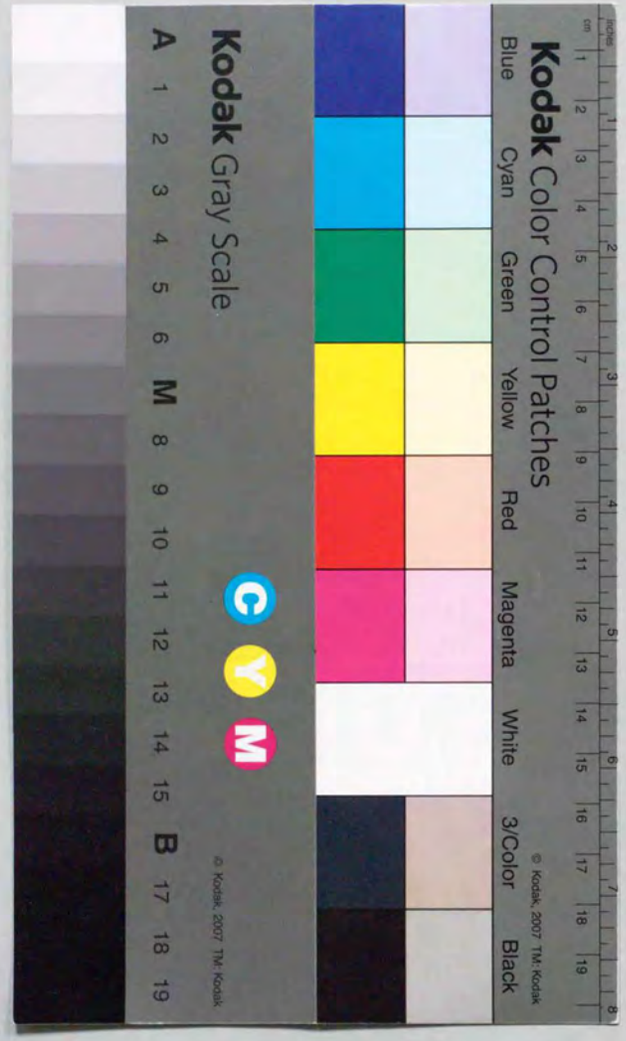

学位論文

Study of Dijet Processes in Photoproduction at HERA

HERAにおける光生成反応による2ジェット事象の研究

平成7年10月 博士（理学）申請

東京大学 大学院 理学系研究科 物理学専攻

山 崎 祐 司

Study of Dijet Processes in Photoproduction at HERA

Yuji Yamazaki

Graduate School
University of Tokyo
7-3-1, Hongo
Bunkyo-ku, Tokyo, 113, Japan

A thesis submitted in partial fulfillment
of the requirements
for the degree of doctor of science

December 25, 1995

Abstract

The inclusive dijet cross section, $d\sigma/dE_T d\eta_1 d\eta_2$ and $(d\sigma/d\eta_2)|_{E_T>E_T^{thr},\eta_1}$, in ep scattering at $\sqrt{s} = 300$ GeV has been measured for the first time in the photoproduction regime of $0.2 < y < 0.85$ and $Q^2 < 4$ GeV^2 using the 1994 HERA positron run of 2.62 pb^{-1}. Two or more jets with $E_T > 8$ GeV and $-1 < \eta < 2$ are required in selecting the dijet event. The result is compared with the QCD-inspired models. The dijet cross section is generally well described by these models up to $E_T = 50$ GeV, whereas the excess of the cross section has been observed for the events with both jets close to the incoming proton direction ($\eta > 1$) and $x_\gamma > 0.75$ where the direct process is dominant. The higher order effect has been studied by the jet rate and the energy correlation of the jets.

Contents

Chapter 1

Introduction

The history of the particle physics is, in short, the history of finding the substructure of the materials. The experiment to be mentioned as a starting point is the discovery of the atomic nucleus by Rutherford. In this experiment the substructure of the atom is probed by α-ray; the helium nucleus beam was injected to the target of metal. This technique of the experiment, injecting a probe to the target, is one of the most effective ways to investigate the substructure, or constituent of the materials, i.e., elementary particles. Another approach to investigate the nature of the fundamental particle is concentrating the energy in a small space. This enables us to make an excited state of the particle, or to create a new particle from the vacuum. In both cases, it is necessary to accelerate the particles and to make collisions.

One of the biggest progresses in investigating the nature of the hadronic particles is the observation of the substructure of nucleons by eN deep inelastic scattering experiment in 1969 by SLAC-MIT group [1]. The experiment found that the structure function, the parametrization of the parton density, was almost constant with respect to the momentum transfer from the electron to the proton. This observation leads to the model that there are pointlike charged particles inside the proton, which are scattered like free particles [2]. The proton is described by the incoherent sum of the pointlike constituents called partons. It is also found that only half of the proton momentum is carried by these charged particles, suggesting the existence of the other neutral particles in the proton. Soon after the quantum chromodynamics (QCD) was developed. It predicted that the charged partons are quarks, and the unknown neutral particle is another gauge boson, called gluon, which propagates the exchange force between quarks.

The existence of the gluon is confirmed by the three-jet production in the e^+e^- collider PETRA at DESY [3]. The e^+e^- annihilation produces a quark-antiquark pair via production of a virtual γ/Z^0. The pair is observed as a two-jet event. The production of the third jet showed an evidence of the radiation of the gauge boson of the strong force. After this, together with deep inelastic scattering, QCD is accepted and applied to the explanation of the various hadronic processes. The high-p_T jet production at $p\bar{p}$ collider Sp$\bar{\text{p}}$S [4] is the first observation where the description of the hadron by QCD was successful. Thereafter it is believed that QCD can describe the interaction of the hadron in a high energy region.

The structure function of the nucleon has been measured in parallel by many experiments using not only electrons but also muons [5] and neutrinos [6]. The behavior of the structure function could be also explained by the QCD-inspired Altarelli-Parisi equation [7, 8], which was another example of the success of QCD.

The photon is the gauge boson that propagates the electromagnetic force in our usual life. When it propagates through a vacuum, it fluctuates into a charged fermion pair, $q\bar{q}$ or l^+l^-, due to the vacuum polarization. This polarization may add another aspect to the photon. When a photon scatters with the hadronic object, the photon may split into $q\bar{q}$. The quark may also evolve into a large number of quarks and gluons in case the polarized quark has small transverse momentum. As the result it forms a vector meson whose quantum number is the same as photon [9]. This fact indicates that, with some probability, the photon reacts as a hadron with the other hadronic objects besides the reaction as a bare photon. This effect has been observed in many experiments of photon-nucleon scattering and other photon-related experiments.

The hadronic behavior of the photon can be parametrized by determining the photon structure function as in the nucleon case. The deep inelastic scattering of the photon, $e\gamma$ scattering, is the most suitable way to measure the photon structure function. The experiments at e^+e^- colliders have measured it in the collision of the electron and the real photon emitted collinearly from the other electron [10]. Though the structure function of the photon has been measured only in the region where the parton momentum fraction is large, the result can be also described by the QCD evolution. Once it is proved that the partonic picture can be applied to the photon, one may expect that the photon-hadron collision can also be described by the perturbative QCD as hadron-hadron case. Before HERA, however, the center of mass energy is restricted within $\sqrt{s} = 18$ GeV in photon-proton scattering experiment, therefore the QCD process like the jet production was hard to be observed.

HERA, the first ep collider, was built mainly aiming at large Q^2 phenomena, but it also serves as a γp collider: the proton collides with the almost real photon emitted collinearly from the electron beam. With this process the γp center of mass energy of up to $\sqrt{s} = 300$GeV is achieved. In this extended energy range, the high-p_T jet production, which had not been measured before HERA, is expected to occur. It will be explained by perturbative QCD as in the case of the $p\bar{p}$ collider.

In this thesis the hard scattering processes in photoproduction are studied by using the dijet event from photoproduction at HERA. For this purpose the triple differential cross section $d\sigma/dE_T d\eta_1 d\eta_2$ and the rapidity distribution of the second jet $(d\sigma/d\eta_2)|_{E_T > E_T^{lab}, \eta_1}$ are measured at HERA for the first time. The data were taken by the ZEUS experiment in 1994 run period.

The thesis is organized as follows. In chapter 2, first kinematical variables at ep scattering are explained. After the current model of the photon and the hard scattering in photoproduction are discussed for the description of the physics on the dijet event in photoproduction. The experimental apparatus and data acquisition system of ZEUS experiment is described in Chapter 3. The Monte Carlo simulations for the photoproduction processes used in this thesis are explained in chapter 4. The selection criteria of the photoproduction event are described in chapter 5. In chapter 6, jet finding and energy correction of the jet is discussed. After the data selection and jet finding, the properties of the dijet events are presented in chapter 7. Finally the cross sections of the dijet events are presented in chapter 8, followed by the discussion of the result in chapter 9.

Chapter 2

Photoproduction at HERA

2.1 Kinematical variables

There are several Lorentz-invariant variables commonly used in describing electron-proton scattering [11, 12]. Q^2 is defined by the momentum transfer square from the electron,

$$Q^2 = -q^2 = -(k - k')^2 \simeq 2k \cdot k'. \tag{2.1}$$

where k and k' denote the incoming and outgoing electron four momentum, respectively, and $q = k - k'$ denotes the four momentum transfer from the electron. In case of one gauge boson exchange, q is the momentum of the gauge boson, and Q^2 represents the wavelength of the gauge boson, as well as the scale of the electron-proton scattering.

The dimensionless variables, Bjorken x and y, are defined as

$$x = \frac{Q^2}{2p \cdot q}, \tag{2.2}$$

$$y = \frac{p \cdot q}{p \cdot k}, \tag{2.3}$$

where p is the momentum of the incoming proton. y represents the energy transfer from the electron in the proton rest frame. These three variables are related using the center of mass energy $s = (p + k)^2 = m_p^2 + 2p \cdot k$ by

$$Q^2/xy = 2p \cdot k = (s - m_p^2) \simeq s, \tag{2.4}$$

hence only two of these variables are independent.

The invariant mass of the hadronic system W is equal to the center of mass energy of exchanged boson and the proton.

$$W^2 = (p + q)^2 = m_p^2 - Q^2 + 2p \cdot q \simeq ys - Q^2. \tag{2.5}$$

The proton mass m_p is neglected in the approximation of the last two equations.

The cross section of the electron and proton scattering is expressed by the product of the leptonic tensor $L^{\mu\nu}$ and the hadronic tensor $W^{\mu\nu}$,

$$\sigma \sim L_{\mu\nu} W^{\mu\nu}. \tag{2.6}$$

In low-Q^2 region ($Q^2 \ll m_Z^2$), the contribution of the weak neutral bosons to the cross section is small, since Q^2−dependence of the photon cross section is $1/Q^4$, while that of the weak boson is $1/(m_{Z,W^\pm}^2 + Q^2)^2$. Therefore the contribution of the weak boson is negligible in the low-Q^2 region and it is possible to regard the electron-proton scattering via photon exchange. In this case, the general form of the hadronic tensor can be parametrized by two components, denoted as W_1 and W_2. The tensor product in formula 2.6 leads to

$$L_{\mu\nu} W^{\mu\nu} = 4W_1(k \cdot k') + \frac{2W_2}{M^2}[2(p \cdot k)(p \cdot k') - M^2 k \cdot k']. \tag{2.7}$$

By substituting the kinematical variables and taking the phase space into consideration, the double differential cross section $d\sigma/dxdQ^2$ is expressed as

$$\frac{d\sigma}{dxdQ^2} = \frac{4\pi\alpha^2}{xQ^4}[xy^2 m_p W_1(x, Q^2) + [(1 - y) + \frac{m_p^2 xy}{s}]\nu W_2(x, Q^2)], \tag{2.8}$$

where $\nu = p \cdot q/m_p$ represents the energy transfer from lepton in the proton rest frame, and α is a fine structure constant. W_1 and W_2 depend explicitly on the two independent variables, x and Q^2.

The simple quark parton model (QPM) relates the cross section formula to the quark distribution inside the proton, considering that the charged partons are the quarks. It is assumed that each quark carries only the longitudinal momentum fraction ξ of the proton and does not carry the transverse momentum. In the QPM, the electron-proton scattering is regarded as a scattering between an electron and a quark. No interaction among partons inside the proton is assumed to occur during the electron-quark scattering. In this case x is the same as the momentum fraction ξ.

To parametrize the cross section 2.8, two dimensionless functions F_1 and F_2, called structure functions, are defined as

$$F_2(x, Q^2) \equiv \nu W_2(x, Q^2) \tag{2.9}$$

$$F_1(x, Q^2) \equiv m_p W_1(x, Q^2) \tag{2.10}$$

The cross section of the electron-proton scattering (eq. 2.8) is rewritten using the structure functions

$$\frac{d\sigma}{dxdQ^2} = \frac{4\pi\alpha^2}{xQ^4}[xy^2 F_1 + [(1 - y) + \frac{m_p^2 xy}{s}]F_2]. \tag{2.11}$$

In the QPM, the structure function is expressed using the parton density

$$F_2(x, Q^2) = \sum_i e_i^2 x f_i(x) \tag{2.12}$$

$$F_1(x, Q^2) = \frac{1}{2x} F_2(x) \tag{2.13}$$

Since in the QPM the partons inside the proton are quasi-free particles, the parton density does not depend on Q^2. Therefore the structure functions in the parton model are expected to scale, namely only depend on x and are constant in Q^2. The two structure functions in the QPM are related by the second formula (Calan-Gross relation [13]).

The scaling of F_2 is due to the fact that the QPM ignores all the effects from QCD – the additional interaction or radiation of partons during scattering. In reality F_2 depends on Q^2, the resolution to measure the parton density. To describe this scaling violation effect, the GLAP (Gribov-Lipatov-Altarelli-Parisi) evolution equation [7, 8] takes into account the gluon radiation and the quark-antiquark pair production from gluon. Since the high-x parton loses the momentum in Q^2 evolution, F_2 at high-x becomes lower at high Q^2, whereas F_2 at low-x becomes higher at high Q^2.

In the electron-proton scattering, the process in which Q^2 is large ($Q^2 \gg \Lambda_{QCD}$) and the proton is scattered inelastically, the process is called deep inelastic scattering(DIS). If a neutral boson (γ/Z^0) is exchanged, the process is called neutral current DIS (NC-DIS or NC). The process with charged boson exchange ($W^{\pm}$) is called charged current DIS (CC-DIS or CC). In the charged current, the final state lepton is a neutrino, hence not observed in the detector.

2.2 Photoproduction

2.2.1 Overview

The electron-proton scattering in very low-Q^2 region ($Q^2 \ll \Lambda_{QCD}$), the scattering can be explained as an interaction between a proton and a quasi-real photon emitted from the electron, thus as a photoproduction process.

In the DIS process, the photon can resolve the individual partons inside a proton, thus the photon directly couples to the quark. In contrast, in photoproduction where the photon $Q^2 \approx 0$, the low virtuality of the photon allows to emit a quark-antiquark pair, which may develop non-perturbatively and form the vector meson whose quantum numbers are the same as those of the photon. Thus in colliding with a hadron the photon may behave as a hadron, besides the bare photon that couples to a quark directly. Current models of this "physical photon" are presented in the following subsection.

2.2.2 The photoproduction in ep scattering

In ep scattering, the photon beam of the photoproduction processes is emitted by the electron beam with almost no transverse momentum ($Q^2 \simeq p_{T\gamma}^2 \approx 0$). The photon energy is not monochromatic. The energy fraction of the photon to the electron is expressed by the y variable in eq. 2.3.

$$y = \frac{p \cdot q}{p \cdot k} \simeq \frac{E_\gamma}{E_e} \tag{2.14}$$

The γp center of mass energy W can be written using y: $W = \simeq ys$ (see eq. 2.5).

The cross section of the ep scattering can be factorized into to two parts in a very good approximation. Namely, the photon emission from the electron and the γp scattering can be evaluated separately.

$$\sigma(ep) = \int_y f_{\gamma/e}(y) \cdot \sigma_{\gamma p}(\sqrt{s})$$

where $\sigma(ep)$ is the total cross section of photoproduction processes of interest, $\sigma_{\gamma p}(\sqrt{s})$ is the total cross section of the processes at a given center of mass energy of γp system and $f_{\gamma/e}(y)$ is the photon flux. $f_{\gamma/e}(y)$ can be calculated by the Weizsäcker-Williams approximation to high accuracy [14]

$$f_{\gamma/e}(y) = \frac{\alpha}{2\pi} \frac{1+(1-y)^2}{y} \log\left(\frac{Q^2_{max}(1-y)}{m_e^2 y^2}\right) \tag{2.15}$$

where Q^2_{max} is the maximum scattering angle of the electron considered. Since the photon flux is the same for e^+ and e^-, hereafter the term "electron" represents both e^+ and e^- otherwise expressed explicitly.

2.2.3 Models of the physical photon

Usually the photon is described by the superposition of the three components [15, 16]: vector-meson-dominance (VMD) model component, an 'anomalous' component and a direct component. The VMD component originates the vacuum polarization of the photon to $q\bar{q}$. These quarks may evolve into the non-perturbative cloud of the partons. To form the vector meson, the virtuality or the transverse momentum of the fluctuated quark should be small. This contribution of the photon reacts with a hadron like a hadron-hadron scattering. The perturbative parton component becomes dominant when the virtuality of the fluctuation is higher, and the split $q\bar{q}$ pair cannot form the vector meson. This component is called 'anomalous' process whose contribution can be calculated only by the perturbative QCD. Only the parton-parton scattering is assumed to occur from this contribution in the photon-hadron collision. The photon structure originates from both the anomalous and the VMD component. The photon in direct component couples directly to the incoming quark from the hadron. It does not contribute to the structure of the photon.

The structure of the photon at a given Q^2 is calculated by means of the QCD evolution starting from the parton distribution of both VMD and the anomalous component. The detail of the calculation is different for each parametrization [16, 17, 18, 19, 20]. The general process to calculate the photon structure function is discussed here. The VMD part acts as a non-perturbative input in calculating the structure function. Normally this is estimated by the structure function of the lowest mass vector meson ρ

$$F_2^{VMD}(x,Q^2) = \frac{4\pi\alpha}{f_\rho^2} F_2^\rho(x,Q^2) \tag{2.16}$$

where f_ρ is the decay constant of ρ meson and $(4\pi\alpha/f_\rho^2)$ gives the coupling of the photon to ρ meson. Usually the structure function of the pion is used as that of the vector mesons.

The quark contribution from the anomalous component is calculated from the point-like process $\gamma \to q\bar{q}$:

$$F_2^{point}(x,Q^2) = \frac{3\alpha}{\pi}\sum_q x e_q^4[(x^2+(1-x)^2)\log\left(Q^2\frac{1-x}{xm_q^2}\right) + 8x(1-x) - 1]. \quad (2.17)$$

These two contributions are added at a fixed Q^2 and evolved by the GLAP equation. The main difference of GLAP equation between the proton and the photon is that there is an inhomogeneous term of the integrodifferential equation that comes from the splitting function $P_{\gamma q}$:

$$P_{\gamma q} = 3e_q^2(x^2+(1-x)^2). \quad (2.18)$$

Including the point-like term, the GLAP equation is expressed as

$$\frac{df_q(x,Q^2)}{d\log Q^2} = \frac{\alpha}{2\pi}P_{\gamma q}(x) + \frac{\alpha_s(Q^2)}{2\pi}\int_x^1\frac{dy}{y}[f_q(y,Q^2)P_{qq}\left(\frac{x}{y}\right) + g(y,Q^2)P_{gq}\left(\frac{x}{y}\right)] \quad (2.19)$$

$$\frac{dg(x,Q^2)}{d\log Q^2} = \frac{\alpha_s(Q^2)}{2\pi}\int_x^1\frac{dy}{y}[\sum_q f_q(y,Q^2)P_{qg}\left(\frac{x}{y}\right) + g(y,Q^2)P_{gg}\left(\frac{x}{y}\right)] \quad (2.20)$$

where $f_q(x,Q^2)$ and $g(x,Q^2)$ are the parton densities of the quark and gluon inside the photon, respectively. The parton-parton splitting functions used in the equations above are as follows.

$$P_{qq}(x) = \frac{4}{3}\left(\frac{1+x^2}{1-x}\right) \quad (2.21)$$

$$P_{gq}(x) = \frac{1}{2}(x^2+(1-x)^2) \quad (2.22)$$

$$P_{gg}(x) = 6\left(\frac{1-x}{x} + x(1-x) + \frac{x}{1-x}\right) \quad (2.23)$$

Due to the inhomogeneous term $P_{\gamma q}$, the photon structure function increases as Q^2 increases in whatever region of x in contrast to the proton case where the high-x part of the structure function decreases in the Q^2 evolution.

2.2.4 The processes in photoproduction

In low-p_T photon-nucleon scattering, the cross section can be explained by a soft process like pomeron exchange, as meson-nucleon scattering since the photon behaves like a vector meson. At HERA, the total cross section of γp at $\sqrt{s} \approx 200$ GeV has been measured [21, 22] and it is well described by the soft process. To describe the high-p_T jet production, one needs the model based on the parton-parton scattering governed by the perturbative QCD in addition to the soft process. So far at HERA, the high p_T jet is observed in photoproduction [23, 24] and demonstrated that the jets cannot be explained by the soft processes. The jet production is studied by the inclusive jet cross section [25, 26]

and the dijet events [27, 28, 29]. These publications reported that the cross section can be explained in terms of the parton-parton scattering. The parton-parton scattering in photoproduction is called hard photoproduction.

The hard photoproduction is also similar to the hadron-hadron scattering except the direct process, where the entire momentum is transferred to the 2→2 hard scattering and there is no photon remnant. If a parton from the photon and a parton from the hadron interact as 2→2 process like in the hadron-hadron scattering, the process is called resolved photon process. The partons that did not participate in the hard scattering carry the rest of the momentum and are observed as a photon remnant in approximately the incoming photon direction (see figure 2.1). The existence of the resolved [24] and direct [27] processes in hard scattering has been reported by the previous publications.

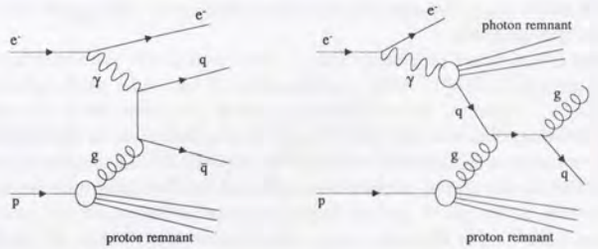

Figure 2.1: The examples of the Feynman diagram of (a) direct and (b) resolved processes.

The lowest order cross section formula of the hard scattering in γp interaction is expressed similarly to the hadron-hadron collision. The cross section is factorized by three parts: the flux of the parton from photon and nucleon, and the parton-parton cross section calculated by perturbative QCD [30]. The event cross section formula of the $2 \to 2$ process is

$$\frac{d\sigma}{d\eta_1 d\eta_2 dp_T^2} = \sum_a\sum_b x_a x_b f_a^\gamma(x_\gamma,p_T^2)f_b^p(x_p,p_T^2)\,\frac{\sigma(ab\to j_1 j_2+X)}{d\hat{t}}, \quad (2.24)$$

where a and b denote the incoming partons from photon and nucleon, j_1 and j_2 denote the outgoing partons and $\hat{t}$ is the Mandelstam variable of the two parton system. In case

of the direct process the cross section is expressed as

$$\frac{d\sigma}{d\eta_1 d\eta_2 dp_T^2} = 2\sum_b x_b f_b^p(x_p, p_T^2)\ \delta\left(2 - \frac{p_T}{yE_e}(e^{-\eta_1} + e^{-\eta_2})\right)\ \frac{\sigma(\gamma b \to j_1 j_2 + X)}{d\hat{t}} \qquad (2.25)$$

The pseudorapidity of the parton η is defined as

$$\eta = -\log\left(\tan\frac{\theta}{2}\right),$$

where θ is chosen as polar angle from incoming proton direction at HERA in the laboratory frame. In case of a massless particle the pseudorapidity interval is Lorentz invariant in the boost along the beam direction, thus suitable for representing the angular information of the parton-parton scattering.

To avoid double counting from the soft and hard scattering processes, the phenomenological cut-off of the minimum transverse momentum p_{Tmin} is introduced to the parton-parton scattering. The sum of the non-perturbative cross section and the parton-parton cross section above p_{Tmin} becomes the total γp cross section. This parameter can only be determined experimentally.

The order of the direct process is $O(\alpha\alpha_s)$. The order of the process of hard scattering in resolved process is $O(\alpha_s^2)$. After multiplication of the order of the photon structure function $O(\alpha/\alpha_s)$, however, the contributions of both processes are in the same order.

One interesting characteristic in the hard photoproduction is the difference of the transverse momentum distribution between the direct and the resolved process. Since the entire momentum of the photon is transferred in the direct process hard scattering, the fraction of the direct process becomes larger as the p_T of the process becomes higher(figure 2.2(a)). For the same reason the rapidity distribution of the jet from the direct process peaks in the photon direction, where that of the resolved process is flatter(figure 2.2(b)).

It is worthwhile mentioning that the classification of the photoproduction event into the resolved and direct processes is meaningful only in the lowest order($2 \to 2$ scattering) [31]. If one considers the next-to-leading-order (NLO) diagram, there are $2 \to 3$ process which can be regarded as both "direct" and "resolved" processes. Figure 2.3 shows an example of the Feynman diagram of these processes. Since the $\gamma q\bar{q}$ vertex of this process can be regarded as either point-like resolved process or direct process, it is needed to define the criteria to classify the "direct" and "resolved" process at a higher order. A proposal of the criteria is presented in the next section.

2.3 Dijet processes in hard photoproduction

The dijet processes in hard photoproduction are the topic to be studied in this thesis. In this section first the reconstruction of the kinematical variables in dijet events is described. Next it is explained why these processes are useful in studying hard photoproduction and how the cross sections are defined for this study.

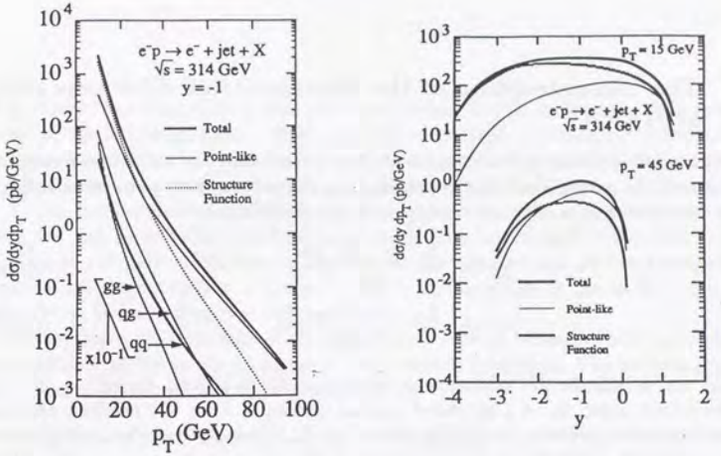

Figure 2.2: The theoretical calculation of the distribution of (a) the transverse energy of the outgoing parton (b) the rapidity distribution of the outgoing parton at HERA by H. Baer et al. [14]. Here the positive rapidity is defined as the photon direction.

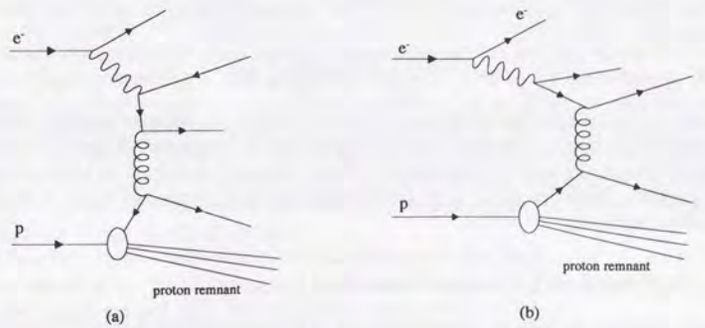

Figure 2.3: The example of the $2 \to 3$ scattering diagram that can be regarded either (a) direct and (b) resolved process.

2.3.1 The reconstruction of the kinematics of dijet processes at HERA

In the dijet process, assuming the lowest order $2 \to 2$ scattering, the longitudinal momentum fraction of the parton inside the proton (x_p) and the photon (x_γ) can be reconstructed from the four momentum of the jets using the following formulae.

$$x_p = \frac{E_{T_1} e^{\eta_1} + E_{T_2} e^{\eta_2}}{2E_p}, \tag{2.26}$$

$$x_\gamma = \frac{E_{T_1} e^{-\eta_1} + E_{T_2} e^{-\eta_2}}{2yE_e}, \tag{2.27}$$

where E_{T_i} and η_i indicate the transverse energy and η of i-th highest E_T jet.

In the lowest order, $x_\gamma = 1$ for direct process and $x_\gamma < 1$ for the resolved process. After hadronization, however, the distribution of the x_γ is smeared and the overlap of the two processes is observed, hence the separation of the two types becomes unclear. The situation becomes worse when we take the higher order calculation. As discussed in the previous section, it is impossible to distinguish the type of the process in case of more than three partons in the final state. Thus, another definition to separate the two types of the processes is needed. Since the x_γ formula in eq. 2.27 can be applied to any order of calculation, the unambiguous definition of the two types can be done according to the fraction of the momentum reconstructed from the two highest p_T jet production. By this reason, a cut $x_\gamma = x_\gamma^{cut}$ is used to separate the resolved and direct event [28]. The value of x_γ^{cut} is determined in section 7.3.

There are two methods in reconstructing y in formula 2.27. The first is to tag the scattered electron The photon energy fraction to the electron is derived from the formula: $y = E_\gamma/E_e = (E_e - E'_e)/E_e$, where E'_e is the energy of the tagged electron. Second is to reconstruct y from the hadronic energy flow. The "Jacquet-Blondel method" [32] is used to estimate y

$$y_{JB} \equiv \frac{\sum_i (E_i - p_{Z_i})}{2E_e} \simeq \frac{2p \cdot q}{2p \cdot k} = y$$

where i shows the index of the final state hadronic particles or detector activity related to the hadronic particles. E_i and p_{Z_i} are the energy and Z-component of the momentum of the particle with the index i, respectively. The Z direction is defined as the incoming proton direction. Hereafter $\sum_i (E_i \pm p_{Z_i})$ is written as $E \pm p_Z$ unless the index is needed to be written explicitly.

2.3.2 Inclusive dijet cross section

One aim to measure the high-p_T jet cross section in photoproduction is to study whether this process is described by the parton-parton scattering, namely the perturbative QCD. As discussed in the previous section, two outgoing partons are observed in the lowest order hard photoproduction event. Therefore using the dijet events is suitable to study

the parton-parton scattering in hard photoproduction. In this analysis the dijet events are chosen by the following reasons. First, x_γ can be calculated according to the formula 2.27, thus the classification into the resolved and direct processes is possible. Second, one can investigate the cross section dependence on the rapidity of both jets.

To see the perturbative QCD effect clear, the events with high-p_T jets are chosen. Since the high-p_T jets that can be seen in the HERA experiments come from the high-x region of the parton densities in the photon, the cross section is less ambiguous. In addition, the reconstruction of the jet energy becomes better as the p_T becomes higher since the jet becomes narrower and well defined.

In this study, the definition of the dijet cross section is taken inclusively; another jet information is added to the inclusive jet cross section $d\sigma/dE_T d\eta$. The following types of the inclusive dijet cross section are presented.

1. The triple differential cross section $d\sigma/dE_T d\eta_1 d\eta_2$,
2. The differential cross section of the second jet for the event with p_T above the threshold E_T^{thr}, and η_1 within a fixed interval: $(d\sigma/d\eta_2)|_{E_T > E_T^{thr}, \eta_1}$.

With the inclusive dijet cross section, the cross section dependence on the three variables E_T, η_1 and η_2 can be seen individually.

In obtaining these cross sections, E_T of the leading jet is taken. The pseudorapidity of the leading and second jet is swapped and then double-counted. Therefore, two entries (E_{T1}, η_1, η_2) and (E_{T1}, η_2, η_1) are filled per event. This symmetrization of the two jets is introduced to avoid the infrared divergence in determining the first jet. When the cross section is calculated in the lowest order, the two scattered partons have the same transverse momentum. Therefore the determination of the cross section depends on the soft particle emission in the higher order calculation and becomes unstable. This definition also avoids the problem in experimental determination of the first jet, which also depends on the detector smearing. This definition has been used in $p\bar{p}$ experiments [33, 34]. Recently, the Next-to-Leading-Order(NLO) calculation of the direct process cross section in photoproduction at HERA energy is published based on the similar definition [35].

Note that this definition does not use the E_T of the second jet except in selecting the second jet above certain threshold of E_T. The distribution of E_{T2} may be different from the model to be compared even if the cross section agrees with the model. Therefore the distribution of E_{T2} should be studied.

These two types of cross section, $d\sigma/dE_T d\eta_1 d\eta_2$ and $(d\sigma/d\eta_2)|_{E_T > E_T^{thr}, \eta_1}$, are measured in two regions of x_γ: for all events and for those with $x_\gamma > x_\gamma^{cut}$. The η and E_T range and x_γ^{cut} will be determined after the event selection, see chapter 7.

Chapter 3

ZEUS experiment

ZEUS is a collaboration at the electron-proton collider HERA. This thesis is based on the data from the ZEUS experiment. In this chapter the accelerator HERA, the ZEUS detector and the data acquisition system are described.

3.1 HERA

HERA is the first electron-proton collider built at DESY (Deutshces Electron-SYnchrotronen) in Hamburg, Germany. The design energy is 30 GeV for electron and 820 GeV for proton, which provide the center-of-mass energy of $\sqrt{s} = 314$ GeV. This is equivalent to the 52.5 TeV lepton energy in a fixed target experiment. The ground plan of the accelerators is shown in figure 3.1. The principal parameters are listed in table 3.1. HERA is 6.3km in circumference. The beams are stored in the separated beam pipes in the bending section, guided to the same beam pipe at the experimental hall and undergo a head-on collision. The RF cavity of the proton is operated in 208 MHz for a short bunch length of 11 cm. Superconducting magnets are used for the dipole magnet of the proton ring, which yields top magnetic field of 4.65 T. Normal conducting magnets are used for the dipole magnet of the electron ring.

For the injector of the HERA, the existing accelerators are used with modifications. The electron beam is first accelerated by the linear accelerator, then preaccelerated by DESY II(9.0 GeV) and PETRA II (14 GeV) and injected to HERA. The proton is preaccelerated by the Proton Linac, followed by DESY III (7.5 GeV) and PETRA II (40 GeV) for the injection of the main ring.

One of the most important features of HERA is a short bunch crossing interval of 96 ns in order to achieve high current and hence high luminosity. In design, up to 210 bunches are used and the luminosity of $1.5 \times 10^{31}\text{cm}^{-2}\text{s}^{-1}$ is aimed at.

The data taking in the 1994 running period

In the 1994 running period, HERA has delivered most of the integrated luminosity by the positron and proton beam due to the bad lifetime of the electron beam. The lifetime

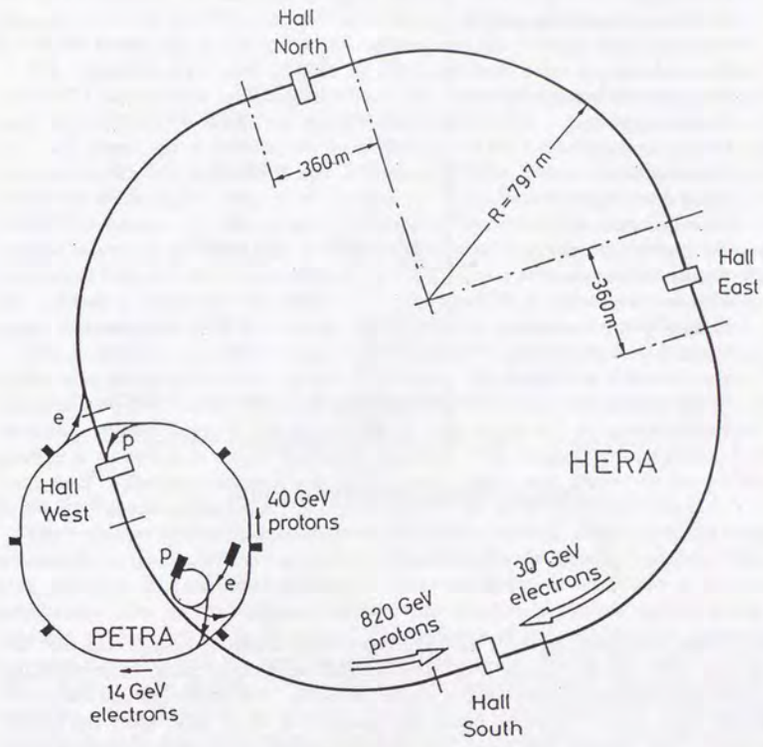

Figure 3.1: The layout of the *ep* collider HERA

	proton ring	electron ring	unit
Nominal energy	820	30	GeV
c.m. energy	314		GeV
Luminosity	1.5×10^{31}		$cm^{-2}s^{-1}$
Number of interaction points	4		
Crossing angle	4		mrad
Circumference	6336		m
Length of the straight section	360		m
Energy range	300-820	10-33	GeV
Bending radius	588	608	m
Magnetic field	4.65	0.165	T
Injection energy	40	14	GeV
Circulating current	160	58	mA
Number of particles	2.1×10^{13}	0.8×10^{13}	
Number of bunches	210		
Number of buckets	220		
Beam size at crossing σ_x	0.27	0.26	mm
Beam size at crossing σ_y	0.08	0.07	mm
Bunch length at crossing σ_z	11	0.8	cm
RF frequency	52.033/208.13	499.667	MHz
Filling time	20	15	min

Table 3.1: Design parameters of HERA

of the electron was short, typically around three to four hours. It is suspected that the ionized dust of the positive charge is collected around the electron beam. After switching to positron, the lifetime was improved to around 10 hours. The proton lifetime was about 200 hours. The electron/positron beam was operated at 27.52 GeV, while the proton beam energy was nominal 820 GeV. The typical current of the proton(positron) was around 40(30) mA. ZEUS has collected about 0.3 pb^{-1} from e^-p runs and 3.1pb^{-1} from e^+p runs. The data from e^+p collision was used for this analysis.

In addition to the normal paired bunch, the proton only and the electron only bunches, called pilot bunches, are circulated to investigate the contribution of the event induced by the beam gas collision. The number of the bunches in the positron run period are 153 paired bunches, 15 electron pilot bunches, 17 proton pilot bunches and 35 empty bunches. Only 16 bunches out of 35 empty bunches are gated by the trigger.

3.2 The ZEUS detector

3.2.1 Overview

The ZEUS detector [36] is a multipurpose detector for the *ep* collider experiment. The schematic view of the ZEUS detector is in figure 3.2. The proton comes from the right side of the beam pipe in the figure, and collides with the electron from the left side.

The entire detector consists of, from the interaction point to outside, a vertex detector(VXD), a central tracking detector(CTD), the forward and rear tracking detectors(FTD and RTD), transition radiation detector(TRD), a high resolution calorimeter(CAL), barrel and rear muon detectors (BMU and RMU), a backing calorimeter(BAC), a forward muon detector (FMU) and a vetowall(VETO). There are additional detectors around the beam pipe of the proton upstream direction: a small-angle rear tracking detector(SRTD), a beam pipe calorimeter (BPC) and a C5 counter(C5). Also the detectors are situated in around the beam pipe of proton downstream direction: a leading proton spectrometer (LPS), a forward neutron counter (FNC) and a proton remnant tagger (PRT). The luminosity counter(LUMI) is situated more than 30 m downstream of the electron beam. The vetowall(VETO) covers the detector of the upstream side of the proton.

The coordinate of the ZEUS detector is defined as indicated in figure 3.2: the incoming proton direction is determined as the Z direction, the horizontal direction toward the center of the HERA ring is X and Y is determined to form a right-handed system. Since the center-of-mass frame of the *ep* collision is boosted toward the proton direction, the positive Z direction is called "forward" direction. The negative Z direction is called "backward". The polar angle θ is defined as polar angle with respect to the positive Z direction. The azimuthal angle ϕ is the angle from the positive-X direction.

There are two notable characteristics in the ZEUS detector. First is that the design is asymmetric to the beam direction, reflecting the beam energy imbalance and the different beam particles. The calorimeters situated in forward direction are thicker to absorb the large energy flow. In the backward direction the detector is planned mainly to tag the scattered electron with high accuracy. The thickness of the rear detector, however, is kept enough to contain the possible hadronic energy flow within the central detector. This is important in studying the events with backward energy flow like very small-x DIS scattering or the photoproduction event. Second is the high hermeticity. The coverage of the detector is 99.8% of the forward hemisphere and 99.5% of the backward hemisphere in solid angle, achieved by the CAL.

The three main detectors in this analysis, the CAL, the CTD and the LUMI, are described.

3.2.2 High resolution calorimeter(CAL)

The first requirement of the calorimetry is a good hadronic resolution for the measurement of the hadronic final state of the DIS NC/CC process and the jet physics. To cope with it, a sampling type consisting of depleted uranium(DU) as absorbers and plastic scintillator

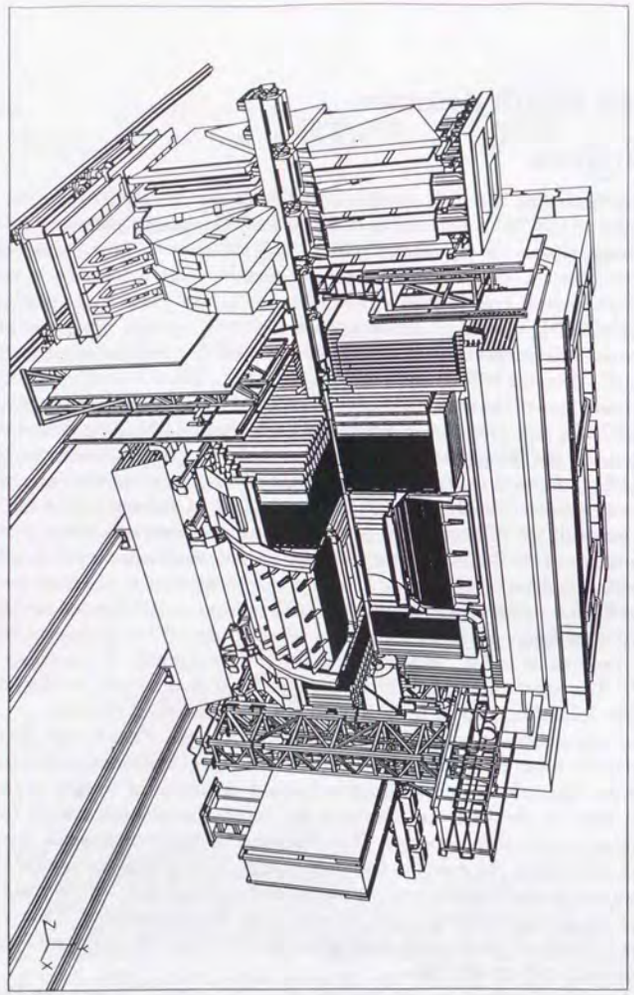

Figure 3.2: The schematic view of the ZEUS detector.

	EMC			HAC		
	thickness (cm)	X_0	λ	thickness (cm)	X_0	λ
steel	0.2	0.011	0.0012	0.4	0.023	0.0024
DU	3.3	1.000	0.0305	3.3	1.000	0.0305
steel	0.2	0.011	0.0012	0.4	0.023	0.0024
sci.	2.6	0.006	0.0033	2.6	0.006	0.0033
others	1.3	–	–	1.3	–	–
total	7.6	1.028	0.0362	8.0	1.052	0.0386

Table 3.2: The parameters of one layer DU+scintillator. Here X_0 and λ are the radiation length and absorption length of the calorimeter cell.

	FCAL			BCAL			RCAL	
	EMC	HAC1	HAC2	EMC	HAC1	HAC2	EMC	HAC
number of layers	25	80	80	21	49	49	25	80
radiation length X_0	25.9	84.2	84.2	22.7	52.4	52.5	25.9	84.2
absorption length λ	0.960	3.09	3.09	1.046	2.03	2.04	0.953	3.09
thickness (cm)	25.1	64.0	64.4	21.3	42.2	42.4	23.6	64.4
total radiation length		194.3			127.6		108.5	
total absorption length		7.14			4.92		3.99	
total thickness (cm)		152.5			105.9		87.0	

Table 3.3: The parameters of FCAL, BCAL and RCAL. The radiation length and the absorption length are measured in normal to the calorimeter face. In part of the FCAL and RCAL the longitudinal length is shorter.

tiles as samplers are chosen.

The structure

The calorimeter consists of three parts: a forward calorimeter (FCAL), a barrel calorimeter (BCAL) and a rear calorimeter (RCAL). The FCAL, BCAL and RCAL cover the polar angle of 2.2° to 39.9°, 36.7° to 129.1° and 128.1° to 176.5°, respectively (see figure 3.3). The parameters of each calorimeter are summarized in table 3.2 and 3.3.

The longitudinal structure of the calorimeter is divided to two parts: EMC for the electromagnetic calorimeter and HAC for the hadronic calorimeter. The longitudinal depth of the EMC is about $25X_0(\simeq 1\lambda)$ and the HAC is 7.1λ (for FCAL). For the FCAL and BCAL the HAC section is further subdivided into two sections, HAC1 and HAC2.

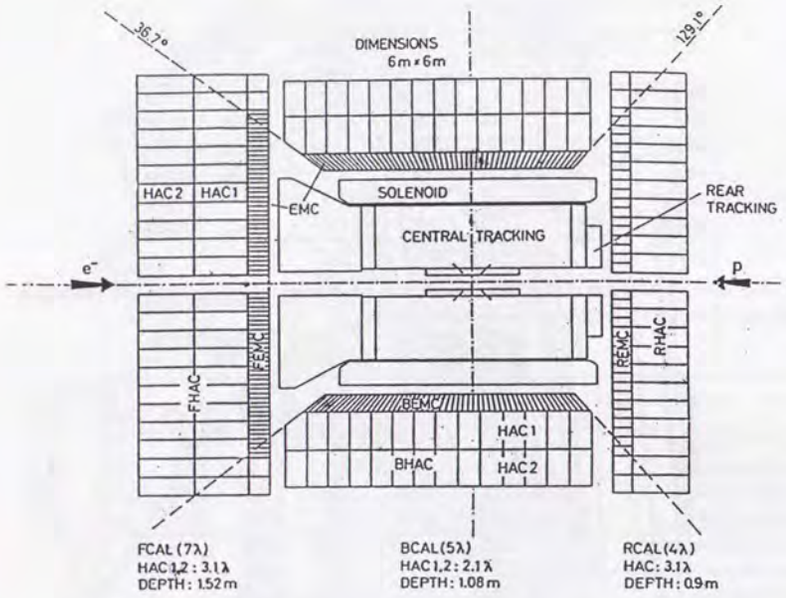

Figure 3.3: The cross section of the ZEUS calorimeter.

In the following the RCAL EMC may be called as REMC, RCAL HAC as RHAC and so on.

The FCAL and RCAL consist of the repetition of the rectangle section of 20 × 20 cm section. The vertical stack of the section is called a module. Figure 3.4 shows the schematic view of a module in FCAL. Each section is called a tower and each unit of the readout is called a cell. The transverse cross section of the HAC cell is the size of the tower, 20 × 20 cm, while the tower is divided horizontally to four 5 × 20 cm EMC cells in FCAL, and two 10 × 20 cm EMC cells of in RCAL to provide the better vertical position resolution. Both EMC and HAC are non-projective to the incoming particle from the interaction point. The beam hole of both FCAL and RCAL is the size of one tower, 20 × 20 cm. The small beam hole provides an excellent hermeticity.

The overall structure of the BCAL is the similar to the FCAL or RCAL. The trapezoid

shaped tower is cumulated to $Z-$direction to form a module. 32 modules form the entire barrel calorimeter of the cylindrical shape. Each tower faces to the interaction point in $X-Y$ plane to form the projective shape to the beam axis, though the trapezoid is skewed in ϕ by 2.5° to avoid that the module boundary is projective. The cross section of the HAC cell is the tower size of 20 × 28 cm. The EMC section is bended so that each cell is projective to the interaction point also in Z-direction. An EMC cell is one of the four subdivisions of the tower in Z-direction.

Figure 3.5 shows the cross section of a tower in FCAL. In the tower the DU plate (3.3 cm) and the plastic scintillator (2.6 cm) are stacked alternatively perpendicular to the longitudinal direction. DU plates are clad by the stainless steal of 0.2 mm thick(in EMC) to provide the moderate shield to reduce yet provide enough rate of the radiation from the DU for the calibration of the gain of photomultiplier (PMT) mentioned below. The sampled signal from the scintillator of each cell is read out by the wave length shifter (WLS) from both sides of the scintillator. The WLS converts the photons of short wave length from the scintillator to the longer region and propagate the photon to the PMT. The signal of the PMT is amplified in the two shapers, high-gain and low-gain, to provide both a large dynamic range and an accuracy in low energy.

The performance

The most important benefit of the combination of the uranium as the absorber and the plastic scintillator as the sampler is that one can make the response of the hadronic and electromagnetic particles to be equal. Usually the response of the hadron shower in the calorimeter is less than that of the electromagnetic shower. This is mainly because the energy of the neutron, soft $\gamma-$ray and heavy nuclei, which is produced in the consequence of the excitation or the fragmentation of the nucleus, are undetected since they often stop in the absorber. With the combination of the uranium and the plastic scintillator, the neutron from the fragmented uranium causes the elastic scattering with the hydrogen in the scintillator and produce the scintillation. From this contribution, the smaller response from the hadronic shower is "compensated" if one optimizes the thickness of both the uranium and scintillator plate. The result of the beam tests [37, 38] confirmed the compensation:

$$e/h = 1.00 \pm 0.03 \quad \text{for E} > 3 \text{ GeV}$$

where e/h is the detector response ratio of the electromagnetic to the hardron shower at given energy. In the consequence hadronic and electromagnetic showers can be measured in single type of calorimeter without any correction dependent on the particle type. Both the electromagnetic and hadron calorimeters are build by the same materials and in the structure.

Once the energy response is compensated, the energy resolution of the hadronic shower is improved, mainly because energy of the neutral pions produced in the hadronic shower is measured as the same scale as that charged pions. The energy resolution of the hadronic shower is

$$\sigma(E)/E = 35/\sqrt{E} \oplus 2\%$$

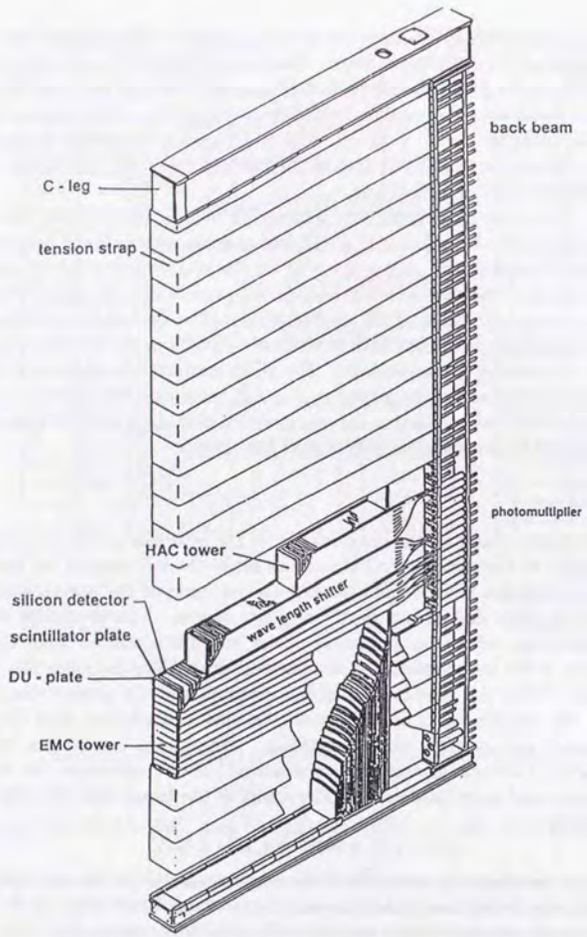

Figure 3.4: The schematic view of a module in FCAL.

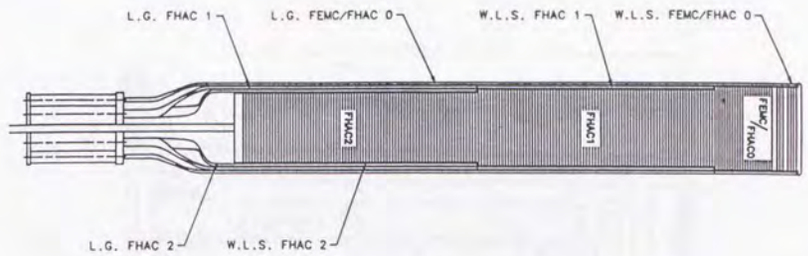

Figure 3.5: The cross section of a tower in FCAL.

where E is in GeV and the symbol $\oplus$ means the addendum in quadrature. The energy resolution of the electromagnetic shower is

$$\sigma(E)/E = 18/\sqrt{E} \oplus 1\%.$$

Another virtue in this calorimeter is the fine timing resolution of the plastic scintillator. The timing resolution of $\sigma(t) = 0.5ns + 1.5ns/\sqrt{E(GeV)}$ makes it possible to use the calorimeter as a coarse time-of-flight detector. The position resolution of the direction perpendicular to the readout surface of the scintillator is determined from the pulse height balance of both readouts, while the direction parallel to the read out surface can use the fine segmentation of the cell in EMC.

The calibration of the calorimeter is performed by several ways. The scintillation light coming from the radioactivity of the DU (Uranium NOise, UNO) is constant and used as a monitor of the absolute calibration scale. The ratio (E/UNO), the ratio of the UNO signal to the response from a given energy particle is known by the beam test. The charge injection to the preamplifier checks the balance of the low- and high-gain. The light injection by laser and the LED to the PMT is used to monitor the linearity of the PMT and the readout electronics. A ^{60}Co source scan is done once per year to check the local uniformity inside each cell. Finally the beam halo muon(see also section 5.2) is used as a source of the minimum ionized particle to see the absolute energy scale.

3.2.3 Tracking detectors

The central tracking of the ZEUS detector is performed by the six detectors: VXD, CTD, FTD, RTD, TRD and SRTD. In this analysis the information of the VXD and the CTD is used to find the vertex. The FTD, RTD and TRD were not fully operational in the 1994 running period. The configuration of the tracking detectors is shown in figure 3.6.

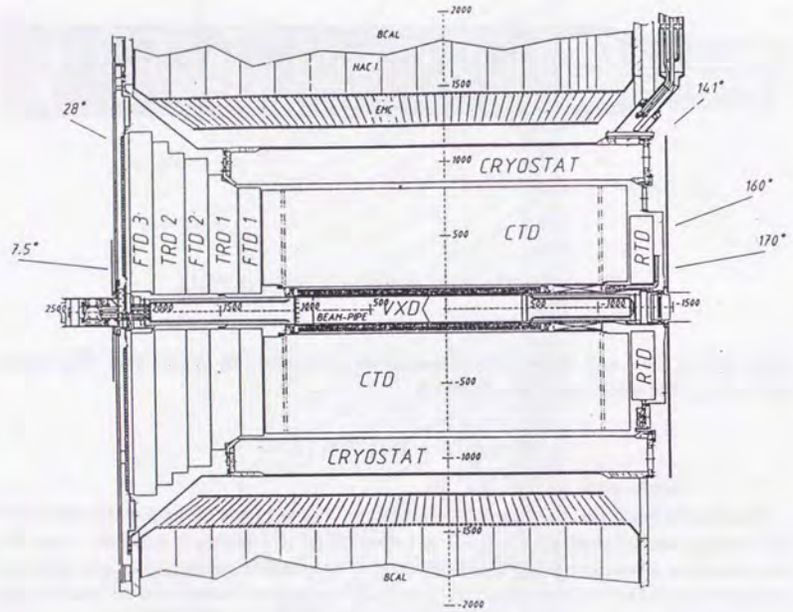

Figure 3.6: The layout of the tracking detector.

Central tracking detector (CTD)

The central tracking detector is a drift chamber of the cylindrical shape. The inner and outer radii are 16.2 and 85 cm, and the length is 241 cm. The chamber consists of nine superlayers (SL). Figure 3.7 shows the wire layout of the octant of the CTD. The angular coverage of the CTD is from 11.3° to 168.2° in polar angle for the track that passes at least the innermost superlayer. The coverage for the track that passes all the superlayers is from 36.1° to 142.6°. Of the nine superlayers, the wires in the odd number layers are spanned parallel to the beam, whereas those of the even number layers have small angle stereo wires.

The magnetic field of the CTD volume provided by the superconducting solenoid is high (1.43T) for the good momentum resolution of the high-p_T track. The field imposes

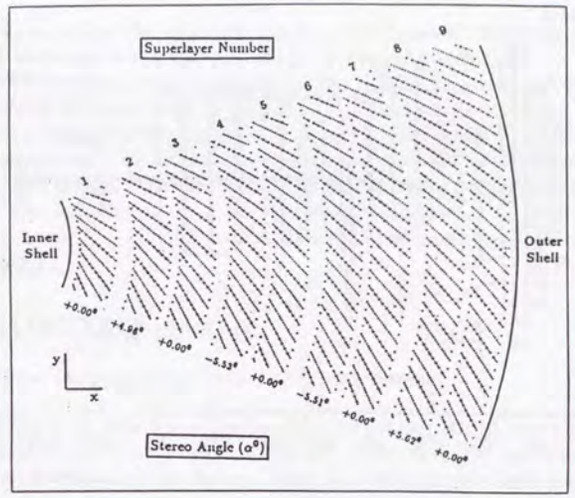

Figure 3.7: The wire layout of the octant of CTD.

high Lorentz angle of 45°. The short drift path (max. 2.56cm) is chosen so that the drift time is short (< 500ns) enough to distinguish the tracks from the neighboring bunches. The single track resolution of the CTD is about 190 μm in $X-Y$ plane and about 3.3 cm in $Z-$direction.

3.2.4 Luminosity Monitor(LUMI)

The luminosity at HERA is measured using the bremsstrahlung process $ep \rightarrow ep\gamma$. This process is chosen since (a) the cross section is calculable by QED and well controlled (b) the rate is sufficiently high and (c) the background is easily controlled. The events with both the photon and electron emitted in very small angle are used.

The layout of the detector is shown in figure 3.8. There are two counters to tag the process: the photon and electron counter. The final state photon travels in the proton beam pipe by $Z = -80$ m, where the proton is vertically vended. Then the photon is escaped from the beam pipe through the copper-beryllium window at $Z = -92.5$ m, and detected by the photon calorimeter situated at $Z = -106.9$ m. The calorimeter

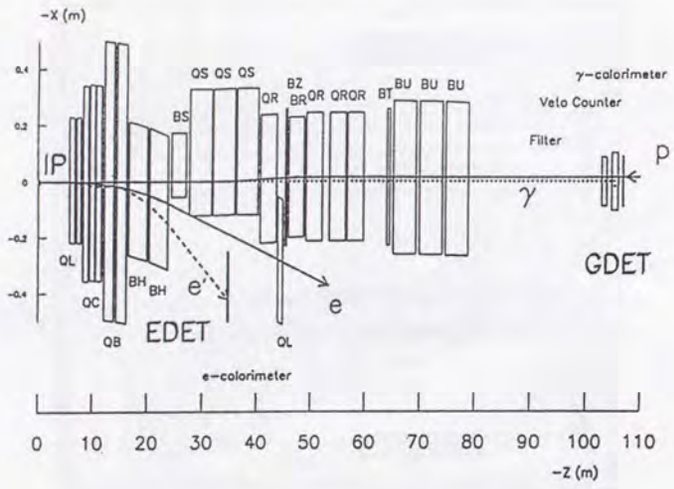

Figure 3.8: The layout of the luminosity monitor.

is sampling type of the combination of lead and the plastic scintillator. The plastic scintillator fiber arrays are inserted in the two layers of the scintillator sampler to measure the position of the photon. The front surface of the calorimeter is covered with the filter of $1.5X_0$ carbon and $0.5X_0$ lead in the 1994 running period to absorb the soft photons from the synchrotron radiation [39]. The orbit of the outgoing electron is bended by the bending magnet for the electron beam with a smaller radius due to the lower momentum than the electron beam. Therefore the electron from this process of the energy $E_e \sim$ 8-24 GeV escapes from the steel window at $Z = -27.3$ m, and comes into the electron calorimeter, almost attached inside the electron ring at $Z = -34.7$ m.

The luminosity is calculated based on the counting of the bremsstrahlung photon since the background is well controlled with only the photon counter. The background of this method is the bremsstrahlung photons from the electron beam and the residual gas inside the beam pipe. This contribution is subtracted statistically using the background rate of the electron pilot bunch,

$$R_{ep} = R_{total} - kR_{e-pilot}$$

where the R_{total}, R_{ep} and $R_{e-pilot}$ are the total rate of the photon, the contribution of the rate from ep collision and the rate from the electron pilot bunch, and k is the ratio of the

electron bunch current of the ep to the electron pilot bunches. The electron counter is used to check the acceptance simulation of the photon calorimeter.

The main error source of the luminosity in the 1994 running period [39] comes from the subtraction of the background (0.3%), the theoretical ambiguity of the cross section (0.5%) and the ambiguity of the energy scale (0.65%), which result to the overall error of 1.0%. The contribution from the non-elastic scattering $ep \to eX\gamma$, for example $ep \to e\Delta\gamma$, is about five order smaller than the elastic contribution hence negligible [40].

Since the electron calorimeter of the luminosity monitor has an acceptance to the scattered electron of $Q^2 \sim 0$, i.e., from the photoproduction process, it is also used as an electron tagger.

3.3 ZEUS DAQ system

There are two main requirements to the ZEUS DAQ system.

1. **High background rejection.** The background rate of HERA experiment reaches to O(100kHz) due to both the high residual gas in the beam pipe produced by the synchrotron radiation of the electron beam and the large cross section of the proton. In contrast the expected physics rate at the design luminosity is about 5 Hz.

2. **Low dead time.** The bunch crossing interval of HERA is 96ns, which is nearly one order of magnitude shorter than previous e^+e^- and $p\bar{p}$ collider. This is too short to deal the detector signal and give the trigger decision within this interval. If one triggers the readout with the minimum requirement of the event and read out the entire information from the detector, one cannot avoid high dead time.

To cope with these problems, ZEUS adopted the combination of a pipeline readout system for the detector signal and a three level trigger: the first level trigger (FLT), the second level trigger (SLT) and the third level trigger (TLT). The schematic diagram of the trigger and the DAQ system is shown in figure 3.9.

3.3.1 The pipeline readout system and the first level trigger

The first level trigger and the pipeline system cooperate to reduce the dead time – the pipeline store the raw data while FLT is processing. The pipeline system is an array of switched capacitors or the memories, in which the analogue or the digital signal of each bunch crossing is stored. The array has the length of 58 units, hence it can store the detector data of 58 bunch crossing or 55.7μs. This produces a computing time of 58 crossing intervals for the first level trigger to make a decision. In practice 46 crossings are used to keep a room for the communication time and the bunch crossing ambiguity.

The structure of the FLT is divided into two parts: component FLTs and the Global First Level Trigger (GFLT). Each component FLT provides the trigger signal within 26 crossing intervals. Most of the detector components have a special readout for the

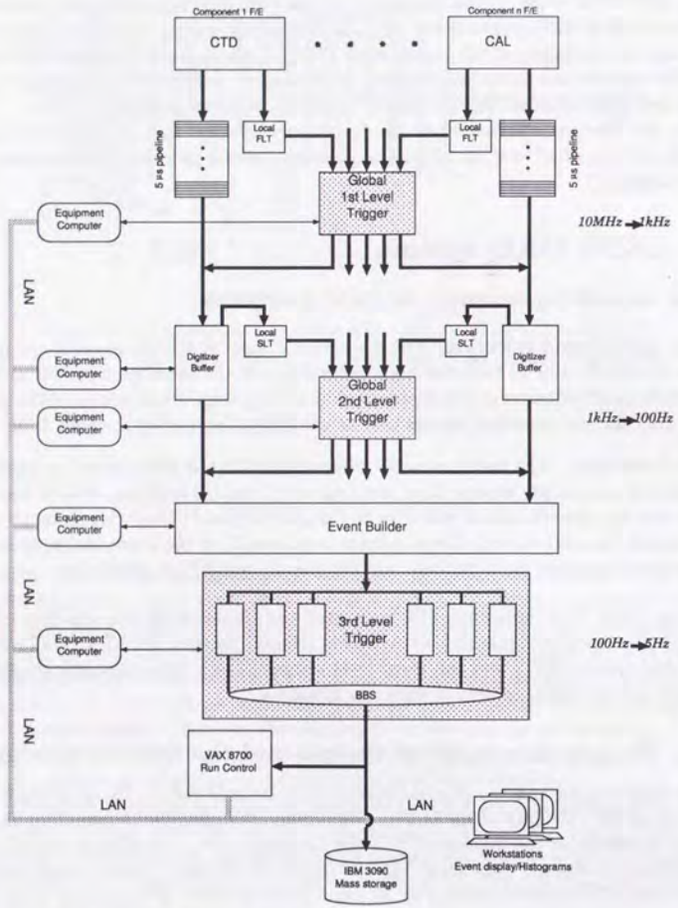

Figure 3.9: The trigger and the DAQ system of the ZEUS experiment

component FLT and provide signals that are coarse but calculable in short time. For example the calorimeter FLT picks the 5% of the analogue signal, digitizes and calculates the global energy information etc. all by hardware.

The GFLT receives these signals from the component FLTs, and makes a trigger decision within 20 crossing intervals. If the decision is positive, the accept flag is sent to each detector component. This flag prompts the readout of the pipeline information of the corresponding bunch crossing number. GFLT does not issue a further trigger until all the components complete the readout of the pipeline. With this mechanism dead time of the readout is kept small. The dead time in the 1994 running period is around 1–2 percent, depending mainly on the luminosity. The typical output rate was a few hundred Hz.

GFLT also maintains the synchronization of the pipeline system and the first level trigger by providing the HERA clock to each component.

The trigger logic evaluation in GFLT

In the FLT, the maximum allowed trigger rate is about 1 kHz due to the limited length of the buffer in SLT (see the next subsection). To reduce the 10MHz bunch crossing to 1kHz, GFLT should be able to evaluate the various complex logics at the same time within the fixed computing time of 20 bunch crossing intervals. In addition, the logics of the trigger should be able to be changed easily following the physics interest, which may be different between low and high luminosity periods. To fulfill these requirements, the memory lookup table (MLT) technique is adopted for the logic evaluation. The MLT can realize any projection of the fixed input and output bit width, which is suitable for GFLT since the number of the input and output signals are stable.

GFLT uses 32kbytes SRAM of 16bit address width and 4bit output as MLT unit. The input signal of about 700 bit is fed to the first layer of MLT. The trigger logics are evaluated in passing through the three layers of MLT formed by about 160 units of MLT. GFLT can produce the 64 independent trigger signals, each of which is called subtrigger. The final decision is the OR of these subtriggers after the VETO is applied to each subtrigger independently.

The online control process of the GFLT sets up the trigger logic by calculating the contents of the MLT according to the trigger description. The description is written in high-level computer language whose grammar is close to the C language. This make the setup of the logic easy since one can concentrate the logic itself, regardless of how the hardware configurations are. The same description is used in making a simulation program code of the GFLT logic used in the offline reconstruction and the Monte Carlo simulation. The offline code generator program reads the same description as used in online and generates a FORTRAN code [41]. This avoids the human error in writing the simulation code and make a fast update possible.

3.3.2 Event buffer and the second level trigger

Prompted by the GFLT decision, the data in the pipeline system are read out and the analogue data are digitized. The results are stored to the digitizer buffer and sent to SLT. The SLT is divided to two parts as the FLT: local SLT and global SLT (GSLT). The trigger signals are processed in each local SLT. GSLT evaluates the trigger logic using the information from the local SLT. Since the local SLT can use all the information from the pipeline readout, the trigger signals are in more detail than the FLT To provide flexibility, the DSP and the transputer [1] are used in the signal processing. With these architectures the better rejection of the background can be achieved. The design rejection factor is 10, which results in the output rate of 100 Hz. In 1994 run period, the typical output rate of SLT was 20–30 Hz.

The role of the digitized buffer is the same as the pipeline; it provides the computing time for the SLT. The depth of the buffer is 15. Since the maximum input rate is 1kHz, The maximum computing time allowed in SLT is estimated as 1/1kHz×15= 15 msec, though 8 msec is recommended considering the fluctuation of the GFLT input rate [42].

When GSLT issues a positive decision, the data in the event buffer are sent to the event builder (EVB). The event builder collects the data from each component and constructs an event data structure according to the format of the database.

3.3.3 The third level trigger and data recording

The role of the third level trigger is to reduce the output rate to 5 Hz by selecting the physics event. A large computing power is required to perform complicated trigger logics necessary for the reduction. To realize this, the third level trigger adopts a distributed computing system. A farm of 30 workstations (SGI with MIPS R3000) is formed by connecting each other with a network. The master machine distributes the incoming events to each machine and collects the result. The event that passed the TLT trigger is sent to the mass storage on a mainframe computer. In the 1994 running period, the typical output rate was about 3 Hz.

The benefit of using the compatible workstation to the offline analysis machine is that the code development of the TLT trigger logics is very easy. Any offline reconstruction and analysis code can be easily ported to TLT.

[1] The name of the processor for the parallel processing.

Chapter 4

Monte Carlo Simulation

To measure the quantity on hadrons or partons, one has to know the correspondence between the quantity on detectors and the quantity on the level one wants to measure. One also has to estimate the detection efficiency of the process to be measured, and to estimate the background processes. They are evaluated using the Monte Carlo(MC) technique.

There are two parts in the MC: the event generation and the detector simulation. In this chapter the event generation part is discussed.

4.1 Overview of the Monte Carlo generators in hard photoproduction

The simulation of the hard process consists of the three parts. First, the incoming particle is generated according to the parton density. The initial state radiation is simulated if necessary. Next, the hard scattering process is simulated. The events are generated so that the momentum distribution of the generated events reproduces the cross section formula. Finally, the final state radiation, the hadronization of the partons and particle decays are simulated according to the model taken in the simulation program.

Usually the final state particle production is simulated in three parts: the matrix element(ME), the parton shower(PS) and the fragmentation. First the hard scattering itself is simulated by the exact calculation of the matrix element. In this step only a few outgoing partons, whose mass scale is typically above a few GeV, are generated to a fixed order. Since analytic calculation of the higher order process is too complicated, it is simulated normally by a parton shower model, which generates the parton emission from the outgoing partons. The model is normally based on the Altarelli-Parisi type splitting functions. This takes the leading logarithm effect for the emission. The parton emission is repeated iteratively until the virtuality of the parton reaches to the value of the cut-off parameter $Q_0 \simeq 1$ GeV where the transition from perturbative to non-perturbative QCD occurs. This iteration approximates the matrix element calculation to a higher order. Since the parton in low virtuality cannot live for long time due to the colour

confinement, it fragments to hadrons. This fragmentation process cannot be described by the perturbative QCD. Therefore a phenomenological model to simulate the hadron production is needed.

In this paper, two Monte Carlo packages PYTHIA 5.7 [43] and HERWIG 5.8 [44] are used to calculate the cross section. A variation of HERWIG in which multiple interaction is implemented is also used in estimating the possible systematic uncertainty in the energy flow [45].

4.2 PYTHIA

The PYTHIA is a program package that is capable to simulate various physics processes in $p\bar{p}$, e^+e^- and ep collisions. It is originated from the program JETSET [46] for the hadronic production in the e^+e^- annihilation process. The fragmentation of JETSET and PYTHIA is based on the Lund string fragmentation model.

The string fragmentation model is based on the simple assumption that the potential between quark and antiquark is proportional to the distance r of the $q\bar{q}$ pair,

$$\phi(r) = \kappa r$$

where $\kappa \approx 1$ GeV/fm denotes the mass density per unit length. This model called linear confinement assumption, is inspired from the lattice QCD. This potential between the $q\bar{q}$ pair has a narrow transverse dimension of the hadron size called string. When the $q\bar{q}$ pair moves apart, the energy stored in the string increases, and reaches enough to create a new $q\bar{q}$ pair from the vacuum. The system is split into two new colour neutral $q\bar{q}$ states and forms two new strings. Each string runs approximately to the original quark direction with transverse energy smearing of the order of the hadron mass. If the invariant mass of the new $q\bar{q}$ is low enough, they form a hadron; otherwise the process is repeated. Eventually the first $q\bar{q}$ pair loses all the virtuality and turns into hadrons. In case of the presence of a gluon, the string is spanned from the quark via the gluon to the antiquark. The gluon is treated as a kink of the string: two strings from the quark to the gluon and from the antiquark to the gluon are fragmented by the same mechanism as the string between the $q\bar{q}$.

PYTHIA has two options in simulating the photoproduction processes. In the first option, the resolved and direct processes are simulated separately. The photon structure function chosen by the user is used in the resolved process. In the second option, the contributions from VMD, anomalous, and the direct components are mixed according to the recommendation of the model [15]. In this option the photon structure function is built in the mixture of VMD and anomalous processes and is unchangeable. Considering also that the second option came only recently, the first option is selected in this work. The photon spectrum from the electron beam is simulated by eq. 2.15. PYTHIA uses the lowest order matrix element in simulating the hard scattering. The scale of the hard scattering Q^2 in PYTHIA is taken by the formula $Q^2 = (m_{T1}^2 + m_{T2}^2)/2$, where

$m_{Ti}^2 = p_{Ti}^2 + m_i^2$ denotes the transverse mass of two outgoing partons. The higher order effects are simulated by the parton shower.

For this study, the hard photoproduction events are generated by PYTHIA with the beam energies are the same as the 1994 running period. For the structure function, GRV-LO for the photon and MRSA for the proton is used. Both direct and resolved components are generated. These processes are added according to the cross section from the generator.

4.3 HERWIG

HERWIG is another program package that simulates most of the QED and QCD processes in $p\bar{p}$, e^+e^- and ep collisions. The largest difference from the PYTHIA package is its fragmentation model named cluster fragmentation.

The cluster fragmentation model first splits all the gluons to $q\bar{q}$ pairs after the perturbative parton shower process. All the colour connection is identified and each forms a colour neutral state, called a cluster. Each cluster has mass and spatial dimensions whose scale is typically around the Λ_{QCD} and peaks at low value. Then the cluster decays into hadrons. The cluster simply becomes a hadron if it is light enough to form a hadron. While the mass of the cluster is larger but not too large, the cluster decays isotropically into two clusters, which is in contrast to the string model where the split string runs approximately to the original quark direction. In case the cluster is too heavy to decay isotropically into two clusters (typically around 4 GeV), the cluster decays in the original quark direction, which is similar to the string fragmentation.

In HERWIG, the resolved and direct processes are simulated separately. In the simulation of the direct event, the exact matrix element of the process of $O(\alpha\alpha_s)$, i.e., $ep \to e' + qg + X$ (QCD Compton) and $ep \to e' + q\bar{q} + X$ (boson-gluon fusion) is used. In the resolved process, the partons from both beams are used in the hard scattering process, thus the lowest order of the hard process is simulated by the matrix element. The scale of the hard scattering is taken as $2\hat{s}\hat{t}\hat{u}/(\hat{s}^2 + \hat{t}^2 + \hat{u}^2)$ where the $\hat{s}, \hat{t}, \hat{u}$ are the Mandelstam variables in the parton-parton system. For both direct and resolved processes, the higher order effects are simulated by the parton shower.

HERWIG events are generated using the same structure functions and beam energies as PYTHIA for this study.

4.4 Multiple interaction in HERWIG

The multiple interaction(MI) is the process in which more than one parton from each beam particle interacts per one hadron-hadron scattering, see figure 4.1. In photoproduction, this process can occur only for the resolved process since the direct process has no parton component inside the photon.

The motivation of introducing the multiple interaction comes from the fact that the

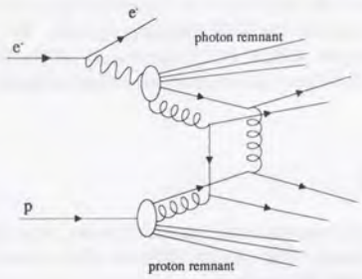

Figure 4.1: An example of Feynman diagrams of multiple interaction in γp collision.

total cross section of the hard process calculated from the parton-parton interaction exceeds the observed total cross section. The total parton-parton cross section is expressed using the cut-off p_{Tmin}.

$$\sigma_{hard}(p_{Tmin}) = \int_{p_{Tmin}}^{\sqrt{s}/4} \frac{d\sigma}{dp_T^2} dp_T^2$$

At high center of mass energy, the differential cross section $d\sigma/dp_T^2$ cannot be well calculated since the low-x behavior of the parton distribution inside the photon is not yet clear. Therefore there is a possibility that the total cross section by this formula can be very large at high energy. Further, since the integration diverges as $p_{Tmin} \to 0$, the choice of p_{Tmin} changes the total cross section very much. Because of these reasons, most of the total cross section calculation based on the parton-parton cross section in hard process exceeds the experimental result [21, 22]. What one measures, however, is a total hadron-hadron cross section, not the parton-parton cross section. To make the parton-parton cross section matched to hadron-hadron one, one can assume that more than one parton-parton scattering occur within one hadron-hadron scattering. The parton-parton cross section is renormalized into one hadron-hadron cross section by using the factor of

$$\langle n_{scat} \rangle = \frac{\sigma_{hard}}{\sigma_{hadron}}, \tag{4.1}$$

where σ_{hadron} denotes the total hadron-hadron cross section and $\langle n_{scat} \rangle$ is the mean number of the scattering per one hadron-hadron interaction.

Once multiple interaction is introduced in the hard photoproduction cross section calculation, the behavior of the cross section changes. Since non-highest p_T scatterings

inside one event are normally of very low-p_T whose parton-parton cross section is very high. Therefore the effect of the MI is not observed as a jet but as an increase of the transverse energy flow pedestal of the jet or the soft underlying events. More jet energy is observed than the jet without MI if the parton momentum is the same. Therefore the jet cross section from the highest p_T scattering in the multiple interactions increases.

The energy flow pedestal depends strongly on the soft part of the parton density [47]. The change of the structure function in the low-x region affects the $\langle n_{scat} \rangle$ hence the p_T distribution of the softer parton-parton scattering in one hadron-hadron scattering. The jet energy pedestal is also changed. In the consequence the increase of the hard scattering cross section is observed in moderately high-p_T region where the cross section does not strongly depend on the change of the parton density in the normal model. Due to this mechanism, the change of the parton density affects nonlinearly the cross section and the factorization of the cross section (eq. 2.24) is broken. To make the MI model to describe the data, one has to readjust the parameter p_{Tmin} to the data. Note that the change of p_{Tmin} is strongly connected to the choice of the structure function if one keep $\langle n_{scat} \rangle$ or the cross section.

To generate the multiple interaction in one event, first the average number of the parton-parton interactions is estimated according to formula 4.1. The number of the scatterings per each event is determined using the Poisson distribution. The probability of the m scattering per one event is given by

$$p(m) = \frac{(\langle n_{scat} \rangle)^m}{m!} \exp(-\langle n_{scat} \rangle).$$

Once the number of scatterings is determined, these hard scatterings are generated independently. This algorithm may generate an unphysical event if the sum of the parton momentum over all the scatterings inside an event exceeds unity, especially in case of partons from a photon. This is avoided by simply removing such an event. The colour connection of the partons is complete only for the highest p_T partons. All the lower p_T scatterings are assumed to be of the subprocess $gg \to gg$. The colour connections are established within a gg pair of the subprocess and never connected to the highest p_T subprocess.

In this study the events are generated using the same structure functions as PYTHIA and HERWIG. The p_{Tmin} is chosen as 2.5 GeV.

4.5 Hard diffractive process Monte Carlo

POMPYT [48] Monte Carlo program is used for the estimation of the hard diffractive photoproduction process. POMPYT is based on the suggestion in the paper [49] for the flux factor and both gluonic and quarkonic parton distributions of the pomeron . The result from this generator shows a good agreement with the data in the previous publications [50, 51]. In this paper the fraction of the gluonic component is taken as 0.5 as observed in the paper [52]. Note that the main difference between quarkonic and

gluonic components of the POMPYT prediction is the absolute cross section, and the event characteristics do not depend largely on the type of process.

Chapter 5

Event Selection

As discussed in the previous section, each of the three levels of the ZEUS trigger system is integrated to the DAQ system and plays a role to reduce the outgoing event rate to 5 Hz at the TLT output. To achieve this, it is necessary to embed event selection criteria as many as possible to the online trigger to keep the output rate below the limit and take necessary physics events. Most of the selection criteria for hard photoproduction are running on the trigger. Both the trigger logic and the event selection criteria are explained in this chapter. The selection of the final sample using the jet finder is described in the next section after the jet finder is defined. For this study, the 2624 nb^{-1} of 1994 HERA positron-proton collision data are used.

5.1 Overview of the selection criteria

There are two important characteristics in the hard photoproduction event that is used for the selection criteria. One is the presence of one or more high p_T jet(s) in an event, with the total p_T along the beam direction being balanced. The other is that no scattered electron is found in the CAL since the scattered electron is not expected in the CAL coverage for the low-Q^2 event.

To find the jet, the CAL energy deposit pattern is used(section 5.5). In earlier levels of the trigger, however, there is not enough computing time to perform jet finding. Instead calorimeter activities like the E_T are used. Here E_T is a scalar sum of the $|p_T|$ measured by the calorimeter cell. Since a jet is likely to have one or more charged particles, the event vertex is observed in hard photoproduction. The combination of CAL activity and the existence of the vertex is useful to select the physics event in the trigger (section 5.3, 5.4, 5.5). The other characteristic of the event, the anti-tag condition, is used in offline selection criteria.

Although it is also possible to tag the scattered electron with $Q^2 \sim 0$ using the LUMI electron calorimeter(LUMI-tagged event). It is not required in this study. One reason is that this condition reduces the acceptance of the photoproduction events. The other reason is that this condition limits the W range of the event due to the energy dependence

of the acceptance of the electron counter. About 30 % of the photoproduction event sample has an electron observed in the LUMI electron calorimeter. Since a LUMI-tagged event is sure to originate from photoproduction process, these events are used for a cross check of the normal sample by examining the event properties. This will be discussed in section 7.2.

5.2 Overview of the background rejection

As discussed in section 3.3, the background rate in the HERA experiments reaches to the order of 100MHz and a large reduction factor is required at each level of the trigger.

There are three types of main background sources at the HERA experiment.

1. Beam gas event

   The term "beam gas event" denotes the event from interaction between the beam particles and the residual gas molecules remaining in the beam pipe. Due to the synchrotron radiation from the electron, the vacuum is in the order of 10^{-9} torr in the HERA beam pipe. Thus most of the background comes from beam gas events at HERA, specially from the proton beam.

2. Beam halo muon

   There are muons produced mainly from the decay of pions produced by the interaction of the off-orbit proton beam with the materials around the beam pipe. They run parallel to the beam but far away from the beam axis, penetrating the main detector.

3. Cosmic ray

   The ZEUS detector is not shielded against the cosmic ray which hits the CAL at a rate of O(10kHz).

Most of the background events can be removed by rejecting the event with off timing hit and requiring the vertex from the interaction region. Specially, the timing information from the CAL is a strong tool to reject the background.

The detectors to provide the timing information is FCAL($t_{\rm F}$), RCAL($t_{\rm R}$), the average of all the calorimeters($t_{\rm G}$), C5 counter($t_{\rm C5}$), and SRTD ($t_{\rm SRTD}$) . The timing from the particles in the ep collision at the interaction region is adjusted to the zero timing of each detector. The trigger uses the following conditions to reject the background. Here the word "upstream" and "downstream" indicates the proton upstream and downstream direction, respectively.

(a) Off timing hit in the upstream detectors, $t_{\rm R}$, $t_{\rm C5}$ and $t_{\rm SRTD}$ to remove mainly the proton beam gas events and cosmic rays.

(b) Off timing hit in the upstream detector $t_{\rm F}$ to remove mainly the electron beam gas events and the cosmic rays.

(c) Too large timing difference in $t_{\rm F} - t_{\rm R}$ to remove mainly the beam halo events.

5.3 First level trigger

The trigger logic at FLT is the coincidence of the signals from two component FLTs, CAL (CFLT) [53] and CTD (CTD-FLT). Several vetoes to reduce the background are applied to the logics.

The logic is fulfilled if all of the following conditions are satisfied.

- One of the following conditions on CFLT signal is satisfied(see figure 5.1).

  `CAL_E`(total energy)$\geq$ 15 (GeV)

  `CAL_EMC_E`(EMC energy)$\geq$ 10 (GeV)

  `CAL_Et`(total transverse energy)$\geq$ 11 (GeV)

  `BCAL_EMC_E`(BCAL EMC energy)$\geq$ 3.4 (GeV)

  `RCAL_EMC_E`(RCAL EMC energy)$\geq$ 2.0 (GeV).

- There should be a track found by CTD-FLT coming from the nominal interaction region.

- No beam gas timing is observed or at least one physics timing is observed in the two C5 counters.

- No beam gas timing is observed or at least one physics timing is observed in four SRTD sections.

- No coincidence of the two layers of the VETOWALL is detected.

The CFLT provides coarsely digitized information to GFLT as trigger signals. The CFLT also utilizes the good timing resolution of the CAL and can determine the bunch crossing number of the events. The coverage of the five signals of the CFLT listed above is shown in figure 5.1. The towers around the beam pipe are excluded to reduce the trigger rate due to the high activity from the beam gas background.

The CTD-FLT provides the flag of the tracking information by classifying the event to four types. The classification is based on the total number of tracks and number of tracks from the interaction region defined as $-50 < z < 80$ (cm). In the 1994 running period, the z coordinate obtained from the timing information of superlayer 1 is used for track finding at FLT level.

The C5 counter timing has a strong reduction power against the proton beam gas event. The counter is situated close to the beam pipe at $Z = -3.2$ m and has a response

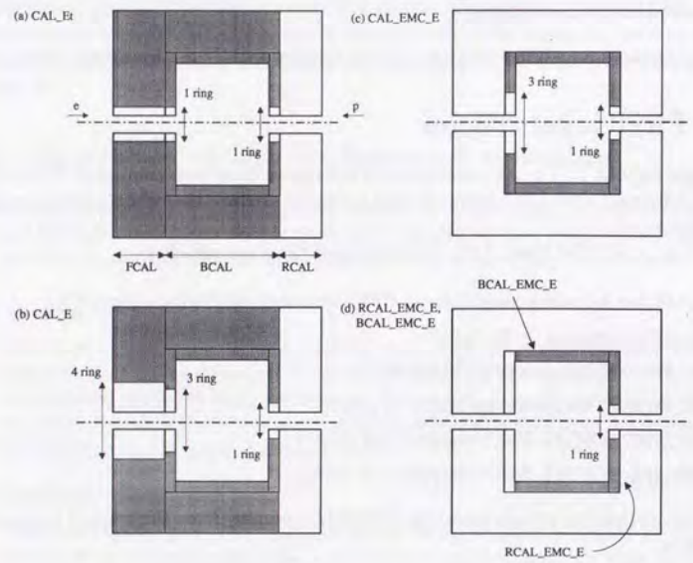

Figure 5.1: The schematic figures of the coverage of the five signals from CFLT. Each figure indicates the ZEUS calorimeter. The shaded regions are used for the signal written aside. The arrow with the term "n ring" denotes the number of the rectanguler ring of the width of n calorimeter towers.

to most of the proton beam gas events from upstream. The timing from the beam gas event is in about 22ns earlier than the event timing from *ep* collision. The SRTD timing, situated in front of the RCAL around the beam pipe, has also a strong power to reduce the beam gas background that originates between the C5 counter and the SRTD. The VETOWALL, covering the upstream side of the main detector, provides the coincidence signal of the two layers to reject the event with penetrating particles.

5.4 Second level trigger

The logical structure of the second level trigger is made up by two parts – global vetoes and the physics filters. First the global veto is applied to all the events to reduce the background rate. Then the physics filter is imposed to select physics events [54].

5.4.1 Vetoes at SLT

The global vetoes remove the event that has an apparent characteristic of the background, using the calorimeter energy deposit and the calorimeter timing from CAL SLT. The trigger logics used in the 1994 run period are as follows.

- The event with the signal from only one PMT in the calorimeter is removed. This logic removes the event that is caused by the discharge of a PMT (spark). The spark event can be distinguished from the normal event by the energy imbalance of the two readouts of a CAL cell.
- The event with empty energy deposit from CAL is removed. The condition of emptiness of the energy deposit of the FCAL, BCAL and RCAL are below 0.8, 0.6 and 0.4 GeV, respectively.
- The event is removed if the average of the timing from the upper half of BCAL is more than 8 ns earlier than that of the lower half. This logic is to reduce the cosmic ray event.
- The event is removed if the calorimeter timing is inconsistent with the timing expected from an *ep* collision. The event is removed when one of the following conditions is fulfilled.
  1. Both t_F and t_R are valid and $(t_F - t_R) > 8$ns (the condition (c) in section 5.2).
  2. t_R is valid and $t_R < -8$ns (cond.(a)).
  3. t_R is valid and $t_R > 8$ns (cond.(a)).
  4. t_F is valid and $t_F > 8$ns (cond.(b)).
- The event with $E - p_Z > 75$ is rejected. The maximum of the $E - p_Z$ at HERA is 55.04 GeV, twice the electron energy if there is no detector smearing.

5.4.2 Physics filters for hard photoproduction at SLT

There were four filters to select the hard photoproduction event in the 1994 running period. Only the event that passed the "High Et" filter is used for this study. The event passes the High Et filter if all of the conditions listed below are fulfilled. Global energy sums from CAL SLT and FLT information make up the filter condition. In calculating the quantities used in the following condition, the vertex position is taken as the nominal interaction point ($X = Y = Z = 0$).

- $E_T^* > 8$ GeV, where E_T^* is the transverse energy excluding the CAL cells inside the 10° cone measured from the incoming proton direction. The vertex of the cone is the event vertex.
- $E - p_Z > 8$ GeV.
- $E - p_Z > 12$ GeV or $p_Z/E < 0.95$
- One or more tracks are found at CTD-FLT

where the $E - p_Z$ and p_Z/E are calculated from the CAL energies.

The first and the second condition save the high-p_T events from the photoproduction and remove the proton beam gas background event, whose hadronic energy is low and most of the activity is seen in the forward region. The low p_T or small-y hard photoproduction events cannot also be saved by these cuts. The third condition is applied to reduce proton beam gas background further. This condition is based on the fact that hadronic energy activity of the proton beam gas event is concentrated around the forward direction. Figure 5.2 shows the distribution of the two quantities used in the third condition. The distribution of the events from the proton pilot bunch is concentrated to the region where the third condition removes, whereas that of the event from colliding bunch is spread to high $E - p_Z$ and low p_Z/E region.

At the beginning of the 1994 data taking period, a looser logic than what listed above was applied to the High Et filter. Therefore the same conditions as listed above are imposed for all the data in offline analysis.

5.5 Third level trigger

The TLT has the same logical structure as the SLT. First global vetoes are imposed to all the input events, then the physics filters are applied. Since TLT uses the computer farm whose machine is the same as used in the offline analysis, a complicated logic like a jet finder can be used.

5.5.1 Vetoes at TLT

The conditions of the vetoes are following.

- The event is removed if it is identified as a spark event. The cell with the energy imbalance $|(E_1 - E_2)/(E_1 + E_2)| > 0.9$ is regarded as a spark cell, where E_1 and E_2 are the energies from the two PMT readouts of a cell. If the event contains only one spark cell and the sum of the CAL energy other than the spark cell is less than 2 GeV, the event is identified as a spark event.

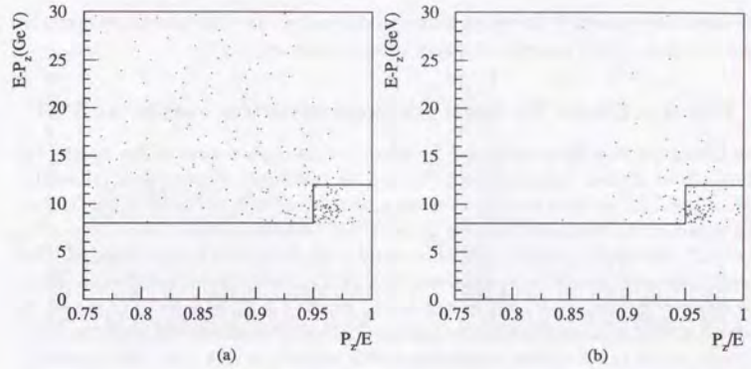

Figure 5.2: $E - p_Z$ and p_Z/E distribution at SLT. (a) shows the distribution of $E - p_Z$ vs p_Z/E from the event of colliding bunch. (b) is the same distribution but the event comes from the proton pilot bunch. The events below the lines are removed at the SLT. The event used in these figures is the event that passed the High Et SLT filter except the third condition, and the onejet TLT filter (see section 5.5.2).

- The event is removed if the calorimeter timing around the beam pipe region of FCAL ($t_{F_{BP}}$) and RCAL ($t_{F_{BP}}$) is inconsistent with the timing expected from the *ep* collision. Only cells with the energy deposit of more than 1.0 GeV are considered for this timing calculation. The event is regarded as a background event if both conditions are fulfilled;
  1. $7\text{ns} < t_{F_{BP}} - t_{R_{BP}} < 15\text{ns}$ (cond.(c))
  2. $7\text{ns} < t_{R_{BP}} < 15\text{ns}$ (cond.(a))
- The event is removed if the calorimeter timing is inconsistent with the timing expected from the *ep* collision. At the TLT the information from FCAL(t_F), RCAL(t_F) and all the calorimeters (t_G) are used. Each timing is taken as valid if two or more cells have the energy greater than 0.2 GeV and the total energy exceeds 1.0 GeV. The event is regarded as a background event if one of the following conditions is fulfilled.
  1. $t_R < -6\text{ns}$ or $t_R > 6\text{ns}$ (cond.(a))
  2. $t_F < -8\text{ns}$ or $t_F > 8\text{ns}$ (cond.(b))

3. $t_F - t_R < -8$ns or $t_F - t_R > 8$ns (cond.(c))

4. $t_G < -8$ns or $t_G > 8$ns .

- The event is removed if the muon finder performed at the TLT identified that the event is due to either a cosmic muon or a beam halo muon.

5.5.2 Physics filters for hard photoproduction events at TLT

There are fifteen physics filters prepared to select the hard photoproduction event. Of these filters a filter named "one jet branch" is used for this study. These filters utilize the advantage of the TLT architecture by running a cone algorithm jet finder EUCTLT on TLT. The detail of the cone algorithm jet finder is discussed in section 6.1.

At the TLT, the event is required to have a vertex by the vertex finder program. The vertex position is used in calculating the quantities used in the following conditions. Then this filter imposes the following requirement to the event: (1) $E_T^* > 5$ GeV, where E_T^* is the transverse energy calculated by excluding the CAL cells inside the 10° cone from the vertex, (2)$E - p_Z > 5$ GeV. These conditions are to reduce the rate from the other SLT filters, and no effect to the events from High Et SLT filter.

Then a further condition using the EUCTLT jet finder information is applied to select the photoproduction sample with at least one high p_T jet. For the one jet branch, the event is taken if at least one jet is found which fulfills

1. $E_{Tjet} > 6.5$ GeV and $2.0 \leq \eta_{jet} < 2.5$, or

2. $E_{Tjet} > 5.5$ GeV and $\eta_{jet} < 2.0$.

The reason to use the one jet branch for the dijet event study is to trigger the event with the leading p_T jet.

After the event passes the TLT, the event is sent to the mass storage and reconstructed offline. No more filters are applied in the reconstruction.

5.6 Offline event selection

Since there are still remaining backgrounds from beam gas interactions and cosmic rays even after the TLT, two selection criteria are applied.

1. $-37 < z < 43$,

   where z is the vertex position along the beam axis. The z distribution is fitted by a Gaussian using dijet event and $\pm 4\sigma$ is taken as a fiducial region. Figure 5.3(a) shows the vertex distribution of the events from colliding bunches, proton pilot bunches and electron pilot bunches. Most of the events in tail of the distribution are explained by the beam gas background.

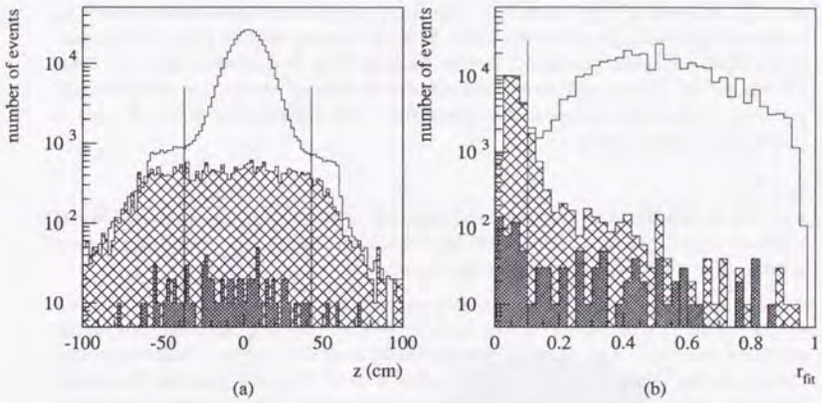

Figure 5.3: The distribution of (a) z position of the vertex and (b) r_{fit}. The solid histogram shows all the events from the one jet branch. The hatched area contains the events from the proton pilot bunch, and the shaded area those from the electron pilot bunch. The numbers of the events in proton pilot and electron pilot bunch are weighted to that of colliding bunch by the ratio of the currents of each bunch type. The edge of the distribution observed at around ±60 cm is due to the cut at the TLT.

2. $r_{fit} < 0.1$, where r_{fit} is the ratio of the number of tracks fitted to the vertex to the total number of tracks.

   In some case, the beam gas event is triggered as the overlap of the two events. There are events consisting of the combination of a vertex in the interaction region and the beam gas event with large calorimeter energy and large number of tracks from the upstream. This contribution can be removed by rejecting the event with low r_{fit}. Figure 5.3 (b) shows the distribution of r_{fit}. The peak near zero can be explained by the proton beam gas background (hatched histogram).

Further selection criteria are applied to reduce the background process from the other physics processes, namely the high-Q^2 processes. To remove the CC event, $r_{cc} = \not{p}_T/\sqrt{E_T} < 1.5(\mathrm{GeV}^{1/2})$ is applied. Here $\not{p}_T$ denotes the missing p_T by the CAL. This quantity indicates the missing p_T scaled by the resolution of the calorimeter. The distribution is presented in figure 7.8. To remove the NC event, two conditions are imposed.

(3) $(E - p_Z)/2E_e < 0.7$.

Here $E - p_Z$ is calculated by the CAL and including any electron candidates. In this case, $E - p_Z \sim 2E_e$ for the high-Q^2 event where the scattered electron is found by CAL, whereas $E - p_Z = 2yE_e \simeq 2E_\gamma$ for the photoproduction event where no scattered electron is found in the CAL. This cut corresponds to $y_{JB} < 0.7$ in case of the photoproduction events. Therefore this cut may be quoted as '$y_{JB} < 0.7$' for the simplicity. This condition removes almost all high-Q^2 events, but also the high y events of photoproduction at the same time. The distribution of the $E - p_Z$ is presented in figure 7.9(b).

(4) $y_e > 0.7$,

where y_e is calculated from energy and angle of an electromagnetic cluster. This is imposed only if one or more electron candidates are found. The lowest y_e is taken if more than one electron candidate are found.

After imposing the selection $y_{JB} < 0.7$, there remains the background from NC events. The further reduction can be achieved by the anti-tag condition of the scattered electron. The photoproduction event may also contain electromagnetic clusters in the CAL, due to an electron, photon or π^0 from the hadronic final state like a jet. In this case the energy of the electromagnetic cluster tends to be much smaller than that of the scattered electron. Thus y_e, which is different from the kinematical variable y, is high. On the contrary, the cross section of the NC process falls off by $1/y^2$, most of y_e of the NC event is low. For these reasons, the event with $y_e > 0.7$ is regarded as a photoproduction event and saved. The rest are regarded as a scattered electron and rejected. The distribution of the y_e is shown in figure 5.4.

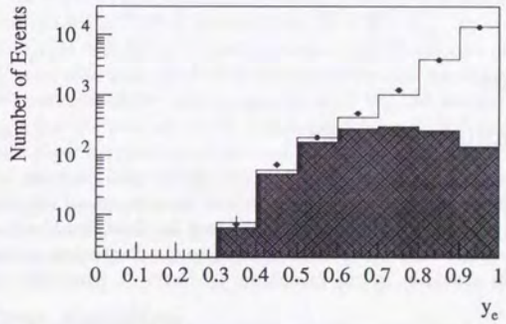

Figure 5.4: The distribution of y_e of the dijet events. Here the dijet event is defined as (1) the event that passed all the event selection criteria described in this section, except $y_e > 0.7$, (2) two or more jets of $-1 < \eta_{jet} < 2$ and $E_{T_{jet}} > 5$ GeV . The PUCELL jet finder, which is discussed in section 6.1, is used on detector level. The dot is the data, the solid histogram is Monte Carlo of the sum of NC and photoproduction, and the hatched histogram is Monte Carlo of NC only. The Monte Carlo is normalized to the number of events of the data.

Chapter 6

Jet Finding and Energy Correction of the Jet

6.1 Jet finder

6.1.1 The definition of the jet

As mentioned in section 4.1, the final state of the quark and gluon cannot be measured directly due to the colour confinement. Only the final state hadrons, which are colour neutral, can be measured by the experiment. In treating the final state hadrons, a *jet* is defined as an event property that has a close relation to the final state quark or gluon. The definition of the jet should be by the algorithm, *jet finder*, to clusterize the hadronic energy flow.

The jet finder should have two conditions. One is that it should be applied to any type of final state: partons in any order of the perturbation theory, hadrons or detector responses. The other is that the reconstructed kinematical quantities from the jet finder have close relationship to that of the parton to study. With these conditions, a jet found in the detector can be associated to what we are interested in. The two types of algorithms fulfilled these two conditions and are commonly used : the cluster algorithm and the cone algorithm.

6.1.2 Cluster algorithm

The idea of the cluster algorithm is that the iteration of merging two close clusters results in several well-separated jets. The merging procedure starts from a psuedoparticle four momentum p_i, which can be either a real particle momentum on the hadron level or the detector information like a track momentum or a calorimeter cell energy. For each combination of the two pseudoparticles a "distance" d_{ij} is calculated. The distance represents the remoteness of the two particles. Then the minimum d_{ij} is picked up, for which the two pseudoparticles are merged and a new pseudoparticle is formed with the four-momentum p_k calculated by the function $p_k = f(p_i, p_j)$. The function f is called a recombination

scheme. After merging, the distances for all the combinations of two pseudoparticles are calculated again and then merged further.

In the JADE type algorithm [55], which is the original form of the cluster type algorithm the invariant mass of the two pseudoparticles is used as d_{ij}. In this definition, the minimum of d_{ij} can be the two low momentum pseudoparticles that are far apart in the angular space. Recently the $k_\perp$ (Durham) algorithm [56] overcame this problem by using the definition of d_{ij} as

$$d_{ij} = 2\ \min(E_i, E_j)(1 - cos\theta_{ij}),$$

where E_i and E_j are the energy of two clusters, and θ_{ij} is the angle between two clusters. By this definition, the softest pseudoparticle tends to be merged first to the spatially nearest pseudoparticle. For the recombination scheme the addition of the four momentum $p_k = p_i + p_j$, the simplest one, is commonly used. Another way is to make the pseudoparticle massless after adding the four momentum; $E_k = E_i + E_j, \quad p_k = E_k \cdot (p_i + p_j)/|\mathbf{p}_i + \mathbf{p}_j|$.

Usually the jet is defined by stopping merging when the minimum d_{ij} is above a certain threshold. The number and physical quantities of the jets are determined by the number and the four-momenta of the pseudoparticles after the last merge. It is also possible to stop merging when the number of the pseudoparticles is as is desired to define jets.

The cluster algorithm has an advantage that all the particles are assigned to the jets. Thus a good reconstruction of the kinematical variables can be achieved. In case the event contains the beam remnant or the underlying event, however, the reconstruction is distorted by the particles from these final states. Therefore the cluster type algorithm has been used mainly in e^+e^- experiment.

6.1.3 Cone algorithm

The idea of the cone algorithm is to find the maximum energy in a fixed cone radius out of the pseudoparticles distribution. Usually the cone is formed in the $\eta - \phi$ space, and the maximum transverse energy is searched for. Hence the algorithm is invariant with the boost along the beam axis and has been mainly developed and used in hadron-hadron collider experiments. The actual algorithm is the following. First a seed for the maximum search is chosen by selecting a pseudoparticle or a cluster of the pseudoparticles whose transverse energy is above the threshold. Next a new axis of the cone is calculated by using the pseudoparticles inside the cone, $\delta R = \sqrt{(\eta_{cone} - \eta_i)^2 + (\phi_{cone} - \phi_i)^2} < R_{cone}$. Here η_{cone} and ϕ_{cone} are the azimuthal angle and the pseudorapidity of the cone center, and the ϕ_i and η_i are those of the psuedoparticle. R_{cone} denotes the cone radius, which is a fixed parameter of the finder. Then a new cone around the new axis is formed and the procedure is repeated. The iteration is stopped by certain conversion criteria. The cone with the transverse energy above the given threshold is selected as a jet. When there is an overlap between the two cones, the algorithm decides whether the two cones are merged or kept apart, judging from the fraction of the overlapped energy. The condition on this division and the way to divide the energy between the two cones varies from algorithm to algorithm.

Usually the 'Snowmass convention' [57] is used in calculating the transverse energy and the cone axis in $\eta - \phi$ space, to make the algorithm unambiguous:

$$E_{T_{cone}} = \sum_i E_{T_i},$$

$$\eta_{cone} = \frac{\sum_i E_{T_i}\eta_i}{\sum_i E_{T_i}},$$

$$\phi_{cone} = \frac{\sum_i E_{T_i}\phi_i}{\sum_i E_{T_i}}.$$

The jet axis parameters, η and ϕ are calculated weighted by E_T so that the parameters are Lorentz invariant to the boost along to the beam axis. There is another advantage using the cone algorithm in hadron-hadron collision experiments. Since the beam remnant is far from the high-E_T jet in $\eta - \phi$ space and the transverse energy of the beam remnant is very small, its effect is also very small.

PUCELL cone algorithm

The PUCELL algorithm [58], used in this study, is a variation of the cone algorithm jet finder. It is operated in the $\eta - \phi$ space and E_T, η and ϕ are calculated according to the Snowmass convention. A single pseudoparticle like a single cell or a hadron is used as a seed if the transverse energy is above the threshold. In case of the overlap, two cones are merged if 75% of the transverse energy of the smaller transverse energy cluster is overlapped. Otherwise the two cones remain apart, and the pseudoparticles inside the cone are assigned to the cone whose axis is closer in the $\eta - \phi$ space.

6.2 The correction of the jet

In this section, first it is discussed to which level the detector information is corrected, then the correction procedure is explained. The correction procedure of the cross section is made up by two parts: first the correction of the jet is performed, and then the acceptance correction is applied to the distributions based on the corrected jet.

6.2.1 Levels of the correction

As discussed in section 4.1, the current theoretical framework describes the formation of the hadronic final state in two steps – the parton shower and the fragmentation. In addition to it there is another step, the detector smearing, between the hadronic final state and the experiment. Thus jets can be studied on four different levels as following [59]:

1. partons from the calculation of the matrix element (parton level),

2. partons after the parton shower (parton shower level),

3. hadrons after the fragmentation (hadron level), and

4. the detector response (detector level).

The correction of the jet quantities from one level to another level is done by applying a correction procedure. The correction factors in the procedure are taken from the model that simulates the transition of the levels. Thus usually the correction is model dependent. A good correlation, however, is expected between the hadron level jet and the detector level jet for the following reasons. First, the correction depends only on the hadronic energy flow of the jet, and does not depend largely on how the jet is produced in the underlying physics model. Second, the model dependent part is the detector simulation and is well understood through the various other studies.

On the contrary, the correction from the hadron level to the parton shower level or the parton level cannot avoid the model dependence. The spatial or momentum information of the underlying level is smeared by the model dependent physics assumption like the parton shower or the fragmentation model. Further, the correction is completely different if the multiple interaction model is employed.

In this thesis, to avoid the large model dependence, the jet cross section is corrected back to the hadron level. The cross section is presented as the cross section using the jet found at hadron level.

6.2.2 The correction procedure

The simplest way to correct back the measured detector level cross section to the hadron level cross section is to calculate the bin-by-bin correction factor using a Monte Carlo simulation. The hadron level cross section is calculated by the formula

$$\sigma_i^{had} = \frac{n_i^{had}}{n_i^{det}}\sigma_i^{det}, \tag{6.1}$$

where σ_i^{det} is the detector level cross section in the $i-$th bin, σ_i^{had} is the corrected cross section in the $i-$th bin, and n_i^{had} and n_i^{det} are the number of the MC events in the i-th bin at the hadron level and the detector level, respectively.

The correction factor, n_i^{had}/n_i^{det}, corrects any detector effect like the trigger efficiency or the jet energy loss, and the extrapolation of the kinematical region. The procedure is valid only if (1) the bin-to-bin migration is simulated by the MC correctly, (2) the shape of the histogram to be corrected agrees with the MC reasonably.

One way to minimize this systematic uncertainty in bin-by-bin correction is to minimize the bin-to-bin migrations. In case of the jet cross section, this can be achieved by correcting the jet quantities, which is the binning variable of the jet cross section. The jet quantities are corrected first by using the correlation of these quantities between the hadron and the detector level. Then the "corrected" cross section, σ_i^{cor} is calculated based

on the corrected jet quantities. The correction factor is applied to σ_i^{cor} to calculate the hadron level cross sections according to the formula

$$\sigma_i^{had} = \frac{n_i^{had}}{n_i^{cor}} \sigma_i^{cor} \tag{6.2}$$

where n_i^{cor} is the number of the MC events in the i-th bin filled by the corrected jet.

The correction on the jet quantities can be applied only statistically; the shift of the mean value of each quantity can be corrected but the smearing of the quantity cannot be corrected. Therefore it is impossible to reproduce the hadron level histogram only by the correction of the jet even if the acceptance of the event is one. The remaining bin-to-bin migration due to the smearing of the jet quantity is corrected by the correction factor.

In the following section, the jet correction procedure between the hadron and the detector level is explained. To parametrize the correction, the jets from the hard photoproduction events generated by PYTHIA as described in section 4.2 are used. To obtain the detector information, the events passed through the ZEUS detector simulation.

In the jet energy correction procedure, the jet found by the PUCELL jet finder is used to define the jets on both the hadron level and the detector level. For the hadron level, the final state hadrons are used as an input set of the finder. The hadron with the $p_T > 0.3$ GeV is used as a seed. For the detector level, the calorimeter cell energy is used as an input. The cell is treated as a massless particle: the momentum of the cell is equal to the energy and the momentum vector taken as parallel to the vector from the vertex to the cell. The position of the cell is taken from the center of the gravity. The calorimeter cell with the $p_T > 0.3$ GeV is used as a seed.

6.2.3 The correlation of the jet quantities between hadron and detector level

To see the jet energy correlation between the hadron and the detector level, the detector level jet with $E_T^{det} > 8$GeV, $-1 < \eta^{det} < 2$ is selected. The matching jet between the detector and the hadron level is searched within the cone of $R = \sqrt{(\Delta\eta)^2 + (\Delta\phi)^2} = 1$. Here the hadron level jet is the jet with $E_T^{had} > 4$ GeV, which is required as a minimum for the E_T of the jet to be regarded as a jetty object. The nearest hadron level jet is taken when more than one jet are matched. Figure 6.1 shows the probability that the detector level jet has no matched jet (solid line) and two jets (dashed line) on hadron level, with respect to η^{det}. The unmatched probability is very low ($< 0.5\%$) in the region of $\eta < 2$. The probability that two close jets on hadron level are observed as one jet in the detector level is high ($\sim 3\%$) and increases in the region $\eta > 2$.

Figure 6.2 shows the correlation between the jet quantities, $E_{T_{jet}}$, η_{jet}, ϕ_{jet} with respect to each of three quantities. The vertical axis shows the difference between the hadron and the detector level quantity. Only the detector jet that has a matching jet on the hadron level is plotted.

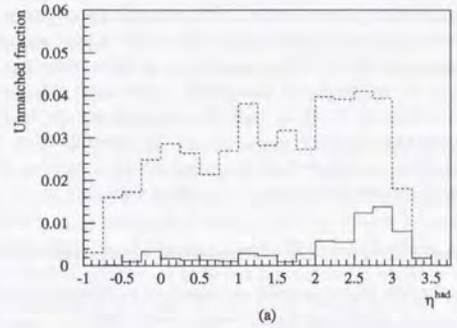

Figure 6.1: The matching probability between the detector level jet and the hadron level jet. The solid line shows the probability that no hadron level jet is matched with the detector level jet with E_T >8.0. The dashed line shows the probability that two hadron level jets are matched.

The difference of η depends on η itself, but the fluctuation is very small compared to the standard deviation of the difference, and the mean value is centered around zero. The effect of the fluctuation can be avoided by taking a much larger width of binning than the amplitude of the fluctuation. There is no systematic shift in ϕ reconstruction and the mean is centered around zero. On the other hand the difference of E_T, $E_T^{had} - E_T^{det}$, becomes larger as E_T^{had} becomes large. The shift depends on E_T itself and η as well. The energy loss from E_T^{had} to E_T^{det} is mainly due to the energy loss in dead materials in front of the CAL.

From these examinations, the E_T of the jet should be corrected by a function of E_T and η, while no correction is needed from the detector to hadron level for η and ϕ:

$$E_T^{cor} = C(E_T^{det}, \eta^{det}) \times E_T^{det} \tag{6.3}$$
$$\eta^{cor} = \eta^{det} \tag{6.4}$$
$$\phi^{cor} = \phi^{had}, \tag{6.5}$$

where C is the correction function, and E_T^{cor}, η^{cor} and ϕ^{cor} are the corrected E_T, η and ϕ of the jet, respectively.

6.2.4 Parametrization of the jet energy correction

The determination of the jet E_T correction function $C(E_T^{det}, \eta^{det})$ is the first important step in calculating the hadron level cross section. In principle the difference between the energy correction parametrizations is absorbed by the acceptance correction if the MC used in the correction agrees perfectly with the data. In reality, however, the agreement of the MC and the data is not perfect and the result depends on the energy correction function. Therefore it is necessary to show that the dependence of the corrected cross section on the energy correction function is small. In this section three possibilities of the energy correction function are presented by using different MC or different fitting procedures. The effect on the cross section is discussed in section 8.3.

6.2.5 The parametrization of the correction function

The idea of the parametrization of the correction function is originally used in the measurement of the inclusive cross section at ZEUS experiment [26].

To determine the function $C(E_T^{det}, \eta^{det})$, first the profile of the ratio of E_T^{det} to E_T^{had} is made.

$$E_T^{det} = \langle E_T^{det}/E_T^{had} \rangle_{\eta^{had}, E_T^{had}} \times E_T^{had} \tag{6.6}$$

Then the function is determined by inverting the profile:

$$C^{-1}(E_T^{had}, \eta^{had}) = \langle E_T^{det}/E_T^{had} \rangle_{\eta^{had}, E_T^{had}}. \tag{6.7}$$

The substitution of the η^{det} to η^{had} in inverting the profile C^{-1} to C is justified since the correlation between two values is good. To avoid a complex two-dimensional function of η and E_T, first the η^{had} region, $-1 < \eta^{had} < 2$, is divided in equidistant twelve bins. Then for each of the twelve bins the E_T dependence of the ratio is fitted by an analytic function. Thus the parametrization is discrete to the η^{had}, which is reasonable since the dependence of the parametrization on η^{had} is not steep.

Figure 6.3 shows the profile of the ratio $\langle E_T^{det}/E_T^{had} \rangle$ with respect to E_T^{had} by the PYTHIA model with the statistical error on the mean (solid point and error bar). The profile is made by the jet to be measured: the hadron level selection criteria ($E_T^{had} > 8$ GeV and $-1 < \eta^{had} < 2$) are applied. The jet is required to have a matched detector level jet with $E_T^{det} > 6$ GeV within $R = 1$ The profile shows a relatively flat dependence on E_T. The fit to the profile as a function of E_T is also drawn by a solid curve. For the parametrization of the fit, the empirical function

$$\langle E_T^{det}/E_T^{had} \rangle_{\eta^{had}, E_T^{had}} = \frac{a_i/E_T^{had} + (1 + b_i)}{1 - b_i}$$

is used. Here the a_i and b_i are the fitting parameters of the $i-th$ bin of η^had. The function comes from the formula $E_T^{det} - E_T^{had} = a_i + b(E_T^{det} + E_T^{had})$; the difference between the hadron and the detector level jet E_T is fitted by a line. With only two parameters, this function fits to the data well as is shown in figure 6.3.

The parametrization dependence of the jet energy correction

In calculating the profile of the ratio $\langle E_T^{det}/E_T^{had} \rangle$, the two-dimensional correlation plot of E_T^{det} to E_T^{had} is sliced in parallel to E_T^{det} and the average of the histogram of each slice is calculated. Suppose that a "real" correlation curve between E_T^{had} and E_T^{det} is fitted. Due to the exponential fall of the E_T distribution of the hard photoproduction event, there are more events below the "real" correlation in the slice. Therefore the average of the slice can be shifted toward the lower E_T.

To estimate this effect, the jet energy correlation is fitted by another way. The profile is calculated in $E_T^{had} - E_T^{det}$, as the function of $E_T^{had} + E_T^{det}$; the slice is 45° rotated clockwise. Since the events on the two-dimensional plot of E_T^{had} and E_T^{det} concentrates approximately around $E_T^{had} \sim E_T^{det}$, the slice parallel to the $E_T^{had} - E_T^{det}$ axis is perpendicular to the rapidly falling distribution. Therefore it is expected that the shift of the profile is smaller than the original scheme. The distribution is fitted by a second order polynomial. Figure 6.4(a) and (b) shows the example of the fitting with this profiling. The result of the fitting is translated to the $C(E_T^{det}, \eta^{det}) - E_T^{had}$ plane and drawn in Figure 6.5 by the dotted curve. Comparing with the nominal parametrization, drawn by the solid curve, this fitting shows a lower correction factor. This is expected since the shift from the nominal parametrization is to the higher direction in C^{-1}, hence lower in C.

The model dependence of the jet energy correction

To see the difference of the energy correction between models, HERWIG MI is used. The example of the fitting to the profile is shown in figure 6.4. The result is plotted in Fig 6.5(dashed line). The difference of the energy correction between the HERWIG MI and the PYTHIA model is smaller than the difference of the fitting procedure. It is seen that the different energy flow of the jet, i.e., HERWIG MI and the PYTHIA model cause little differences in the energy correction function(see also section 7.3 for the energy flow differences of the two models).

The correction factor in figure 6.5 is high in low–E_T region and becomes smaller as E_T becomes high. The factor is large around $\eta = -1$ and $\eta = 1$. This is due to that there are more dead materials in these regions than the other regions.

6.2.6 The application of the correction

It is meaningful to check that the energy correction parametrization obtained in this section reproduces the E_T distribution of hadron level well from the detector level jet.

The result of the correction with the standard parametrization is presented in figure 6.6 as a difference of E_T from the hadron jet before and after the correction. The E_T classification to ten histograms is used in the binning for the cross section of $d\sigma/dE_T d\eta_1 d\eta_2$ (see figure 7.1). The width of the binning in each slice is taken from the E_T resolution in the low E_T region, whereas the width is wider than the resolution in the higher E_T region since the event statistics is low. The center of the corrected histogram peaks around zero.

The inclusive $E_{T_{jet}}$ distribution after the correction is shown in figure 6.7 for the entire region and three partial regions of η_{jet}. The corrected distribution is closer to the hadron level distribution than that of the detector level though the overcorrection is seen in general.

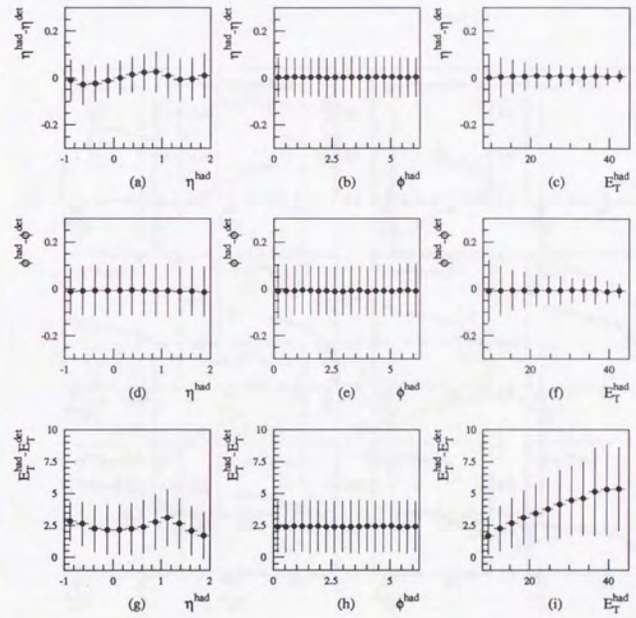

Figure 6.2: The correlation of the hadron and detector jet quantities, η_{jet}, ϕ_{jet} and $E_{T_{jet}}$, estimated by PYTHIA. The correlation is shown as a profile of the difference between the hadron and the detector level quantities. (a),(b),(c): $\eta^{had} - \eta^{det}$ vs η^{had}, ϕ^{had} and E_T^{had}. (c),(d),(e): $\phi^{had} - \phi^{det}$ vs η^{had}, ϕ^{had} and E_T^{had}. (f),(g),(h): $E_T^{had} - E_T^{det}$ vs η^{had}, ϕ^{had} and E_T^{had}. The error bar indicates the standard deviation of the distribution. The scale of E_T is in GeV.

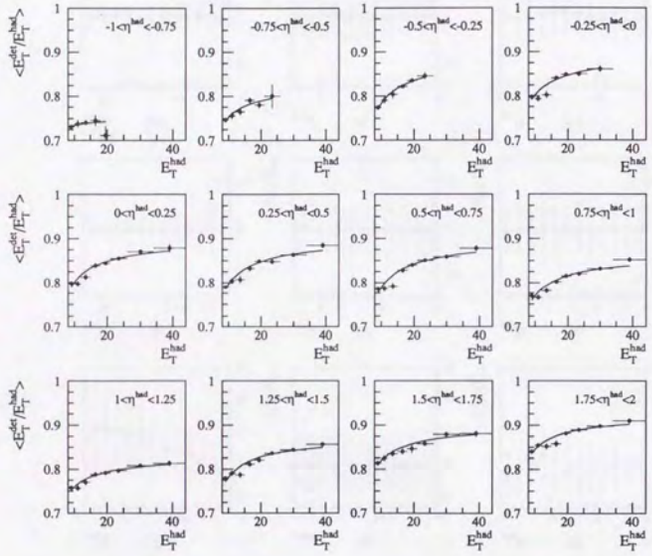

Figure 6.3: The profile of the transverse energy ratio of the detector to the hadron level jet and the fit to the profile. PYTHIA is used for obtaining the profile. The twelve plots correspond to each bin of η. The scale of E_T is in GeV.

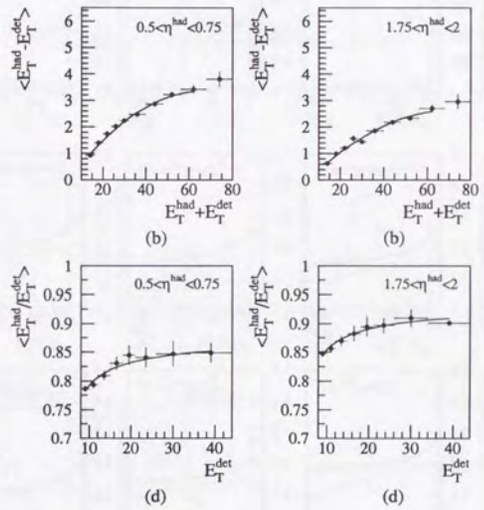

Figure 6.4: The example of the profile of the jet energy correlation. In (a) and (b), the profile is made on $(E_T^{had} - E_T^{det})$ - $(E_T^{had} + E_T^{det})$ space, using PYTHIA. In (c) and (d), HERWIG MI is used to make the profile by the standard parametrization. In both cases, the selection criteria for the event sample used in this figure are the same as figure 6.3. The scale of E_T is in GeV.

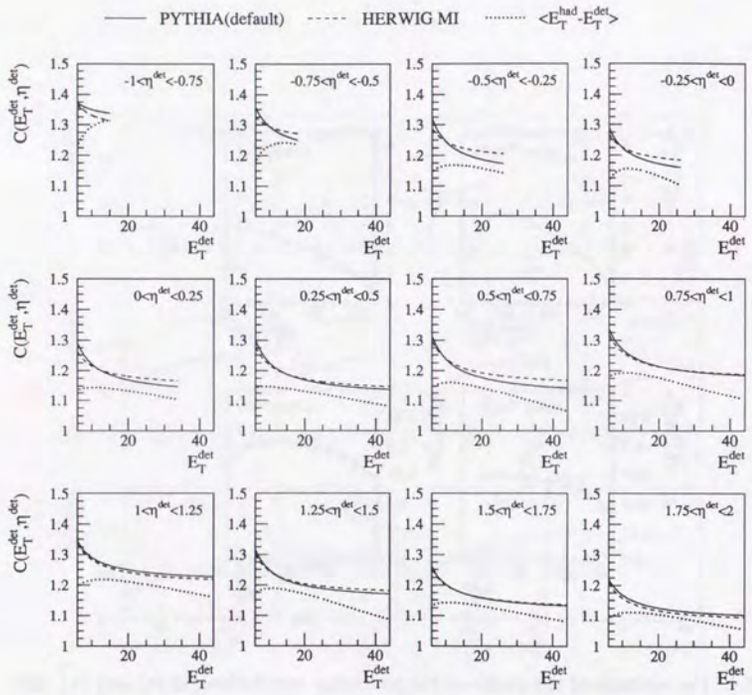

Figure 6.5: The energy correction curve of different parametrizations and models. The solid curve is the default parametrization by PYTHIA, the dashed curve is from HERWIG MI and the dotted curve is from the $\langle E_T^{had} - E_T^{det} \rangle$ parametrization using PYTHIA. The scale of E_T is in GeV.

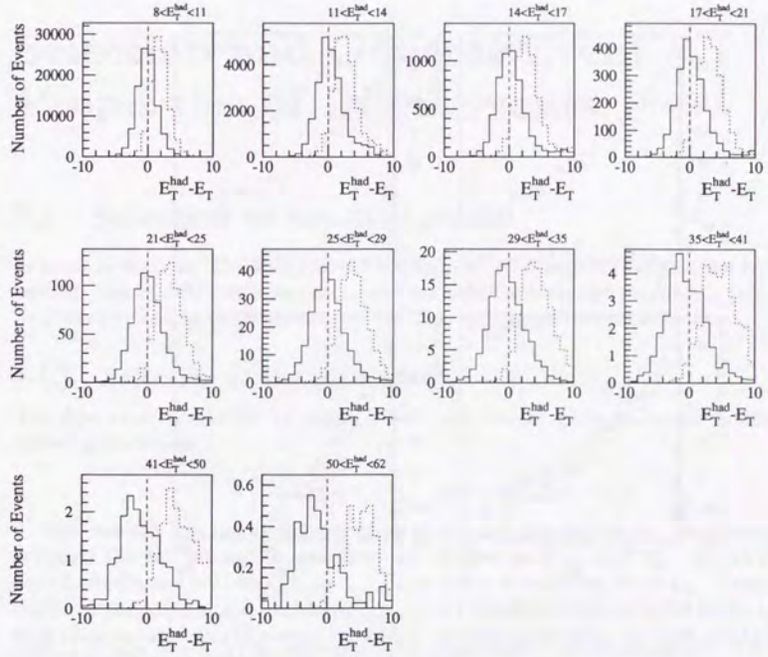

Figure 6.6: The distribution of $E_T^{had} - E_T^{cor}$ (solid) and $E_T^{had} - E_T^{det}$ (dotted) of PYTHIA. Each histogram represents the histogram of E_T^{had} slice. The number of the events is normalized to the luminosity of the data. The scale of E_T is in GeV.

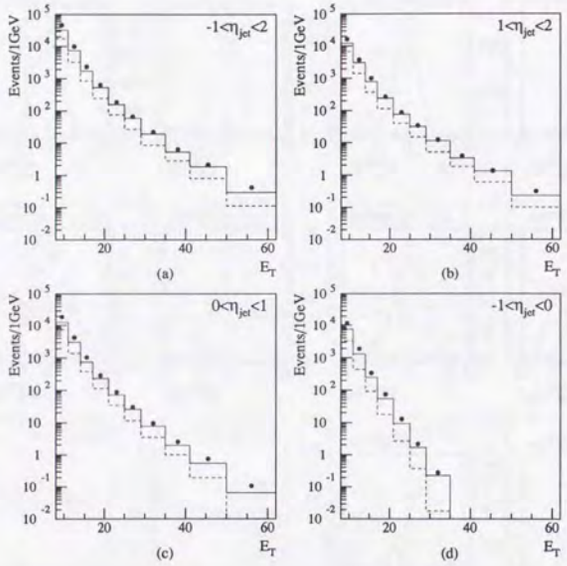

Figure 6.7: The inclusive $E_{T_{jet}}$ distribution after correction of (a) $-1 < \eta_{jet} < 2$, (b) $1 < \eta_{jet} < 2$, (c) $0 < \eta_{jet} < 1$, (d) $-1 < \eta_{jet} < 0$. The detector level MC(PYTHIA) jet is corrected by the correction function and compared with the hadron level jet distribution. The dot is the distribution of E_T^{cor}, the dashed histogram is E_T^{det}, and the solid histogram is E_T^{had}. The scale of E_T is in GeV.

Chapter 7

Selection and General Event Properties of Dijet Events

7.1 Selection of the dijet event

In previous sections, the selection criteria and the jet energy correction have been described. Now the kinematical region to measure $d\sigma/dE_T d\eta_1 d\eta_2$ and $(d\sigma/d\eta_2)|_{E_T > E_T^{thr}, \eta_1}$ can be defined by taking the acceptance of the selection criteria into consideration.

7.1.1 Selection of the dijet event

The dijet event is selected by taking events with two or more jets which fulfilled the following conditions:

$$-1 < \eta^{cor} < 2, \quad E_T^{cor} > 8 \text{ GeV}. \tag{7.1}$$

The selected jets are sorted according to E_T and the highest E_T jet (leading jet) is named the first jet and its quantities are denoted as η_1, ϕ_1 and E_{T_1}. In calculating $d\sigma/dE_T d\eta_1 d\eta_2$ and $(d\sigma/d\eta_2)|_{E_T > E_T^{thr}, \eta_1}$, E_T is chosen as a leading $E_T = E_{T_1}$. Using these events, $d\sigma/dE_T d\eta_1 d\eta_2$ and $(d\sigma/d\eta_2)|_{E_T > E_T^{thr}, \eta_1}$ are calculated and corrected to the hadron level cross sections. In calculating the hadron level cross sections, the dijet events in the hadron level are selected with two or more jets of

$$-1 < \eta^{had} < 2, \quad E_T^{had} > 8 \text{ GeV}. \tag{7.2}$$

The high-E_T jets are chosen because one can see the perturbative QCD effect clearly, and the jet energy correspondence to the hadron level is good. The maximum rapidity is chosen to reduce the effect from the forward energy flow of the proton remnant that is not well understood for the moment. The minimum rapidity corresponds to the kinematical limit (see also figure 7.1 and 7.2).

After the selection of eq. 7.1 with the energy correction on the jet, 22334 events are selected. Among these events, one event is from an empty bunch, one event is from

a proton pilot bunch and no event is seen from the electron pilot bunch. Considering the bunch type and current ratio, the expected number of events produced from the background not originating from the *ep* collision is less than 0.5%. The contribution from DIS events to the dijet event is estimated by DIS MC. As a result, about 250 events are expected to pass the selection and dijet criteria (1.4% of the total sample).

The binning of the $d\sigma/dE_T d\eta_1 d\eta_2$ is defined as follows. First the rapidity space (η_1, η_2) is divided to nine regions by binning η_1 and η_2 with the bin width of unit rapidity. In defining the E_T binning, the bin width is taken approximately as the resolution of the E_T in the low E_T region (< 41 GeV), whereas the bins in the high-p_T region are chosen by statistical reason. Figure 7.1 shows the event distribution of the dijet event after the jet energy correction. The definition of the first and the second jet is exchanged and the event is plotted twice. Here the three variables of the dijet events, E_T^{cor}, η_1 and η_2, are shown by classifying the events to six regions according to the first jet rapidity bins and the cut $x_\gamma > x_\gamma^{cut}$. Here $x_\gamma^{cut} = 0.75$ is taken(see formula 7.7). The rest of the variables, E_T and η_2, are plotted as a scatter plot. The vertical axis is the leading E_T, and the horizontal axis is the rapidity of the second jet. The binning on η_2 and E_T used in obtaining the cross section, $d\sigma/dE_T d\eta_1 d\eta_2$, is drawn on each scatter plot.

Together with the event distribution, several kinematical limits of the dijet event are shown, assuming $2 \rightarrow 2$ scattering. Two curves (solid and dashed) on the left upper corner of each plot show the upper limit of E_T for the variables indicated. The other two curves (solid and dashed) on the right lower corner show similarly the lower limit of E_T.

Figure 7.2 is the same as figure 7.1 except the binning on $(d\sigma/d\eta_2)|_{E_T > E_T^{thr}, \eta_1}$ is shown. The upper boundary of the boxes is open since the bins are taken above the threshold E_T^{thr}.

Figures 7.3 and 7.4 show two examples of the event display among the selected events. Figure 7.3 is an example of the resolved event of $x_\gamma = 0.20$. In addition to the two high-p_T jets, a photon remnant cluster(11.6 GeV) is seen in RCAL. Figure 7.4 is an example of a very high-p_T direct event of $x_\gamma = 0.97$. Only two high-p_T jets and the proton remnant are observed.

7.1.2 Global kinematical variables

Since y_{JB} of the event is restricted by the selection criteria, the y range of the cross section measurement should be restricted as well. To determine the y range to be measured, the correlation between the y_{JB} and y is plotted in figure 7.5. The dijet events (eq. 7.1) of PYTHIA MC that passed the selection criteria other than the cuts on $E - p_Z$ are shown. It is seen that the reconstruction of y by y_{JB} is about 20% lower. The correlation is different between the resolved and direct samples. The two horizontal dashed lines drawn in the figure indicate the selected region at the TLT. From this correlation and cuts, the measured range for the cross section is determined as

$$0.2 < y < 0.85, \tag{7.3}$$

as drawn by the vertical dashed lines in each plot.

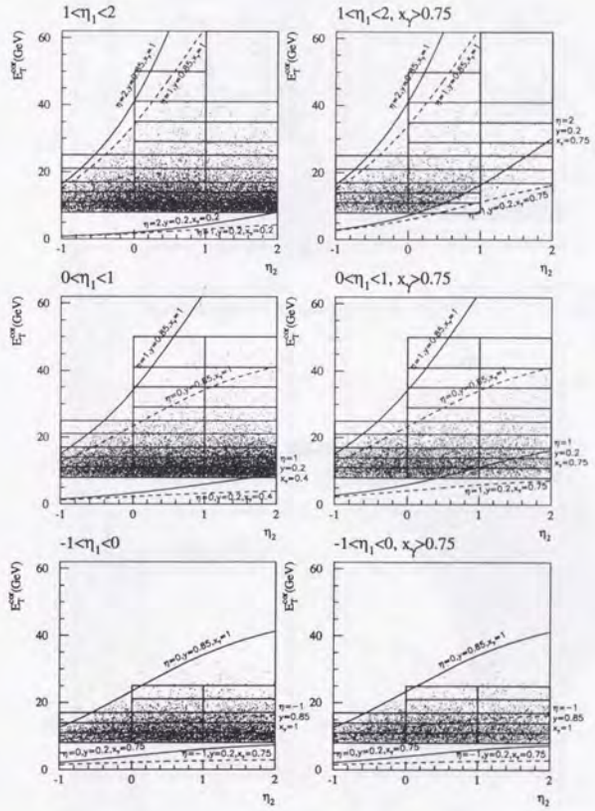

Figure 7.1: Dijet event distribution in $E_T^{cor} - \eta_2$ plane. The kinematical limit of the distribution, by η_2, y and x_γ, are drawn by solid and dashed curves. The boxes drawn in the distribution shows the binning used in $d\sigma/dE_T d\eta_1 d\eta_2$.

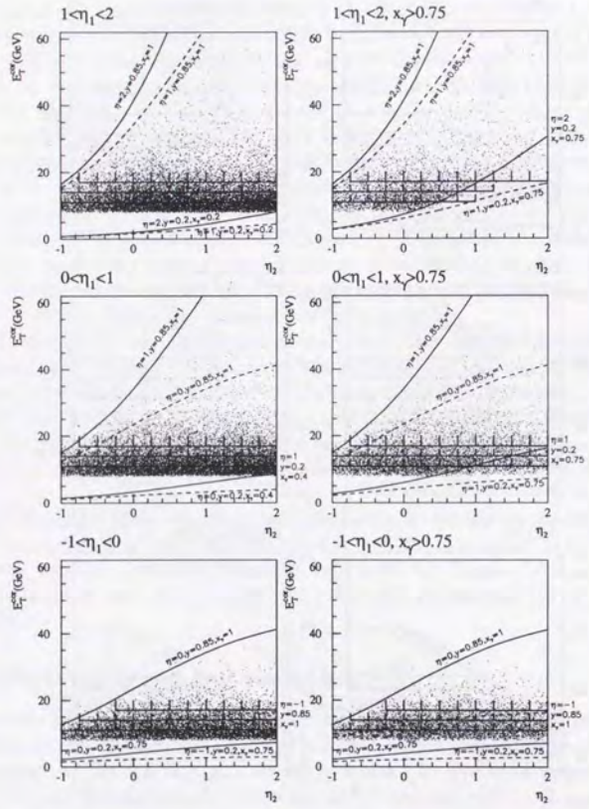

Figure 7.2: Dijet event distribution in $E_T^{cor}-\eta_2$ plane. The lattice drawn in the distribution shows the binning used in $(d\sigma/d\eta_2)|_{E_T>E_T^{thr},\eta_1}$. Others are the same as figure 7.1.

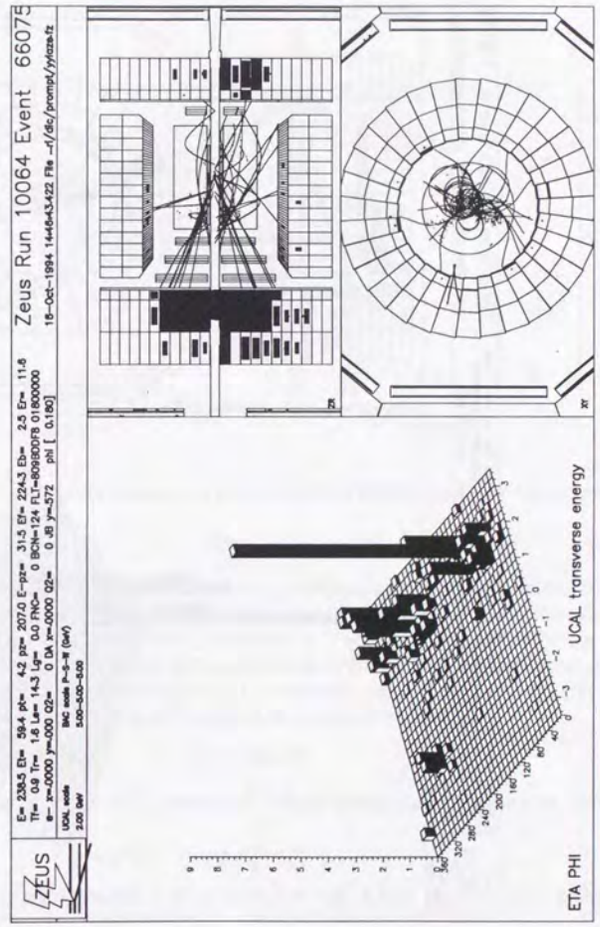

Figure 7.3: An example of the event from the resolved process. x_γ is 0.20. Two clear jets are seen on the LEGO plot. In addition a photon remnant is also seen around $\eta = 2$. The jet properties are: $E_{T1} = 23.4$ GeV, $\eta_1 = 1.96$, $E_{T2} = 22.8$ GeV and $\eta_2 = 2.00$.

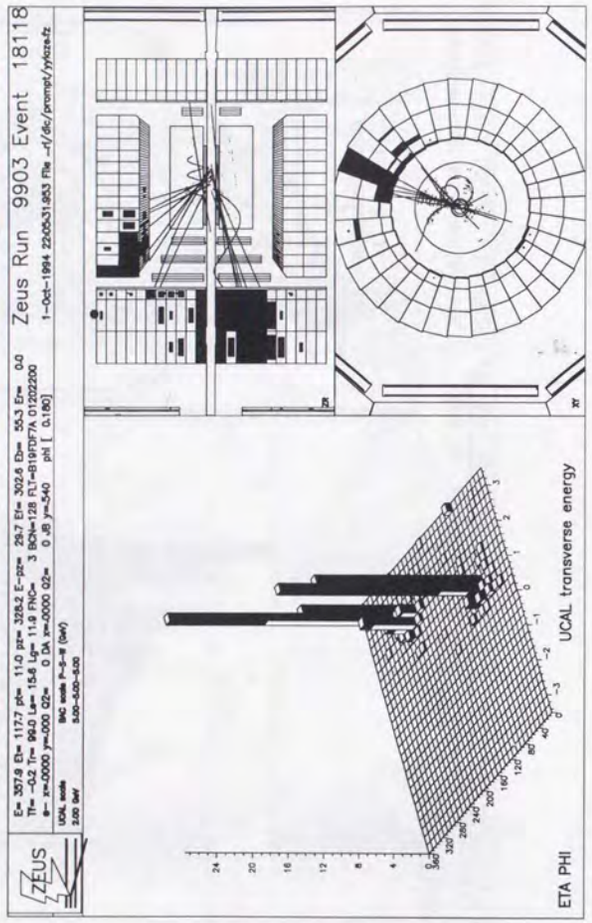

Figure 7.4: An example of very high-p_T event from the direct process. x_γ is 0.97. Two clear jets are seen on the LEGO plot and no photon remnant candidate is observed. The jet properties are: $E_{T1} = 62.5$ GeV, $\eta_1 = 1.99$, $E_{T2} = 50.2$ GeV and $\eta_2 = 0.91$.

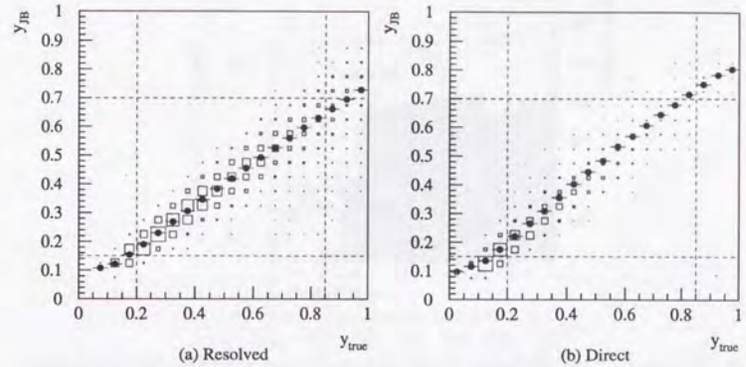

Figure 7.5: The correlation between y_{JB} and y of the PYTHIA events, for the (a) resolved and (b) direct processes.

The Q^2 range is restricted by the anti-tag condition((3) and (4) in section 5.6). The effect of the anti-tag is studied by HERWIG direct process that treats the scattered electron exactly by the matrix element calculation. Figure 7.6 is the distribution of Q^2 of the HERWIG direct events that passed the event selection and dijet selection criteria (eq. 7.1) . The hatched histogram is from the events after imposing the anti-tag condition. The edge on $Q^2 \approx 4$ is seen. The Q^2 range to be measured is defined as

$$Q^2 < 4\,\mathrm{GeV}^2. \tag{7.4}$$

Note that the median of the Q^2 is around 10^{-3} GeV^2 hence most of the events have very low Q^2.

7.2 General event properties of the selected event

7.2.1 The distribution of the quantities on event selection

Figure 7.7 shows the vertex distribution of the distribution of the Z-position of the vertex of the dijet events. The distribution is well reproduced by the MC in the selected region.

In figure 7.8, (a) shows the correlation of E_T and $\not{p}_T$ for the dijet events from the photoproduction process simulated by PYTHIA(dot) and the charged current MC(square). It is seen that the missing p_T of the photoproduction events is much smaller than that of

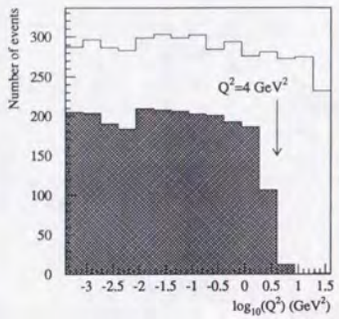

Figure 7.6: The range of the Q^2 before (solid histogram) and after (hatched histogram) imposong a anti-tag condition(see text). The HERWIG direct process is used.

the charged current events where $\not{p}_T \approx E_T$. The photoproduction events can be separated by the cut $r_{CC} < 1.5\text{GeV}^{1/2}$ (below the curve in the plot). (b) shows the distribution $r_{CC} = \not{p}_T/\sqrt{E_T}$ of the data (dot), PYTHIA MC (solid histogram) and charged current event MC (shadowed histogram). The excess in the region $r_{CC} > 1.5$ over the sum of the CC and the photoproduction is mainly due to the cosmic ray shower. The number of events expected from CC MC in $r_{CC} < 1.5$ is 0.6 events.

7.2.2 The global energy

Figure 7.9 shows the global energy distribution used in the selection criteria. The dot indicates the data with all the selection criteria and the dijet selection, the solid histogram is MC(PYTHIA) with all the selection criteria and the dijet selection. The hatched histogram shows the LUMI subsample (the events that has an energy deposit in the LUMI electron calorimeter of $5 < E_{LUMI} < 24.5$ GeV) of the data. The expected number of events from MC is normalized by the integrated luminosity of the data for this study. (a) shows the E_T^* distribution. It is seen that the E_T^* distribution is not well simulated by the PYTHIA MC. The 8 GeV (SLT) and 5 GeV (TLT) threshold in E_T^* in the selection criteria, however, are much lower than the lower edge of the distribution, hence the disagreement of E_T^* does not affect the acceptance calculation. (b) shows the y_{JB} distribution. The MC expectation and the data agree well though the absolute number of events is different. It is also seen that the acceptance of y_{JB} of the LUMI-tagged event begins at around $y_{JB} = 0.3$ and falls at 0.6. (c) shows the p_Z/E distribution and (d) shows the p_Z/E distribution

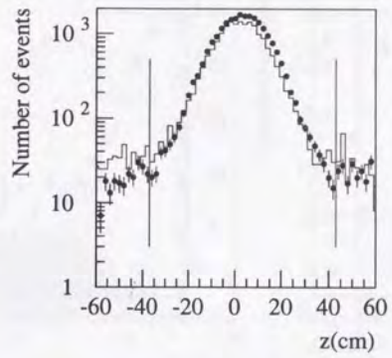

Figure 7.7: The distribution of the Z-position of the vertex of the dijet events. The events that passed all the selection criteria except the vertex cut at the offline selection are shown. The dot is the data and the solid line is the PYTHIA MC. The vertical line shows the fiducial region of the vertex, -37 to 43 cm.

in the range $8 < E - p_Z < 12$, to see the p_Z/E distribution in the region where the cut on p_Z/E is affected (see section 5.4). (c) indicates that p_Z/E distribution peaks at a higher value than the MC expectation. The disagreement is still observed in (d) near the threshold $p_Z/E = 0.95$ used in the selection. Since this can be a source of a systematic effect, two other criteria are tested for the systematic studies (1) only $E - p_Z > 12$ GeV is used and no p_Z/E cut is applied. (2) p_Z/E cut is changed from 0.95 to 0.90, where the agreement is better. This is discussed in section 8.3.

In all figures except (b), the distribution of the LUMI-tagged event has similar distribution to the normal dijet event. This fact confirms that the event is originated from the hard photoproduction process.

7.3 Properties of the jet observed in the detector

In this section several distributions related to the jet are presented.

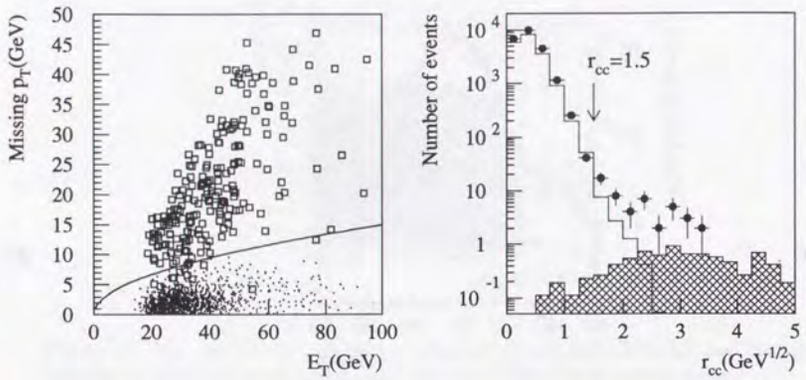

Figure 7.8: (a): The correlation between E_T and $\not{p}_T$. The dot denotes the dijet events from photoproduction (PYTHIA). The open square denotes the charged current MC. The curve is $r_{CC} = 1.5$. (b): The distribution of the r_{CC} of the data (dot), PYTHIA MC (solid histogram) and charged current event MC (shadowed histogram).

7.3.1 x_γ^{det} distribution

In calculating x_γ, the formula

$$x_\gamma^{det} = \frac{E_{T1}^{det} e^{-\eta_1^{det}} + E_{T2}^{det} e^{-\eta_2^{det}}}{(E - p_Z)_{CAL}} \tag{7.5}$$

is used. The uncorrected transverse energy of the jet is used since the denominator in the formula, $E - p_Z$ is uncorrected. Figure 7.10 shows the correlation between x_γ^{det} and x_γ^{had}, which is calculated by the formula

$$x_\gamma^{had} = \frac{E_{T1}^{had} e^{-\eta_1^{had}} + E_{T2}^{had} e^{-\eta_2^{had}}}{2yE_e} \tag{7.6}$$

is shown. The detector effect like the energy loss is partly canceled between the denominator and numerator of the formula, thus the correlation of x_γ to x_γ^{had} is good. The reconstruction of x_γ^{had} by x_γ^{det} is within a several percent shift as shown figure 7.10(b).

The x_γ^{det} distribution of the six unique regions of (η_1, η_2) used in $d\sigma/dE_T d\eta_1 d\eta_2$ is shown in figure 7.11. The expectation from PYTHIA for direct process only and the

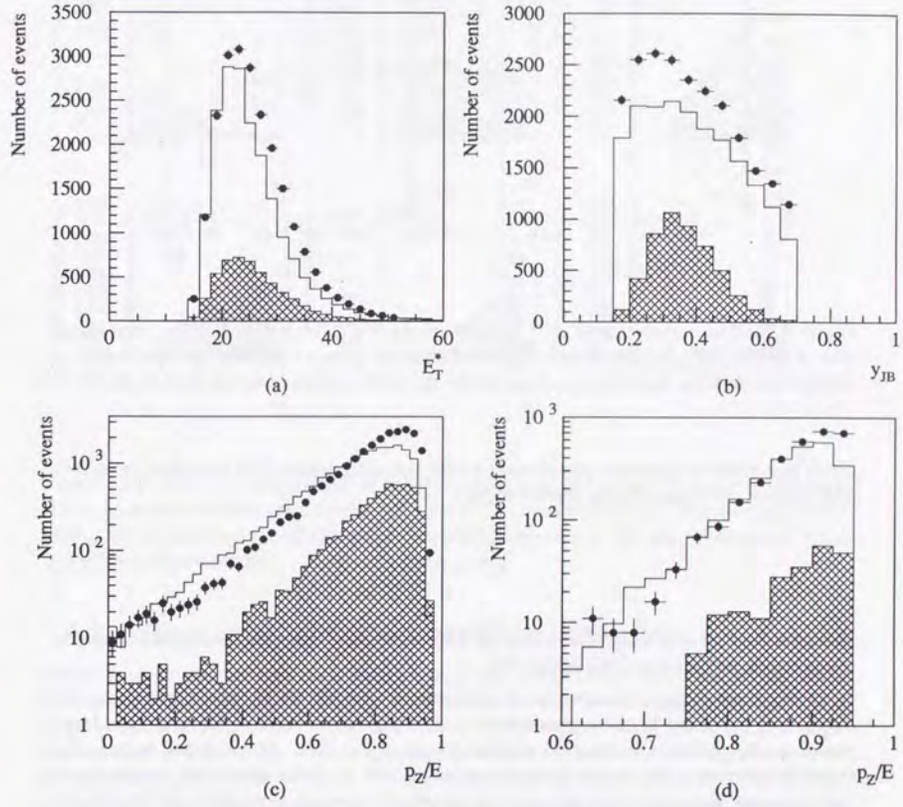

Figure 7.9: The global energy distribution of the dijet events: (a) E_T^* (in GeV) (b) y_{JB} (c) p_Z/E and (d) p_Z/E distribution in the range $8 < E - p_Z < 12$ GeV. The dot indicates the data with all the selection criteria, the solid histogram is MC(PYTHIA) with all the selection criteria The hatched histogram shows the LUMI subsample (the event that has an energy deposit in LUMI electron calorimeter of $5 < E_{LUMI} < 24.5$GeV) of the data.

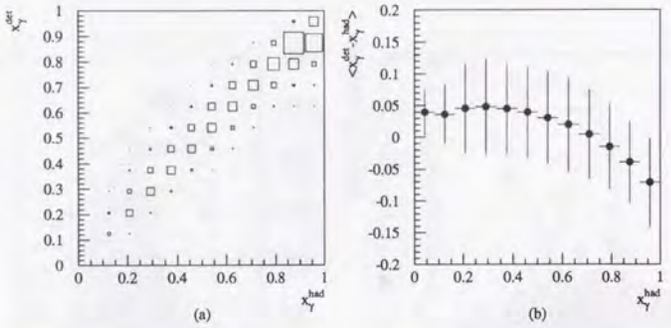

Figure 7.10: The correlation of x_γ^{had} and x_γ^{det} of the PYTHIA event. (a) The correlation plot of x_γ^{det} vs x_γ^{had}. (b) The profile $\langle x_\gamma^{det} - x_\gamma^{had} \rangle$ with respect to x_γ^{had}. The dijet events in which both detector level jets are matched to the hadron level ones are used in the plot.

direct plus resolved processes are also shown for the comparison. It is seen that the direct and resolved processes can be separated by

$$x_\gamma^{cut} = 0.75. \tag{7.7}$$

Hereafter this value is used to separate the two processes. This value is also taken also in the previous publication from ZEUS [28].

In this figure, some disagreements of the data with PYTHIA MC (light-shadowed histogram) are seen. In the region where both jets go forward ($1 < \eta_1, \eta_2 < 2$), a large excess is observed in the resolved process region, $x_\gamma < 0.75$. In the other region, the excess is observed in the direct process region, $x_\gamma > 0.75$. Since the excess on the direct region is seen in most of the kinematical region, an attempt is made to fit the MC to the data by changing the amount of the direct process. The fit is performed in the direct process region $x_\gamma > 0.75$ and the best fit to the data is multiplying the direct process by 1.34. The results are shown in the solid histogram in figure 7.11. Even after the fit, the agreement of the data and MC is not perfect. The similar fit is repeated by changing the resolved component only. In this case multiplying the resolved process by 1.23 results in the best fit (not shown). This increase of the direct or resolved events is taken into account in the cross section calculation as an estimation of the systematic uncertainty.

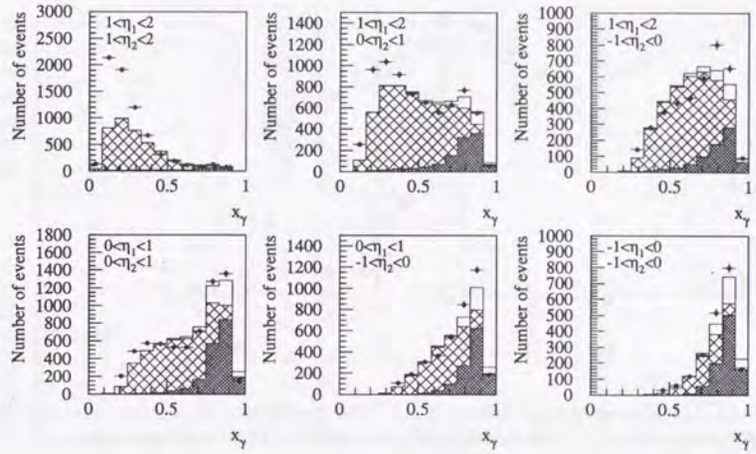

Figure 7.11: The x_γ^{det} distribution of the six unique bins of (η_1, η_2). The dot is the data, the light-shadowed histogram is the MC (PYTHIA) resolved+direct, the dark-shadowed histogram is direct only, and the solid unshaded histogram is MC resolved+direct fitted to the data (direct×1.34).

7.3.2 The azimuthal angle correlation of two jets

Since there are only two partons with an equal p_T in the lowest order scattering of the hard photoproduction, these two jets are observed as back-to-back jets in the plane that is perpendicular to the beam axis. Therefore for the dijet events, the azimuthal angle between two jets $\Delta\phi = |\phi_1 - \phi_2|$ is expected to be close to π. In the measurement of the inclusive dijet cross sections where the cross sections are inclusively defined, the two jets in the dijet events may not necessarily be well separated in azimuthal angle; there can be events with two jets in the same azimuthal angle and the different rapidity. Nevertheless it is worthwhile checking that the two jets are close to the back-to-back topology and well separated.

Figure 7.12 is the distribution of $\Delta\phi$ for the event of (a) the whole x_γ range and (b) $x_\gamma > 0.75$. The distribution peaks at π, which indicates that most of the events have a back-to-back topology. The distribution is narrower for the $x_\gamma > 0.75$ where the direct process is dominant. The distributions are reproduced by the PYTHIA model, though the

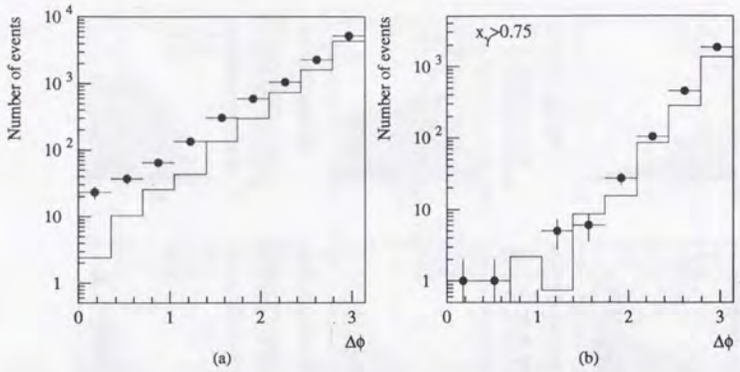

Figure 7.12: The azimuthal angle difference $\Delta\phi$ of the two highest E_T jets. (a) the event of entire x_γ range, (b) $x_\gamma > 0.75$ for the data (dot) and PYTHIA (solid histogram).

distribution is broader than the data in the entire x_γ region where the resolved process is dominant. This may come from the insufficient simulation of the transverse momentum of the photon remnant [60], or the imperfect simulation of the final state radiation(see also the next section).

7.3.3 The energy correlation between two jets

In the lowest order, there are only two jets with an equal P_T in an event. In the real event, however, the higher order effect produces many partons in the final state, thus the p_T of the leading and second highest p_T jet are not necessarily very close. Though the inclusive dijet cross section is safely defined in any order of the calculation by using E_{T_1} as E_T and exchanging the first and second jets, it is important to see the imbalance of the two highest E_T jets. Since the second jet is selected by the criteria $E_{T2}^{cor} > 8$ GeV, the spectrum of the second jet can change the cross section.

Figure 7.13 shows the distribution of $\Delta E_T = E_{T_1} - E_{T_2}$. The maximum allowed value of ΔE_T is restricted by the cut $E_{T_2} > 8$ GeV and depends on E_{T_1}. Therefore the events are shown classified by E_{T_1}. Due to the finite E_{T1} band, the maximum value of ΔE_T for each event varies within the indicated arrow for each figure. The distribution of ΔE_T in this range falls rapidly to zero. Except this region, it is seen that for the higher E_T region like $14 < E_T < 17$ GeV, the distribution of ΔE_T is relatively flat. This indicates that there

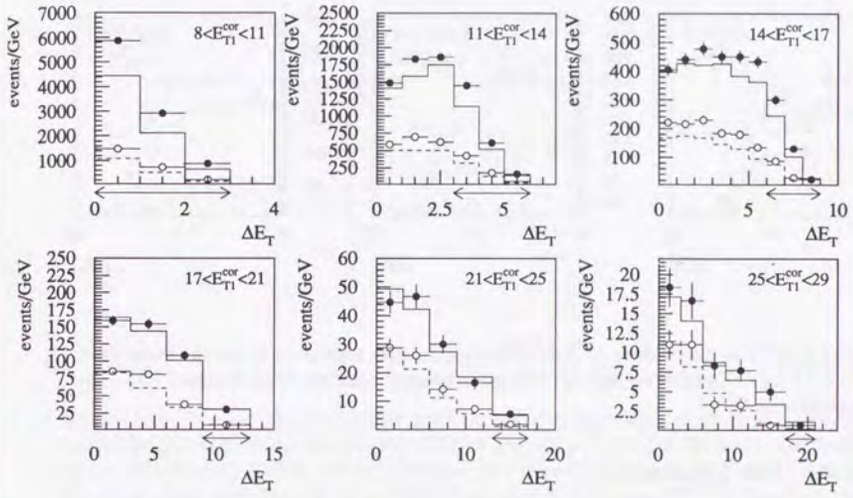

Figure 7.13: The distribution of the ΔE_T classified by E_{T_1}. The solid circle(histogram) shows the event of data(PYTHIA) from the entire x_γ range. The open circle(dashed histogram) shows the event of the data(PYTHIA) with $x_\gamma > 0.75$. The arrow below the holizontal axis in each histogram shows the region of the maximum allowed ΔE_T (see text). The E_T scale is in GeV.

are hard radiations from the partons of the $2 \to 2$ scattering. The fair agreement with MC indicates that the lowest order matrix element with the parton shower can reproduce the hard radiation quite well, except that there are excesses on the events with $x_\gamma > 0.75$ due to the event excess seen in figure 7.11.

The η dependence of the ΔE_T is shown in figure 7.14 in three regions of η_1 in the interval $14 < E_T < 17$(GeV). Apart from the low cross section prediction of PYTHIA, the shape is nearly reproduced by PYTHIA in each region of η_1.

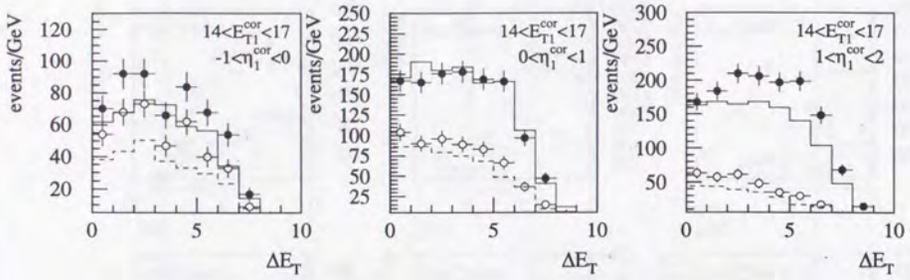

Figure 7.14: The distribution of ΔE_T classified in three regions of η_1 for the event $14 < E_T^{cor} < 17$ GeV. The symbol and the histogram definition are the same as figure 7.13. The E_T scale is in GeV.

7.3.4 The jet rate

The jet rate is another way to confirm how well the parton shower in the lowest order MC reproduces the higher order effect. Figure 7.15 shows the detector level jet rate of the selected events. Here the minimum E_T^{cor} requirement is reduced to 6 GeV and the $-1 < \eta < 2$ is imposed for the $n-$th jets of $n \geq 3$. The solid circle and histogram indicate the whole events, and the open circle and dashed line indicate the events with $x_\gamma^{det} > 0.75$. The ratio of the second and third jet, summarized in the table 7.1, agrees with the PYTHIA MC prediction, though the absolute jet rate is smaller due to the low cross section of the MC. The four jet event ratio, however, is underestimated by the PYTHIA MC.

Figure 7.16 shows the rapidity and E_T^{cor} distribution of the third and fourth jet. Though the absolute cross section is underestimated specially in the fourth jet case, the shape of both rapidity and E_T^{cor} is reasonably reproduced by the MC up to the fourth jet. It is concluded that the event topology of the third jet and the ratio of the two to three jet events are reproduced by the parton shower model.

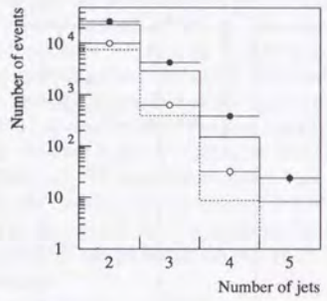

Figure 7.15: The jet rate of the dijet event. In selecting the three or more jet event, the minimum E_T^{cor} requirement is reduced to 6 GeV and the $-1 < \eta < 2$ cut is imposed for the $n-$th jet where $n \geq 3$. The solid circle(data) and the solid histogram(PYTHIA) indicate the whole event and the open circle(DATA) and dashed histogram(PYTHIA) indicate the event with $x_\gamma^{det} > 0.75$.

	ratio	3/2 jet	4/2 jet	5/2 jet
all events	data	0.11	9.3×10^{-2}	7.3×10^{-3}
	PYTHIA	0.10	4.4×10^{-2}	1.5×10^{-3}
$x_\gamma^{det} > 0.75$	data	0.049	2.4×10^{-2}	–
	PYTHIA	0.044	8.4×10^{-3}	–

Table 7.1: The jet rate of the photoproduction event. In selecting the three or more jet event, the minimum E_T^{cor} requirement is reduced to 6 GeV and the $-1 < \eta < 2$ is imposed for the $n-$th jet where $n \geq 3$.

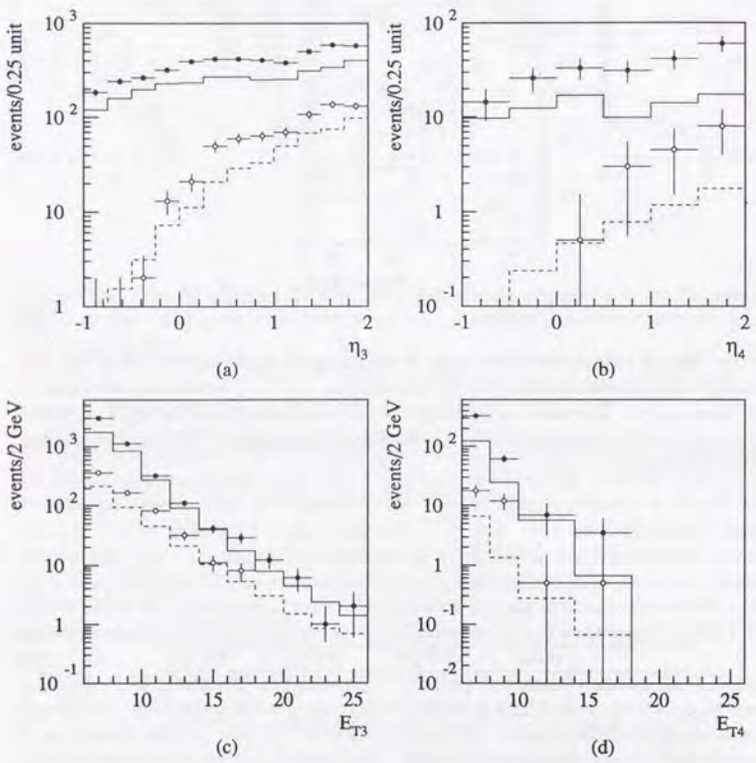

Figure 7.16: rapidity and the E_T distribution of the third and fourth jet. (a), (c): third jet and (b), (d): fourth jet. The definition of the symbols and histograms are the same as figure 7.15.

7.3.5 Transverse energy flow around the jet

Figure 7.17 shows the transverse energy flow around the jet per rapidity, as a function of $\Delta\eta = \eta^{CAL} - \eta_1^{det}$, where η_1^{det} is the rapidity of the first jet and η^{CAL} is the rapidity of the calorimeter cell. Only the cell of azimuthal angle difference $|\Delta\phi| = |\phi^{CAL} - \phi_1^{det}| < 1$ is used. In this figure the jets are selected from (a): $8 < E_T^{cor} < 11$(GeV) and $1 < \eta_1 < 2$ and (b): $8 < E_T^{cor} < 11$(GeV) and $-1 < \eta_1 < 0$. The events are further classified by the rapidity of the second (opposite) jet; $1 < \eta_2 < 2$, $0 < \eta_2 < 1$ and $-1 < \eta_2 < 0$. The rapidity of the first and second jet are exchanged and double counted as usual. It is seen that the MC (PYTHIA) prediction of the transverse energy flow of the jet pedestal of the proton direction ($\Delta\eta > 1$) is smaller than the real data in any kinematical regions of η. The excess observed in the case where the jet goes forward (a) is larger than backward (b). Further, in the figure (a), the transverse energy flow is larger if the second jet is in forward, whereas in the MC prediction the dependence of the transverse energy flow on the second jet rapidity is very little. In case both jets go into the rapidity of $1 < \eta < 2$, the energy flow per rapidity of the pedestal reaches up to 2 GeV. This is almost twice as much as the MC prediction.

As mentioned in section 4.4, the multiple interaction model increases the jet energy pedestal due to the low-p_T semi-hard scatterings in an event. Figure 7.18 shows the comparison of the transverse energy flow of the data and the HERWIG MI model with PYTHIA. The jet with $1 < \eta_1 < 2$ is shown since the jet pedestal excess is the largest in this region. Three histograms classified by the second jet rapidity are shown as in the previous figure. Though the data still shows much larger flow, there is an increase of the transverse energy flow in the pedestal of the jet from PYTHIA to HERWIG MI. The MI model shows improvements in describing the energy flow over the non-MI model.

To see the dependence of the jet energy pedestal on E_T and the rapidity of the jet, the amount of the jet transverse energy pedestal (jet E_T pedestal) is estimated by the transverse energy found in the jet pedestal region, defined as the sum of the transverse energy per unit rapidity and azimuthal angle inside the region $|\Delta\phi| = |\phi^{CAL} - \phi_1^{det}| < 1$ and $1 < |\Delta\eta| < 2$, where $\Delta\eta = \eta^{CAL} - \eta_1^{det}$. The region is indicated in figure 7.19.

Figure 7.20 shows the dependence of the jet E_T pedestal on the second jet rapidity for the three regions of the first jet. The jet with $8 < E_T^{cor} < 11$ GeV is chosen. The data are compared with the PYTHIA model (lines). In the whole x_γ region, it is observed that a large excess over PYTHIA model is seen in $\eta_1 > 0$ as in figure 7.17. The pedestal depends on the second jet rapidity in $\eta_1 > 0$, as observed in figure 7.17. The pedestal of the backward jet ($-1 < \eta_1 < 0$) is described in the model. On the other hand, the pedestal for the event with $x_\gamma > 0.75$ is well reproduced by PYTHIA. From this, it is concluded that the pedestal is simulated by the PYTHIA model for the direct process, though higher pedestal energy is observed than PYTHIA for the forward going jet in the entire x_γ region where the resolved process is dominant.

Figure 7.21 shows the comparison of the pedestal with three models: PYTHIA, HERWIG and HERWIG with multiple interaction option. These plots are shown for the whole x_γ region and for $x_\gamma > 0.75$. The pedestal is presented as a dependence on the

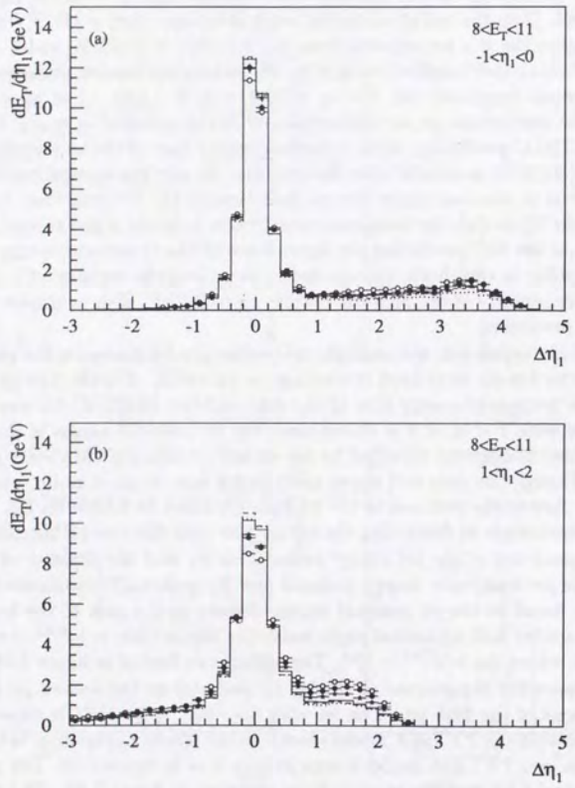

Figure 7.17: The transverse energy flow around the jet in two kinematical regions: (a): $8 < E_T^{cor} < 11$ GeV and $1 < \eta_1 < 2$ and (b): $8 < E_T^{cor} < 11$ GeV and $-1 < \eta_1 < 0$. The open circle (data) and the solid histogram (PYTHIA) shows the event with $1 < \eta_2 < 2$. The solid circle (data) and the dashed histogram (PYTHIA) shows the event with $0 < \eta_2 < 1$. The star symbol (data) and the dotted histogram (PYTHIA) shows the event with $-1 < \eta_2 < 0$.

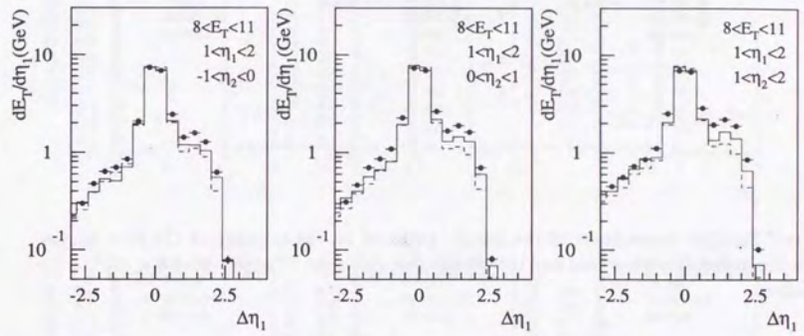

Figure 7.18: The transverse energy flow around the jet in comparison with the two models. The dot is thte data, the dashed histogram is PYTHIA, and the solid line is HERWIG with multiple interaction option. The jet with $1 < \eta_1 < 2$ is shown and classified by the rapidity of the second jet (from left to right, $-1 < \eta_2 < 0$, $0 < \eta_2 < 1$ and $1 < \eta_2 < 2$).

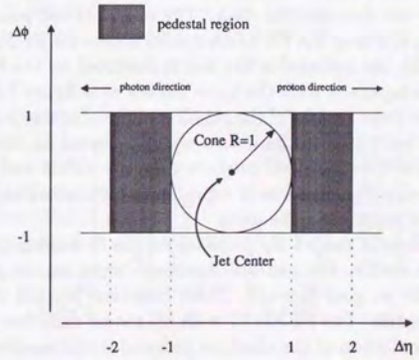

Figure 7.19: The jet energy pedestal region defined in $\Delta\eta - \Delta\phi$ plane (shaded area).

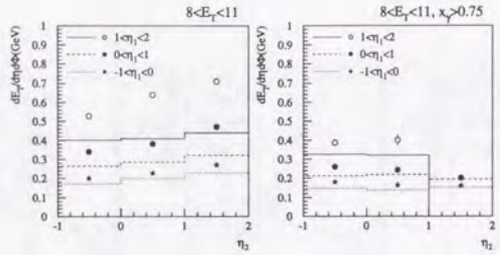

Figure 7.20: The dependence of the jet E_T pedestal on the rapidity of the first jet (to which the pedestal is observed) and the second (opposite) jet. The jets with $8 < E_T^{cor} < 11$ are taken.

second jet rapidity as in figure 7.20. In the entire x_γ region, the pedestal of HERWIG with MI is larger than PYTHIA or HERWIG for the jet with $0 < \eta_1 < 2$, though the pedestal is still smaller than the data. The dependence on the second jet is reproduced qualitatively by HERWIG with MI. In the other rapidity regions of the jet and for the event with $x_\gamma > 0.75$, the three models show similar pedestals and agree with the data.

Figure 7.22 shows the jet E_T pedestal as a function of the jet E_T. Here the jets with $1 < \eta_1 < 2$ and $0 < \eta_1 < 1$ are plotted. It is seen that there is a strong increase of the pedestal as jet E_T becomes smaller for the jet in $0 < \eta_1 < 2$, with the opposite jet also in forward ($1 < \eta_2 < 2$). The PYTHIA model shows the constant pedestal in any rapidity region of the jet and does not describe the data. The excess of the pedestal for the jet with $1 < \eta_1 < 2$ and $0 < \eta_2 < 2$ over the PYTHIA model is seen for jet E_T up to 21 GeV. For the event with $x_\gamma > 0.75$, the pedestal is flat and is described by the PYTHIA model.

Figure 7.23 shows the comparison with the three models as in figure 7.21. The jet with $1 < \eta_1 < 2$ is plotted for the three regions of the rapidity of the opposite jet. The PYTHIA and HERWIG model does not describe the excess of the pedestal for the jet $0 < \eta_2 < 2$ as seen in figure 7.21. HERWIG with MI predicts more pedestals and the increase of the pedestal toward the lower E_T direction is reproduced. The absolute amount of the pedestal energy, however, is lower than the data.

In summary, a large excess of the jet E_T pedestal for the forward-going jet ($0 < \eta_1 < 2$) is observed. For these events, the pedestal becomes larger as the jet E_T becomes smaller, and as the opposite jet goes forward. These behaviors are not described by the PYTHIA and HERWIG models. The HERWIG with MI model describes these behaviors qualitatively, though the prediction of the absolute pedestal is still smaller than the data. The pedestal for the event with $x_\gamma > 0.75$ agrees with the three models.

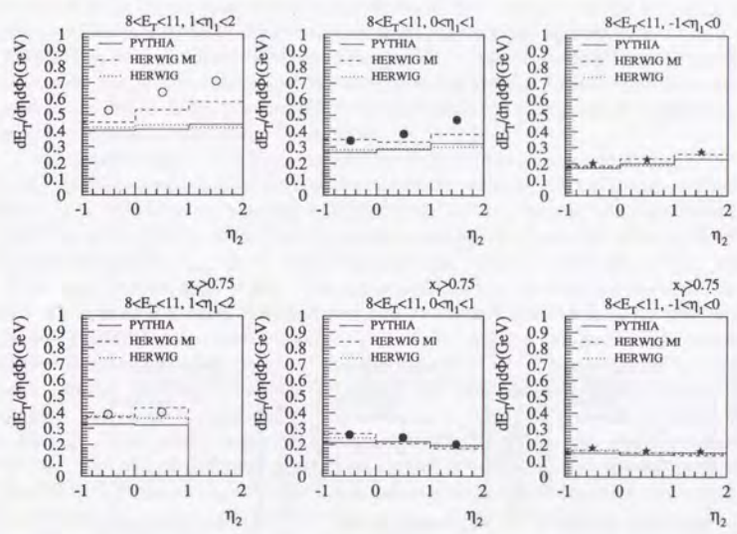

Figure 7.21: The jet E_T pedestal dependence on the rapidity of the first and second jet in comparison with the models.

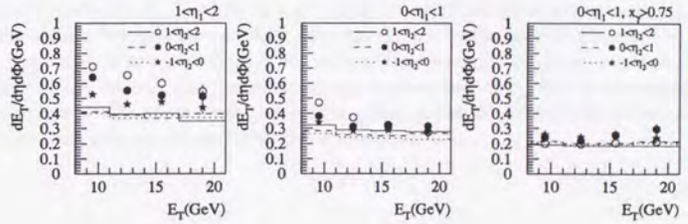

Figure 7.22: The dependence of the jet E_T pedestal on the jet E_T. The events with $1 < \eta_1 < 2$, $0 < \eta_1 < 1$ and $0 < \eta_1 < 1 (x_\gamma > 0.75)$ are shown.

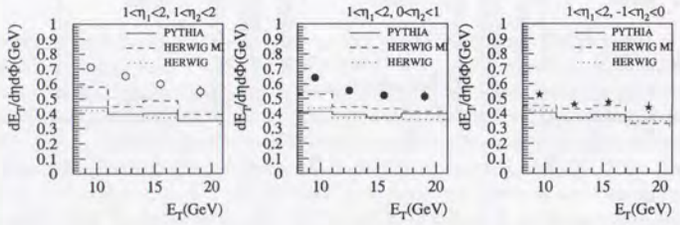

Figure 7.23: The dependence of the jet E_T pedestal on the jet E_T in comparison with the models.

7.4 The contribution of the diffractive event

As reported in the previous publications of the HERA experiments [50, 51], such a diffractive process is observed by the events that has a rapidity gap with no activity in the proton direction from the hadronic activity. Since a diffractively dissociated proton has a smaller mass than the proton remnant of the normal event, some of these events have no activity around the FCAL beam pipe region, hence one observes a large rapidity gap from the jet to the calorimeter edge of the beam pipe.

The rapidity gap in the previous publications has been represented using the variable η_{max}, the maximum rapidity of a calorimeter cluster with significant energy, called condensate. It is defined as an adjacent energy deposit of the calorimeter cells above 100(200) MeV for EMC(HAC). Here total condensate energy of above 400 MeV is used for the maximum rapidity η_{max} of the hadronic activities. Figure 7.24(a) shows the distribution of the η_{max} for the dijet events. The large peak at $\eta_{max} \simeq 4$ shows the existence of the activity around the beam pipe from the proton remnant, which is fairly well reproduced by the PYTHIA MC (dotted line). There is, however, a tail toward the smaller η_{max} direction that cannot be described by the standard MC. The events in the tail have a large rapidity gap, hence indicate the presence of the colour singlet exchange. The large rapidity gap event is separated by the cut $\eta_{max} < 1.5$. There are 64 events in the data with $\eta_{max} < 1.5$, which cannot be explained by the PYTHIA MC, which predicts 20 ± 7 events. The rest of the large rapidity gap event distribution can be well reproduced by the POMPYT Monte Carlo. The total number of events from the hard diffractive process contribution is estimated from the event in $\eta_{max} < 1.5$ and found to be 5 ± 1 %.

Figure 7.24(b) is the x_γ distribution of all the events with at least two jets of $E_T^{cor} > 8$ GeV, together with the event with $\eta_{max} < 1.5$. The event with a large rapidity gap is concentrated on the high-x region. Figure 7.24(c) shows the E_T of the jet. The E_T of the large rapidity gap event falls exponentially to the positive E_T direction, with approximately the same slope as the normal event. The η_2 distributions, with (d)$0 < \eta_1 < 1$ and (e)$-1 < \eta_1 < 0$, indicate that the large rapidity gap event is concentrated on the backward region ($\eta_1 < 0$). This is a natural consequence that no condensate is required above the η_{max} of 1.5. In any distributions, the fraction of the large rapidity event is less than a few percent and does not concentrate in the specific kinematical region.

Note that it is reported that the energy flow around the jet is concentrated in the center of the jet and less pedestal energy is observed [51], due to the absence of the colour flow to the proton remnant. This might cause the systematic effect on the cross section measurement hence is discussed in section 8.3.

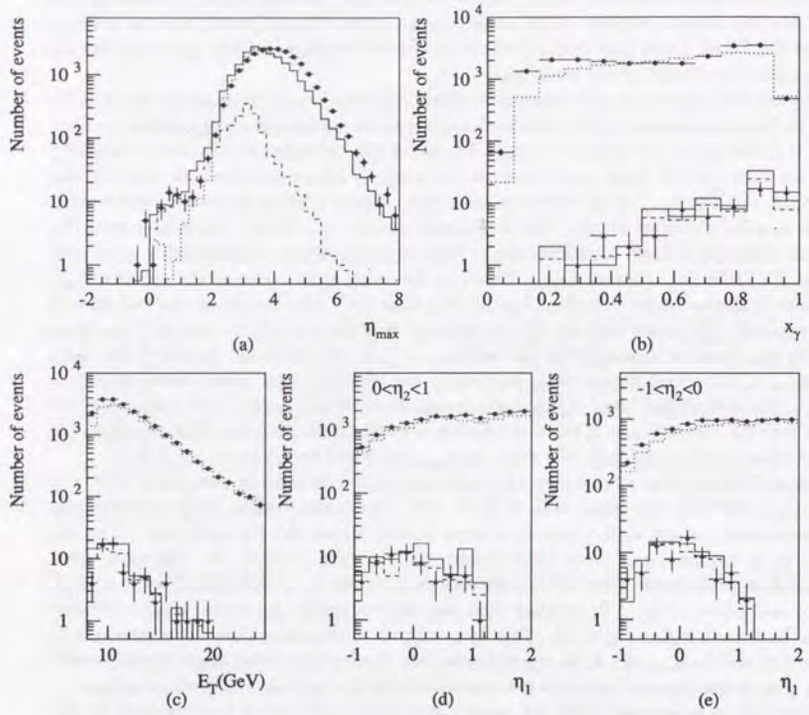

Figure 7.24: The distribution of the large rapidity gap events for the dijet events. (a): η_{max} (b): x_γ (c): $E_{T_{jet}}$ (d): η_1 of the events with $0 < \eta_2 < 1$ and (e): η_1 of the events with $-1 < \eta_2 < 0$. Solid circle(dotted histogram) shows all the data(PYTHIA) with at least two jets of $E_T^{cor} > 8$ GeV. The dashed(solid) histogram in (a) is the prediction of the POMPYT(POMPYT+PYTHIA). The triangle symbol in figure (b)–(e) shows the events with $\eta_{max} < 1.5$ of the data. The solid(dashed) histogram shows the MC expectation from PYTHIA+POMPYT(POMPYT only).

7.5 Check of the ZEUS detector simulation

7.5.1 y_{JB} reconstruction

For the events whose electron energy is measured by the LUMI electron calorimeter, the reconstruction of y by y_{JB} can be checked by the relation of $y_{LUMI} = (E_e - E_{LUMI})/E_e$ and y_{JB} where E_{LUMI} is the energy observed in the LUMI electron counter. y_{LUMI} is a good estimator of the true y since E_{LUMI} is measured as an electromagnetic shower thus the energy measurement is good. Therefore the shift of y_{JB} and the simulation of y_{JB} in MC can be checked by taking a difference between y_{LUMI} and y_{JB}.

Figure 7.25 is the y_{LUMI} dependence of (a) $\langle r \rangle = \langle (y_{LUMI} - y_{JB})/y_{LUMI} \rangle$ for the data and the PYTHIA MC, and (b) $\langle r \rangle_{data} - \langle r \rangle_{MC}$, which shows the difference in the y_{JB} reconstruction between the data and the MC. The dot shows the ratio for the events in entire x_γ range, and the open circle shows those with $x_\gamma > 0.75$. A large discrepancy ($\sim$ 7%) between data and MC is seen in the reconstruction of y_{JB}. This is not improved for the events with $x_\gamma > 0.75$.

In reconstructing the $y_{JB} = (E - p_Z)/2E_e$, part of the $E - p_Z$ comes from the $E - p_Z$ of jets. The x_γ formula(see formula 7.5 in section 7.3) can be rewritten as

$$x_\gamma^{det} = \frac{E_{T1}^{det} e^{-\eta_1^{det}} + E_{T2}^{det} e^{-\eta_2^{det}}}{(E - p_Z)_{CAL}} = \frac{\sum_{jet1,jet2}(E - p_Z)_{jet}}{(E - p_Z)_{CAL}}.$$

Therefore the fraction x_γ of the $E - p_Z$ is measured by the jets. In case x_γ^{det} is not large, the rest of $E - p_Z$ is mainly from the photon remnant. One possibility of the shift is due to the bad simulation of the energy measurement of RCAL around the beam pipe, hence a shift occurs in the energy measurement of the photon remnant. In this case, however, the shift in y_{JB} depends on the photon remnant energy, hence x_γ^{det}. Therefore the shift due to the energy scale of the entire calorimeter is also suspected.

For this reason, the systematic uncertainty of the shift in y_{JB} is studied as follows.

1. For the events with $x_\gamma > 0.75$, the effect of the y_{JB} shift is estimated by reducing the energy scale by 5%, and y_{JB} scale itself on the MC by 7%. This means more than half (> 3.8 %) of the y_{JB} shift is from the energy scale.

2. For the events for entire x_γ range, a conservative way is taken: only y_{JB} scale in the MC is reduced by 7% .

The result of this study is discussed in section 8.3.

7.5.2 Check of the calorimeter response of the jet

The jet energy correction and the correction factor estimation in the calculation of the cross section are based on the Monte Carlo simulation. Especially the incorrect absolute scale of the calorimeter response may lead to the systematic shift of the cross section. Here the energy scale shift of the detector simulation is checked using the jet by the following two methods.

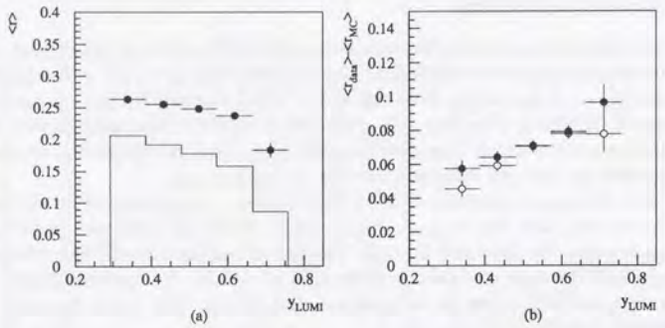

Figure 7.25: Comparison of y_{JB} and y_{LUMI}. (a) shows the profile $\langle r \rangle = \langle (y_{LUMI} - y_{JB})/y_{LUMI} \rangle$ for data (dot) and PYTHIA MC(histogram). (b) shows the difference between the data and MC, $\langle r \rangle_{data} - \langle r \rangle_{MC}$. The dijet events with the energy in LUMI counter are used for the plot.

Comparison with CTD response

Since the tracking detector can measure the absolute momentum of the charged track very precisely, the comparison of the CAL response with the CTD is a good way to check the absolute energy scale of the CAL. Here the jet energy is compared E_T^{CTD}, the transverse energy measured by CTD. E_T^{CTD} is defined as the sum of the transverse momentum of the charged track p_{Ttrack} which pointed the CAL within the cone of $R = 1$ around the jet. The tracks with $-1.5 < \eta_{track} < 1.5$ are used since the momentum measurement is reliable in this region. Corresponding to this region, only the jet with $-1.0 < \eta_{jet} < 1.0$ in the dijet sample ($E_T^{cor} > 8$ GeV) is considered in this study. The track with $p_{Ttrack} > 300$ MeV is considered to exclude the curled track.

Figure 7.26 shows the quantities of the selected tracks. (a) shows the distribution of E_T^{CTD}. In (b), the distribution of the p_{Ttrack} is plotted. These spectrums, ranging in more than three order of magnitude, are described by PYTHIA well. (c) shows the charged multiplicity inside the jet. The distribution is fairly reproduced by the PYTHIA model though the data shows slightly larger multiplicity. The average multiplicity is 4.8 for the data and 4.6 for PYTHIA. From this, it is concluded that the momentum and multiplicity of the changed particles inside the jet are well reproduced by the PYTHIA model.

The energy scale of the CAL is studied by taking the ratio E_T^{CTD}/E_T^{CAL} and comparing it with MC. The shift of the mean value of the ratio $r = \langle E_T^{CTD}/E_T^{CAL} \rangle$ indicates the possible shift of the calorimeter energy scale, since E_T^{CTD} is also expected to be the same

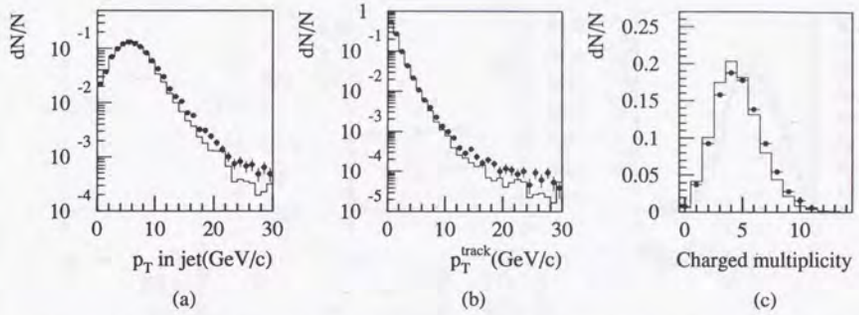

Figure 7.26: The distribution of the track inside the jet in $-1.5 < \eta_{track} < 1.5$ and $p_{Ttrack} > 300$ MeV. (a) E_T^{CTD}, (b) p_{Ttrack} and (c) the charged multiplicity of the jet for the data(dot) and PYTHIA(solid histogram).

between the MC and the data. The ratio of r_{data} to r_{MC},

$$\frac{r_{data}}{r_{MC}} = \left\langle \frac{E_T^{CTD}}{E_T^{CAL}} \right\rangle_{data} \Big/ \left\langle \frac{E_T^{CTD}}{E_T^{CAL}} \right\rangle_{MC} \simeq \left\langle \frac{E_{TMC}^{CAL}}{E_{Tdata}^{CAL}} \right\rangle,$$

indicates the ratio of the energy scale of the MC to the data. Figure 7.27 (a) shows the distribution of the E_T^{CTD}/E_T^{CAL}. The distribution of PYTHIA is shifted to lower value than the data. (b) shows the r_{data} (solid circle) and r_{MC} (open circle) by PYTHIA, in the four regions of η_{jet}. The mean of the r_{MC} is lower than the data in any rapidity region of the jet. (c) shows the ratio of the scale r_{data}/r_{MC}. This indicates that the energy scale in MC is about 5% larger than the data at maximum. The mean is 3.2 %. The dashed lines indicate the energy scale in MC by +7%, as suspected in the y_{JB} study (see the previous section) and −5%. The point stays within this range. From this study, the energy scale uncertainty is confirmed within $+7(-5)\%$ in the rapidity range $-1 < \eta_{jet} < 1$.

Jet E_T balance in dijet events

In dijet events of the lowest order, the E_T of two jets is expected to be balanced. Using this fact, the energy scale of the rapidity region in $1 < \eta_{jet} < 2$ can be checked by confirming that the jet E_T is balanced with the jet in $-1 < \eta_{jet} < 1$ where the energy scale of the calorimeter is known within $+7(-5)\%$. In reality the jet energy imbalance is not small in most of the events as demonstrated in section 7.3.3. In this study, the difference of

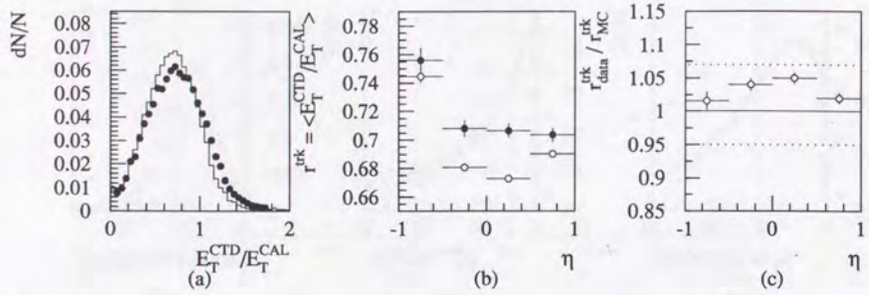

Figure 7.27: (a): the distribution of E_T^{CTD}/E_T^{CAL} for the data (dot) and PYTHIA (solid histogram). (b): $r = \langle E_T^{CTD}/E_T^{CAL} \rangle$ for the data (solid circle) and PYTHIA (open circle). (c) r_{data}/r_{MC}. The dashed lines show the energy scale uncertainties, +7(−5)%.

E_T of the two jets is defined as $\Delta = \langle (E_{Tf} - E_{Tc})/E_{Tc} \rangle$. Here E_{Tf} is the E_T of the jet in $1 < \eta_{jet} < 2$ (forward jet) and E_{Tc} is that of the jet in $-1 < \eta_{jet} < 1$ (central jet). In this case the difference is expected to be close to zero since the leading jet is evenly found in both regions. The deviation from zero, which mainly comes from the rapidity distribution of the leading jet, should be reproduced by MC. If Δ in MC is different from the data, there is a possibility that the E_T balance does not hold due to the energy scale in the forward region ($1 < \eta_{jet} < 2$).

Figure 7.28(a) shows the Δ of the four regions of the forward jet ($1 < \eta_{jet} < 2$). PYTHIA reproduced the distribution well. $\Delta_{MC} - \Delta_{data}$ indicates the energy scale shift of the MC assuming that the energy scale is equal in the central region. This is uncertain in about +3.2% in average. The maximum deviation of the MC from the data is estimated by adding the shift $\Delta_{MC} - \Delta_{data}$ and the uncertainty (3.2%) in quadrature. This is shown in (b) as a solid circle. The deviation stays within 5%.

From these two studies, the energy scale of the calorimeter is known in +7(-5)%. The effect of the uncertainty in calorimeter energy scale is estimated as a systematic uncertainty (see section 8.3).

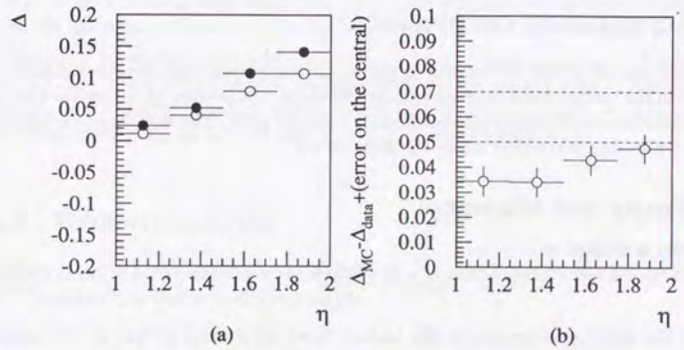

Figure 7.28: (a) $\Delta = \langle (E_{Tf} - E_{Tc})/E_{Tc} \rangle$, where E_{Tf} is the E_T of the jet in $1 < \eta_{jet} < 2$ (forward jet) and E_{Tc} is that of the jet in $-1 < \eta_{jet} < 1$ (central jet). The data (solid circle) and PYTHIA (open circle) are shown as a function of the rapidity of the forward jet. (b) $\Delta_{MC} - \Delta_{data}$ with the uncertainty of the central region (3.2%) added in quadrature. The two dashed lines indicate the 5% and 7% deviation, respectively.

Chapter 8

Dijet Cross Sections

8.1 Acceptance correction

As mentioned in section 6.2, the number of events measured from the detector information is corrected to the hadron level cross section by two steps: the jet energy correction and the acceptance correction. This section describes the second part. The acceptance correction is done by bin-by-bin correction using the formula 6.1 .

8.1.1 Purity and efficiency

The efficiency is defined as

$$E(I) = \frac{n^{det}(I)}{n(I)} \tag{8.1}$$

where $n(I)$ the number of events in the hadron level bin I, and $n^{det}(I)$ is the number of events that passed the detector level selection, and have two hadron level jets each of which has a matched jet on the detector level, in the hadron level bin I. The hadron level bins are defined as in figure 7.1 and 7.2. The matched jet of the detector level is searched in $E_T^{cor} > 8$ GeV and $-1 < \eta_{jet} < 2$. The efficiency represents which fraction of the event to be measured can be tagged in the experiment. High efficiency indicates less extrapolation to the unmeasured region by the experiment.

The purity is defined as

$$P(J) = \frac{n^{had}(J)}{n(J)} \tag{8.2}$$

where $n(J)$ the number of events in the detector level bin J, and $n^{had}(J)$ is the number of events that is in the hadron level kinematical region and have two detector level jets each of which has a matched jet in the hadron level, in the detector level bin J. The detector level bin is the same as hadron level bin defined in figure 7.1 and 7.2. The matched jet of the detector level is searched in $E_T^{had} > 8$ GeV and $-1 < \eta_{had} < 2$. The purity represents which fraction of the events tagged by the experiment contains the event to be measured. High purity indicates small contamination from outside the measured region.

Figure 8.1 shows the efficiency of each bin of $d\sigma/dE_T d\eta_1 d\eta_2$. Only the six unique bins of (η_1, η_2) are shown. The low efficiency in the low E_T region is the consequence of the E_T threshold at 8 GeV in the selection of the dijet event. The low efficiency in the high E_T bins in most of the rapidity region is mainly due to the $y_{JB} < 0.7$ cut.

Figure 8.2 shows the purity of each bin of the $d\sigma/dE_T d\eta_1 d\eta_2$. The low purity in the low E_T region is the consequence of the low E_T threshold, as in the case of the efficiency. The drop of the purity in $x_\gamma > 0.75$ and $1 < \eta_1, \eta_2 < 2$ is from the kinematical restriction of $y > 0.2$.

Figure 8.3 shows the efficiency of each bin of the $(d\sigma/d\eta_2)|_{E_T > E_T^{thr}, \eta_1}$. For $E_T > 11$ GeV, the efficiency is around 50-60 % since the threshold of the second jet, 8 GeV, is close to the first jet threshold E_T^{thr}. As E_T^{thr} becomes higher, the efficiency becomes higher as well. The drop of the efficiency in the lowest and highest rapidity bins are the effect of the edge in the matching condition. The drop of the efficiency in the lower rapidity region seen in the histogram of $E_T > 17$ GeV is due to the kinematical restriction by $y_{JB} < 0.7$.

Figure 8.4 shows the purity of each bin of the $(d\sigma/d\eta_2)|_{E_T > E_T^{thr}, \eta_1}$. As seen in the figure 8.3, the effect of the second jet threshold can be clearly seen. The drop of the efficiency in the higher rapidity region in the histogram of $1 < \eta_1 < 2$ is due to the kinematical restriction by $y > 0.2$ and $x_\gamma > 0.75$ in the hadron level.

8.1.2 Correction factor

As shown in eq. 6.1, the hadron level cross section is calculated by the bin-by-bin correction. The correction factor is defined as

$$C(I) = \frac{n(I)}{n(J)}, \tag{8.3}$$

where the bin J on the detector level and bin I on the hadron level occupy the same area on the jet variables, E_T, η_1 and η_2. The correction factor is approximately equal to the purity divided by the efficiency, though they are not exactly the same due to the matching condition.

Figure 8.5 is the correction factor of the $d\sigma/dE_T d\eta_1 d\eta_2$. The correction factor stays around one, which shows that the correction of the jet energy is stable overall. The drop of the correction factor in the direct region ($x_\gamma > 0.75$) in the case where both jets go forward ($\eta_1 > 1$ and $\eta > 2$) is due to the lower boundary of y.

Figure 8.6 is the correction factor of the $(d\sigma/d\eta_2)|_{E_T > E_T^{thr}, \eta_1}$. As in the case of $d\sigma/dE_T d\eta_1 d\eta_2$, the correction factor stays around one. The rise of the correction factor in the low rapidity reflects the low acceptance on the corner by $y_{JB} < 0.7$ and the $y < 0.85$ cut. The correction factors on these points change if one changes the y_{JB} cut from 0.7. The effect of this cut is studied as a systematic uncertainty in section 8.3.

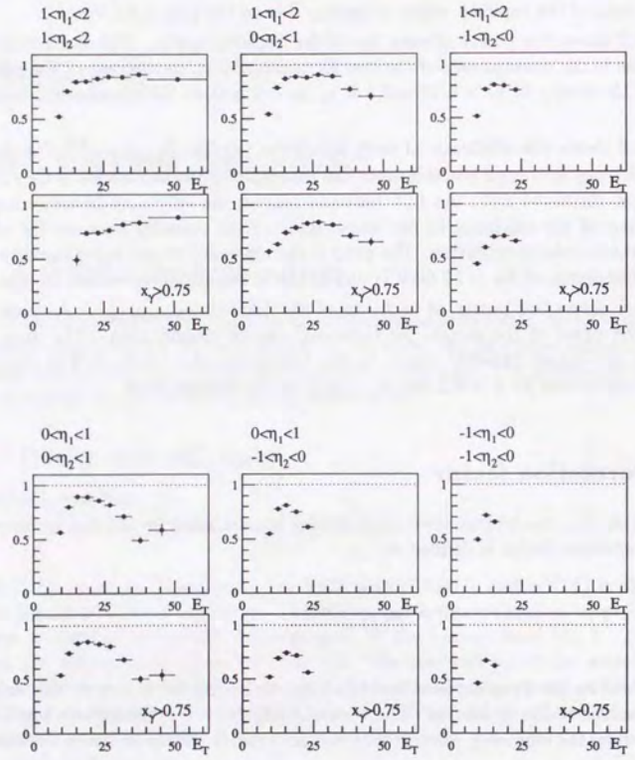

Figure 8.1: The efficiency of the measurement of $d\sigma/dE_T d\eta_1 d\eta_2$. Only six unique regions of (η_1, η_2) are shown and the efficiency is plotted with respect to E_T (in GeV). The upper histograms in each row show the efficiency for the entire range of x_γ, while the lower histogram shows the efficiency for the event with $x_\gamma > 0.75$. The number is estimated by PYTHIA.

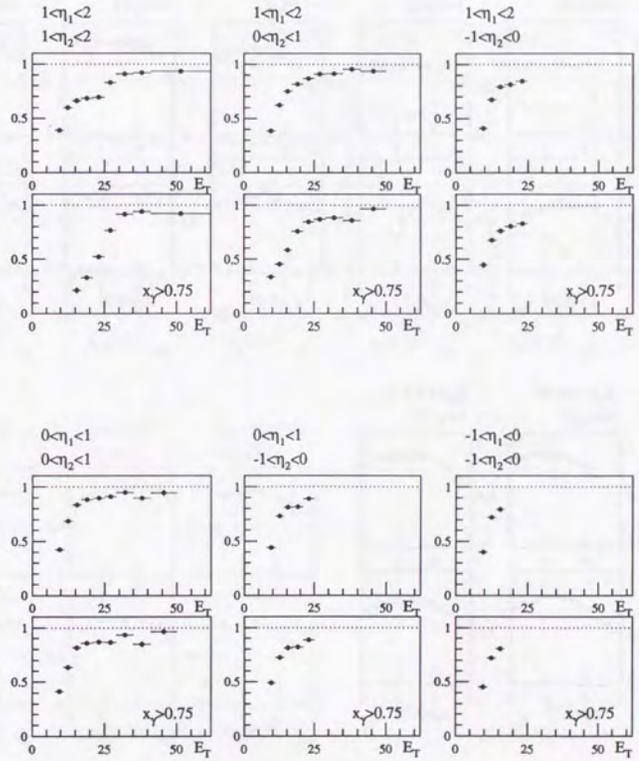

Figure 8.2: The purity of the measurement of $d\sigma/dE_T d\eta_1 d\eta_2$. The order of the histogram is the same as figure 8.1.

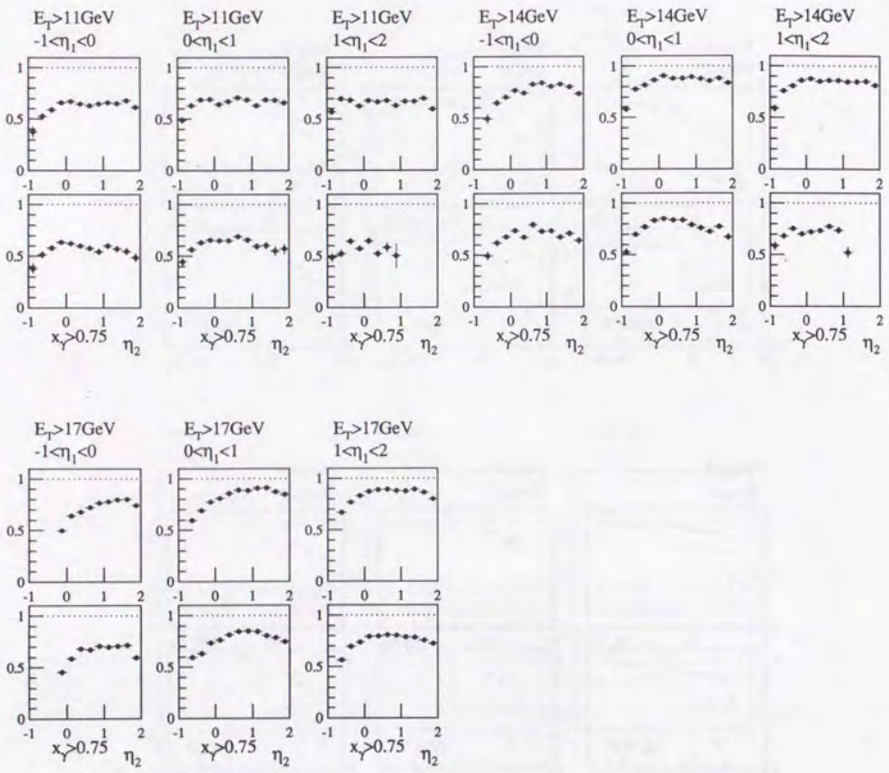

Figure 8.3: The efficiency of the measurement of $(d\sigma/d\eta_2)|_{E_T>E_T^{thr},\eta_1}$. The efficiencies are plotted with respect to η_2 for each of three threshold of E_T and the bins on the second jet rapidity. The upper histograms in each row show the efficiency for the entire range of x_γ, while the lower histogram shows the efficiency for the event with $x_\gamma > 0.75$. The number is estimated by PYTHIA.

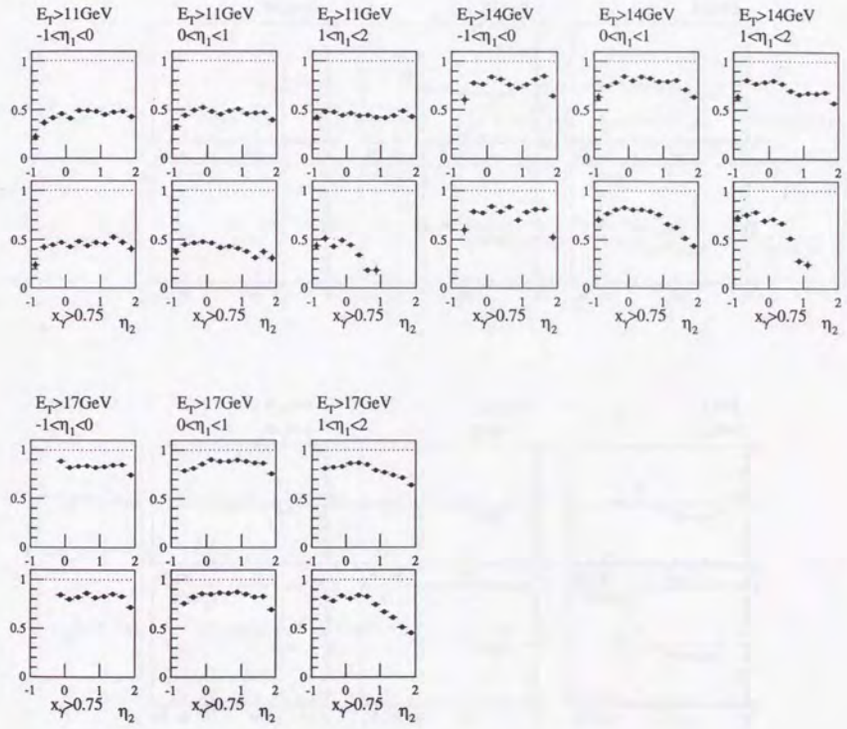

Figure 8.4: The purity of the measurement of $(d\sigma/d\eta_2)|_{E_T>E_T^{thr},\eta_1}$. The order of the histogram is the same as figure 8.3.

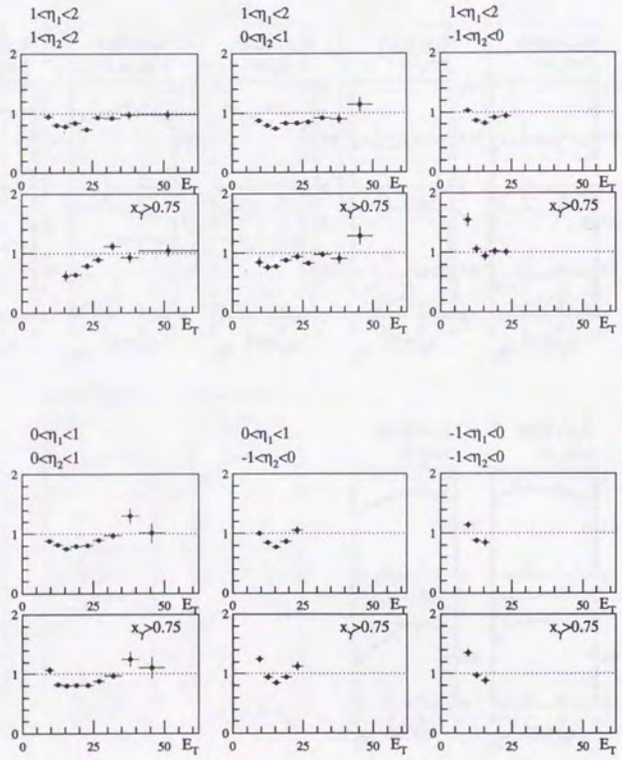

Figure 8.5: The correction factor of the measurement of $d\sigma/dE_T d\eta_1 d\eta_2$. The order of the histogram is the same as figure 8.1.

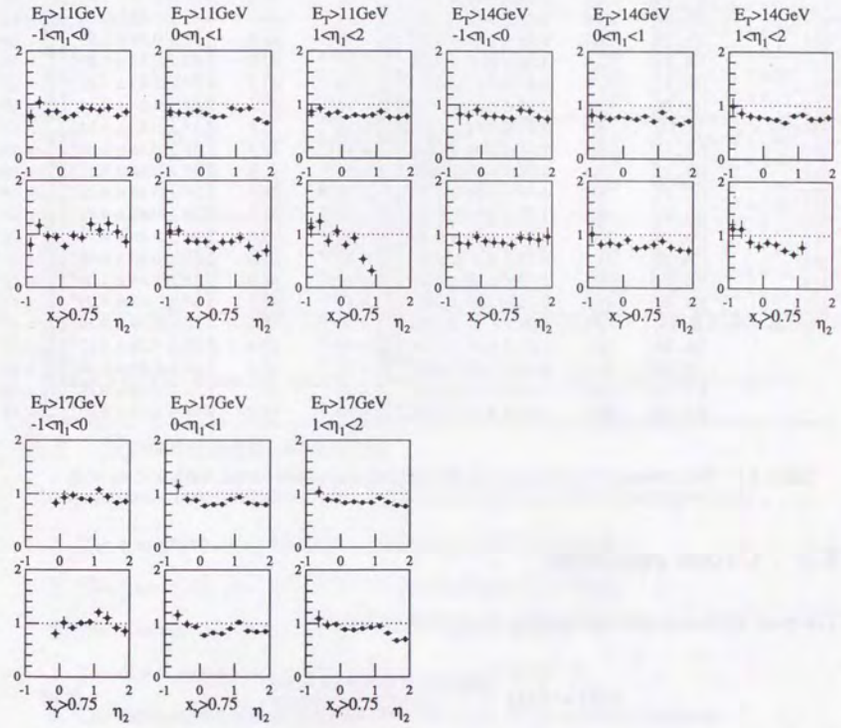

Figure 8.6: The correction factor of the measurement of $(d\sigma/d\eta_2)|_{E_T>E_T^{thr},\eta_1}$. The order of the histogram is the same as figure 8.3.

		entire x_γ range		$x_\gamma > 0.75$	
	E_T range	$\langle E_T \rangle$	$\sigma(\pm\text{stat.}\pm\text{syst.}\pm\text{Escale})$[nb/GeV]	$\langle E_T \rangle$	$\sigma(\pm\text{stat.}\pm\text{syst.}\pm\text{Escale})$[nb/GeV]
$1 < \eta_2 < 2$	[8, 11]	9.7	$3.59 \pm 0.16 \pm 0.55^{+0.93}_{-0.41} \times 10^{-1}$	–	–
	[11, 14]	12.4	$2.27 \pm 0.10 \pm 0.37^{+0.93}_{-0.40} \times 10^{-1}$	–	–
	[14, 17]	15.4	$8.79 \pm 0.43 \pm 1.40^{+4.26}_{-1.76} \times 10^{-2}$	15.6	$1.43 \pm 0.40 \pm 1.81^{+0.99}_{-0.26} \times 10^{-2}$
	[17, 21]	18.7	$3.56 \pm 0.19 \pm 0.43^{+1.98}_{-0.75} \times 10^{-2}$	19.1	$3.30 \pm 0.50 \pm 1.13^{+1.65}_{-0.41} \times 10^{-2}$
	[21, 25]	22.8	$1.21 \pm 0.10 \pm 0.07^{+0.81}_{-0.19} \times 10^{-2}$	22.9	$3.18 \pm 0.52 \pm 0.34^{+2.86}_{-0.37} \times 10^{-2}$
	[25, 29]	26.7	$9.37 \pm 0.97 \pm 1.32^{+5.52}_{-1.16} \times 10^{-3}$	26.8	$3.74 \pm 0.60 \pm 1.07^{+3.35}_{-0.16} \times 10^{-3}$
	[29, 35]	31.4	$2.56 \pm 0.40 \pm 0.22^{+1.37}_{-0.52} \times 10^{-3}$	31.6	$1.42 \pm 0.33 \pm 0.29^{+0.72}_{-0.28} \times 10^{-3}$
	[35, 41]	37.6	$1.11 \pm 0.27 \pm 0.29^{+0.45}_{-0.30} \times 10^{-3}$	37.7	$4.73 \pm 1.73 \pm 1.17^{+2.30}_{-1.17} \times 10^{-3}$
	[41, 62]	47.0	$2.13 \pm 0.54 \pm 0.76^{+0.67}_{-0.38} \times 10^{-4}$	47.1	$1.52 \pm 0.35 \pm 0.18^{+0.42}_{-0.25} \times 10^{-4}$
$0 < \eta_2 < 1$	[8, 11]	9.7	$3.17 \pm 0.13 \pm 0.41^{+0.79}_{-0.28} \times 10^{-1}$	9.9	$2.81 \pm 0.31 \pm 0.53^{+0.15}_{-0.23} \times 10^{-1}$
	[11, 14]	12.4	$2.31 \pm 0.09 \pm 0.12^{+0.78}_{-0.36} \times 10^{-1}$	12.5	$4.39 \pm 0.35 \pm 1.04^{+1.32}_{-0.35} \times 10^{-1}$
	[14, 17]	15.3	$1.02 \pm 0.04 \pm 0.08^{+0.42}_{-0.16} \times 10^{-1}$	15.4	$3.08 \pm 0.23 \pm 0.41^{+0.85}_{-0.40} \times 10^{-1}$
	[17, 21]	18.7	$4.10 \pm 0.20 \pm 0.20^{+1.47}_{-0.77} \times 10^{-2}$	18.8	$1.58 \pm 0.13 \pm 0.21^{+0.54}_{-0.20} \times 10^{-2}$
	[21, 25]	22.7	$1.32 \pm 0.11 \pm 0.11^{+0.52}_{-0.21} \times 10^{-2}$	22.8	$6.79 \pm 0.83 \pm 0.72^{+1.86}_{-0.89} \times 10^{-2}$
	[25, 29]	26.7	$6.55 \pm 0.76 \pm 0.48^{+2.69}_{-1.18} \times 10^{-3}$	26.8	$2.68 \pm 0.48 \pm 0.78^{+1.15}_{-0.45} \times 10^{-3}$
	[29, 35]	31.5	$2.73 \pm 0.42 \pm 0.52^{+0.92}_{-0.58} \times 10^{-3}$	31.5	$1.67 \pm 0.33 \pm 0.58^{+0.53}_{-0.32} \times 10^{-3}$
	[35, 41]	37.5	$1.20 \pm 0.28 \pm 0.22^{+0.51}_{-0.22} \times 10^{-3}$	37.6	$9.19 \pm 2.44 \pm 1.36^{+2.64}_{-1.77} \times 10^{-3}$
	[41, 50]	44.5	$4.35 \pm 1.52 \pm 2.61^{+1.20}_{-0.85} \times 10^{-4}$	44.5	$4.37 \pm 1.62 \pm 3.29^{+1.25}_{-0.85} \times 10^{-4}$
$-1 < \eta_2 < 0$	[8, 11]	9.7	$2.27 \pm 0.11 \pm 0.31^{+0.54}_{-0.30} \times 10^{-1}$	9.7	$1.11 \pm 0.09 \pm 0.16^{+0.09}_{-0.09} \times 10^{-1}$
	[11, 14]	12.4	$1.42 \pm 0.07 \pm 0.08^{+0.49}_{-0.29} \times 10^{-1}$	12.4	$7.33 \pm 0.55 \pm 1.17^{+1.92}_{-0.38} \times 10^{-1}$
	[14, 17]	15.3	$5.32 \pm 0.35 \pm 0.51^{+1.98}_{-1.15} \times 10^{-2}$	15.4	$3.00 \pm 0.28 \pm 0.28^{+0.85}_{-0.48} \times 10^{-2}$
	[17, 21]	18.6	$1.90 \pm 0.15 \pm 0.23^{+0.65}_{-0.35} \times 10^{-2}$	18.7	$1.24 \pm 0.13 \pm 0.21^{+0.35}_{-0.23} \times 10^{-2}$
	[21, 25]	22.6	$4.89 \pm 0.71 \pm 1.45^{+1.76}_{-1.09} \times 10^{-3}$	22.6	$3.44 \pm 0.62 \pm 0.72^{+1.42}_{-0.69} \times 10^{-3}$

Table 8.1: The measured cross section $d\sigma/dE_T d\eta_1 d\eta_2$ of the event with $1 < \eta_1 < 2$.

8.2 Cross sections

The cross section is calculated using the correction factor:

$$\sigma(I) = C(I) \cdot \frac{\text{number of event in bin } J}{\mathcal{L} \cdot (\text{bin area})}, \tag{8.4}$$

where $\mathcal{L} = 2.64\ \text{pb}^{-1}$ is the integrated luminosity of the data sample used in this analysis. The results of the $d\sigma/dE_T d\eta_1 d\eta_2$ are presented in figure 8.7 for the entire range of x_γ and 8.8 for the events with $x_\gamma > 0.75$. These results are listed in the tables 8.1, 8.2 and 8.3. In general, the cross section is described by the PYTHIA model.

The results of the $(d\sigma/d\eta_2)|_{E_T > E_T^{\text{thr}}, \eta_1}$ are presented in figure 8.9 for the entire range of x_γ and for the event with $x_\gamma > 0.75$. These results are also listed in the tables 8.4, 8.5 and 8.6.

		entire x_γ range		$x_\gamma > 0.75$	
	E_T range	$\langle E_T \rangle$	$\sigma(\pm\text{stat.}\pm\text{syst.}\pm\text{Escale})$[nb/GeV]	$\langle E_T \rangle$	$\sigma(\pm\text{stat.}\pm\text{syst.}\pm\text{Escale})$[nb/GeV]
$0 < \eta_2 < 1$	[8, 11]	9.7	$3.03 \pm 0.11 \pm 0.26^{+0.68}_{-0.36} \times 10^{-1}$	9.8	$1.17 \pm 0.07 \pm 0.14^{+0.23}_{-0.09} \times 10^{-1}$
	[11, 14]	12.3	$2.23 \pm 0.08 \pm 0.11^{+0.75}_{-0.38} \times 10^{-1}$	12.4	$1.04 \pm 0.06 \pm 0.15^{+0.30}_{-0.13} \times 10^{-1}$
	[14, 17]	15.3	$8.31 \pm 0.37 \pm 0.94^{+2.70}_{-1.33} \times 10^{-2}$	15.4	$4.96 \pm 0.31 \pm 0.92^{+1.69}_{-0.80} \times 10^{-2}$
	[17, 21]	18.7	$3.06 \pm 0.17 \pm 0.18^{+0.88}_{-0.44} \times 10^{-2}$	18.8	$1.81 \pm 0.13 \pm 0.19^{+0.43}_{-0.21} \times 10^{-2}$
	[21, 25]	22.7	$1.42 \pm 0.11 \pm 0.11^{+0.44}_{-0.25} \times 10^{-2}$	22.7	$1.05 \pm 0.10 \pm 0.18^{+0.26}_{-0.15} \times 10^{-2}$
	[25, 29]	26.8	$4.60 \pm 0.65 \pm 0.78^{+1.74}_{-0.88} \times 10^{-3}$	26.8	$3.18 \pm 0.53 \pm 0.63^{+1.13}_{-0.60} \times 10^{-3}$
	[29, 35]	31.3	$1.11 \pm 0.27 \pm 0.35^{+0.39}_{-0.18} \times 10^{-3}$	31.4	$7.35 \pm 2.16 \pm 2.94^{+2.44}_{-1.11} \times 10^{-3}$
	[35, 41]	37.7	$4.97 \pm 2.08 \pm 2.40^{+0.01}_{-0.67} \times 10^{-4}$	37.8	$4.76 \pm 2.00 \pm 1.45^{+0.12}_{-0.69} \times 10^{-4}$
	[41, 50]	43.6	$1.72 \pm 0.90 \pm 1.37^{+0.96}_{-0.38} \times 10^{-4}$	43.7	$1.87 \pm 0.99 \pm 0.90^{+1.01}_{-0.28} \times 10^{-4}$
$-1 < \eta_2 < 0$	[8, 11]	9.7	$2.20 \pm 0.10 \pm 0.12^{+0.54}_{-0.25} \times 10^{-1}$	9.7	$1.35 \pm 0.08 \pm 0.10^{+0.18}_{-0.09} \times 10^{-1}$
	[11, 14]	12.3	$1.33 \pm 0.06 \pm 0.15^{+0.39}_{-0.20} \times 10^{-1}$	12.3	$9.26 \pm 0.55 \pm 1.53^{+2.71}_{-1.59} \times 10^{-1}$
	[14, 17]	15.3	$5.10 \pm 0.32 \pm 0.61^{+1.33}_{-0.93} \times 10^{-2}$	15.3	$4.04 \pm 0.29 \pm 0.45^{+0.90}_{-0.50} \times 10^{-2}$
	[17, 21]	18.6	$1.57 \pm 0.14 \pm 0.32^{+0.60}_{-0.24} \times 10^{-2}$	18.6	$1.40 \pm 0.13 \pm 0.24^{+0.43}_{-0.22} \times 10^{-2}$
	[21, 25]	22.5	$4.72 \pm 0.74 \pm 1.93^{+1.76}_{-0.95} \times 10^{-3}$	22.5	$4.39 \pm 0.74 \pm 1.12^{+1.49}_{-0.94} \times 10^{-3}$

Table 8.2: The measured cross section $d\sigma/dE_T d\eta_1 d\eta_2$ of the event with $0 < \eta_1 < 1$.

8.3 Systematic studies

The systematic uncertainties of the analysis are studied for the following items.

1. The correction using HERWIG MC instead of PYTHIA.
2. The correction using HERWIG MI MC instead of PYTHIA.
3. The resolved component in PYTHIA is increased by 24 %.
4. The direct component in PYTHIA is increased by 40 %.
5. The diffractive event is included by 10% of the total number of events.
6. The cut $y_{JB} < 0.7$ is changed to $y_{JB} < 0.67$.
7. The cut $y_{JB} < 0.7$ is changed to $y_{JB} < 0.73$.
8. The lower $E - p_Z > 8$GeV cut is removed and only the cut $E - p_Z > 12$ GeV is used. The cut $p_Z/E < 0.95$ has no effect in this case.
9. The cut $p_Z/E < 0.95$ for the event of $8 < E - p_Z < 12$ GeV is changed to $p_Z/E < 0.90$.

		entire x_γ range		$x_\gamma > 0.75$	
	E_T range	$\langle E_T \rangle$	$\sigma(\pm\text{stat.}\pm\text{syst.}\pm\text{Escale})$[nb/GeV]	$\langle E_T \rangle$	$\sigma(\pm\text{stat.}\pm\text{syst.}\pm\text{Escale})$[nb/GeV]
$-1 < \eta_2 < 0$	[8, 11]	9.6	$1.49 \pm 0.08 \pm 0.15^{+0.46}_{-0.25} \times 10^{-1}$	9.6	$1.18 \pm 0.07 \pm 0.16^{+0.30}_{-0.16} \times 10^{-1}$
	[11, 14]	12.3	$7.60 \pm 0.47 \pm 1.35^{+2.19}_{-1.12} \times 10^{-2}$	12.3	$7.10 \pm 0.47 \pm 0.84^{+2.17}_{-1.01} \times 10^{-2}$
	[14, 17]	15.2	$1.99 \pm 0.21 \pm 0.74^{+0.39}_{-0.33} \times 10^{-2}$	15.2	$1.98 \pm 0.21 \pm 0.33^{+0.43}_{-0.24} \times 10^{-2}$

Table 8.3: The measured cross section $d\sigma/dE_T d\eta_1 d\eta_2$ of the event with $-1 < \eta_1 < 0$.

10. The cut $E_T^* > 8GeV$ is increased to 10 GeV.

11. The y_{JB} scale of the MC is decreased by 7 %. In $x_\gamma < 0.75$, the energy scale in the MC is decreased by 5 % at the same time.

12. The photon structure function of the PYTHIA is changed from GRV-LO to LAC1.

13. The proton structure function of the PYTHIA is changed from MRSD- to MRSD^0.

14. The energy correction curve is changed from the $\langle E_T^{det}/E_T^{had} \rangle$ profiling to the $\langle E_T^{had} - E_T^{det} \rangle$ one.

The HERWIG MC is used as an estimator of the possible model dependence of the parton shower and fragmentation. The HERWIG MI is used to check the energy flow dependence of the correction procedure. The possible effects from the ratio of the direct to resolved processes are estimated to change the ratio of these processes by increasing the direct and resolved components. The direct(resolved) components are increased by 40%(24%) as discussed in section 7.3.

In the calculation of the cross section, the contribution of the hard diffractive process is not subtracted from the data sample since this thesis intends to measure the dijet cross section of all the possible processes in the given kinematical region. In the calculation of the cross section only the non-diffractive MC have been used to estimate the jet energy correction and the bin-by-bin correction factor. Though the procedure to calculate the cross section is less influenced by the energy flow around the jet, the possible systematic effect is estimated by adding the POMPYT MC scaled as 10% of the total number of events in the dijet sample.

The correspondence of y and y_{JB} around $y_{JB} \sim 0.7$ is different between the event of the direct and resolved processes, as seen in figure 7.5. The possible systematic effect, especially on the measurement of the cross section of $x_\gamma > 0.75$, is studied by changing the upper limit of y_{JB} from 0.7 to 0.67 and 0.73.

		entire x_γ range		$x_\gamma > 0.75$	
	η_2 range	$\langle \eta_2 \rangle$	$\sigma(\pm\text{stat.}\pm\text{syst.}\pm\text{Escale})$[nb]	$\langle \eta_2 \rangle$	$\sigma(\pm\text{stat.}\pm\text{syst.}\pm\text{Escale})$[nb]
$1 < \eta_1 < 2$	[-1.00, -0.75]	-0.88	$2.50 \pm 0.35 \pm 0.52^{+1.12}_{-0.31} \times 10^{-1}$	-0.88	$1.71 \pm 0.32 \pm 0.37^{+0.58}_{-0.01} \times 10^{-1}$
	[-0.75, -0.50]	-0.62	$3.78 \pm 0.40 \pm 0.30^{+1.58}_{-0.54} \times 10^{-1}$	-0.62	$2.26 \pm 0.36 \pm 0.66^{+0.47}_{-0.16} \times 10^{-1}$
	[-0.50, -0.25]	-0.38	$4.61 \pm 0.42 \pm 0.37^{+1.26}_{-0.53} \times 10^{-1}$	-0.37	$1.99 \pm 0.28 \pm 0.40^{+0.54}_{-0.22} \times 10^{-1}$
	[-0.25, 0.00]	-0.12	$6.15 \pm 0.47 \pm 0.62^{+2.08}_{-1.00} \times 10^{-1}$	-0.12	$2.87 \pm 0.35 \pm 0.28^{+0.72}_{-0.07} \times 10^{-1}$
	[0.00, 0.25]	0.13	$6.74 \pm 0.48 \pm 0.77^{+2.22}_{-0.93} \times 10^{-1}$	0.13	$2.11 \pm 0.26 \pm 0.56^{+0.55}_{-0.20} \times 10^{-1}$
	[0.25, 0.50]	0.38	$7.85 \pm 0.57 \pm 0.27^{+2.44}_{-1.43} \times 10^{-1}$	0.38	$2.33 \pm 0.30 \pm 0.41^{+0.75}_{-0.16} \times 10^{-1}$
	[0.50, 0.75]	0.62	$7.14 \pm 0.53 \pm 0.63^{+2.27}_{-0.99} \times 10^{-1}$	0.61	$7.84 \pm 1.47 \pm 1.64^{+2.17}_{-0.24} \times 10^{-1}$
	[0.75, 1.00]	0.87	$5.99 \pm 0.49 \pm 0.89^{+2.50}_{-1.06} \times 10^{-1}$	0.83	$9.47 \pm 3.64 \pm 6.09^{+5.69}_{-1.55} \times 10^{-1}$
	[1.00, 1.25]	1.12	$6.40 \pm 0.57 \pm 1.30^{+3.13}_{-1.07} \times 10^{-1}$	–	–
	[1.25, 1.50]	1.38	$5.95 \pm 0.51 \pm 0.75^{+2.34}_{-0.97} \times 10^{-1}$	–	–
	[1.50, 1.75]	1.62	$6.81 \pm 0.58 \pm 1.23^{+3.01}_{-1.54} \times 10^{-1}$	–	–
	[1.75, 2.00]	1.87	$8.01 \pm 0.67 \pm 1.62^{+2.66}_{-1.19} \times 10^{-1}$	–	–
$0 < \eta_1 < 1$	[-1.00, -0.75]	-0.86	$2.31 \pm 0.30 \pm 0.57^{+0.87}_{-0.32} \times 10^{-1}$	-0.87	$2.11 \pm 0.31 \pm 0.39^{+0.68}_{-0.34} \times 10^{-1}$
	[-0.75, -0.50]	-0.63	$3.43 \pm 0.35 \pm 0.61^{+0.69}_{-0.49} \times 10^{-1}$	-0.63	$2.90 \pm 0.35 \pm 0.39^{+0.59}_{-0.55} \times 10^{-1}$
	[-0.50, -0.25]	-0.37	$4.49 \pm 0.39 \pm 0.69^{+1.71}_{-0.95} \times 10^{-1}$	-0.38	$2.96 \pm 0.32 \pm 0.65^{+1.21}_{-0.35} \times 10^{-1}$
	[-0.25, 0.00]	-0.12	$5.75 \pm 0.47 \pm 0.34^{+1.37}_{-0.99} \times 10^{-1}$	-0.13	$3.17 \pm 0.34 \pm 0.46^{+0.74}_{-0.69} \times 10^{-1}$
	[0.00, 0.25]	0.13	$6.21 \pm 0.48 \pm 0.43^{+2.09}_{-1.05} \times 10^{-1}$	0.12	$3.59 \pm 0.37 \pm 0.49^{+1.03}_{-0.49} \times 10^{-1}$
	[0.25, 0.50]	0.38	$6.04 \pm 0.45 \pm 0.47^{+1.96}_{-0.88} \times 10^{-1}$	0.38	$2.79 \pm 0.29 \pm 0.83^{+0.61}_{-0.16} \times 10^{-1}$
	[0.50, 0.75]	0.63	$6.47 \pm 0.47 \pm 0.53^{+2.69}_{-0.94} \times 10^{-1}$	0.63	$3.14 \pm 0.34 \pm 0.42^{+1.16}_{-0.38} \times 10^{-1}$
	[0.75, 1.00]	0.87	$8.19 \pm 0.59 \pm 0.76^{+2.22}_{-1.80} \times 10^{-1}$	0.87	$3.03 \pm 0.33 \pm 0.61^{+0.95}_{-0.59} \times 10^{-1}$
	[1.00, 1.25]	1.13	$6.64 \pm 0.50 \pm 0.31^{+2.51}_{-1.08} \times 10^{-1}$	1.12	$1.94 \pm 0.27 \pm 0.43^{+0.56}_{-0.12} \times 10^{-1}$
	[1.25, 1.50]	1.37	$8.16 \pm 0.60 \pm 0.93^{+2.11}_{-1.12} \times 10^{-1}$	1.36	$1.59 \pm 0.23 \pm 0.83^{+0.31}_{-0.06} \times 10^{-1}$
	[1.50, 1.75]	1.63	$6.67 \pm 0.49 \pm 0.55^{+2.18}_{-1.29} \times 10^{-1}$	1.62	$9.64 \pm 1.60 \pm 2.13^{+2.79}_{-1.68} \times 10^{-1}$
	[1.75, 2.00]	1.89	$6.36 \pm 0.49 \pm 0.86^{+2.46}_{-0.85} \times 10^{-1}$	1.88	$7.58 \pm 1.52 \pm 5.49^{+4.36}_{-0.24} \times 10^{-1}$
$-1 < \eta_1 < 0$	[-1.00, -0.75]	-0.85	$8.17 \pm 1.69 \pm 3.86^{+2.75}_{-0.42} \times 10^{-2}$	-0.85	$8.29 \pm 1.70 \pm 2.14^{+3.26}_{-0.90} \times 10^{-2}$
	[-0.75, -0.50]	-0.62	$2.45 \pm 0.33 \pm 0.81^{+0.43}_{-0.46} \times 10^{-1}$	-0.62	$2.35 \pm 0.33 \pm 0.39^{+0.51}_{-0.48} \times 10^{-1}$
	[-0.50, -0.25]	-0.38	$2.75 \pm 0.30 \pm 0.44^{+0.83}_{-0.61} \times 10^{-1}$	-0.38	$2.60 \pm 0.31 \pm 0.24^{+0.67}_{-0.43} \times 10^{-1}$
	[-0.25, 0.00]	-0.12	$3.20 \pm 0.32 \pm 0.38^{+1.02}_{-0.27} \times 10^{-1}$	-0.12	$2.81 \pm 0.31 \pm 0.49^{+1.05}_{-0.28} \times 10^{-1}$
	[0.00, 0.25]	0.12	$3.41 \pm 0.32 \pm 0.69^{+1.19}_{-0.54} \times 10^{-1}$	0.12	$2.49 \pm 0.27 \pm 0.96^{+0.97}_{-0.42} \times 10^{-1}$
	[0.25, 0.50]	0.37	$3.76 \pm 0.35 \pm 0.43^{+1.03}_{-0.95} \times 10^{-1}$	0.37	$3.04 \pm 0.34 \pm 0.27^{+0.47}_{-0.43} \times 10^{-1}$
	[0.50, 0.75]	0.62	$4.32 \pm 0.42 \pm 0.30^{+1.03}_{-0.66} \times 10^{-1}$	0.62	$2.63 \pm 0.33 \pm 0.42^{+0.83}_{-0.36} \times 10^{-1}$
	[0.75, 1.00]	0.87	$4.46 \pm 0.43 \pm 0.70^{+1.42}_{-0.78} \times 10^{-1}$	0.87	$3.10 \pm 0.40 \pm 0.31^{+1.02}_{-0.76} \times 10^{-1}$
	[1.00, 1.25]	1.13	$4.36 \pm 0.42 \pm 0.66^{+1.92}_{-0.47} \times 10^{-1}$	1.13	$2.40 \pm 0.34 \pm 0.70^{+0.68}_{-0.12} \times 10^{-1}$
	[1.25, 1.50]	1.37	$4.48 \pm 0.42 \pm 0.37^{+1.83}_{-0.63} \times 10^{-1}$	1.37	$2.69 \pm 0.37 \pm 0.47^{+0.78}_{-0.16} \times 10^{-1}$
	[1.50, 1.75]	1.62	$4.19 \pm 0.39 \pm 0.34^{+1.51}_{-0.73} \times 10^{-1}$	1.62	$2.38 \pm 0.35 \pm 0.34^{+0.65}_{-0.17} \times 10^{-1}$
	[1.75, 2.00]	1.88	$4.00 \pm 0.40 \pm 0.35^{+0.76}_{-0.50} \times 10^{-1}$	1.88	$1.37 \pm 0.24 \pm 0.46^{+0.25}_{-0.03} \times 10^{-1}$

Table 8.4: The measured cross section $(d\sigma/d\eta_2)|_{E_T > E_T^{thr}, \eta_1}$ of the event with $E_T > 11$GeV.

As shown in figure 7.9, the MC expectation of the distribution of the p_Z/E does not agree with the data. This effect is studied by the two variations of the selection criteria. One is not to use p_Z/E cut shown in figure 5.2: only the event with $E - p_Z > 12$ GeV is used. The other way is to change the p_Z/E threshold from 0.95 to 0.90, below which the agreement of the distributions is better.

The decrease of the y_{JB} scale is taken for a systematic study as discussed in section 7.5.1.

The effect of the change of the photon or proton structure function is estimated by changing the photon structure function from GRV-LO to LAC1 and the proton structure function from MRSA to MRSD$'_0$. In changing the photon or proton structure function, the MC event is reweighed according to the ratio of new parton distributions to the distributions used in the generation of the MC.

Finally the effect of the choice of the jet energy correction parametrization and the uncertainty of the bin-by-bin correction factor related to the parametrization is estimated by changing the $\langle E_T^{det}/E_T^{had}\rangle$ profiling to the $\langle E_T^{had} - E_T^{det}\rangle$ one, as shown in figure 6.5.

In addition to these systematic studies, two other sources of the uncertainty are considered. One is the entire energy scale uncertainty of $+7(-5)\%$. The other effect is the uncertainty of the integrated luminosity(1.0%) as discussed in section 3.2.4.

The result of the systematic study is plotted in figures 8.10 and 8.11 for $d\sigma/dE_T d\eta_1 d\eta_2$, and 8.12, 8.13 and 8.14 for $(d\sigma/d\eta_2)|_{E_T>E_T^{thr},\eta_1}$. The total systematic error of each bin Δ_{total} is calculated by adding the fourteen uncertainties in quadrature considering the statistical significance of each study:

$$\Delta_{total} = \sqrt{\frac{\sum_i (\Delta_i/\sigma_i)^2}{(1/\sigma_{nominal})^2}}.$$

Here Δ_i denotes the systematic uncertainty of the i-th study defined as the cross section deviation from the nominal one. σ_i denotes the statistical error of the cross section on the i-th systematic study. $\sigma_{nominal}$ is the statistical error on the nominal study. The additional effects, the energy scale and the luminosity uncertainty, is not added to the systematic error estimation. The cross section uncertainty due to the energy scale is indicated as a dotted line in each histogram of the systematic studies.

Among these fourteen uncertainties, the following uncertainties are of importance. The effect from the HERWIG MI and HERWIG is difficult to judge due to the small statistics of these samples. No large systematic shift, however, is observed apart from the lowest E_T bins in $d\sigma/dE_T d\eta_1 d\eta_2$. The change of the p_Z/E cut affects the bins of the kinematical limit on the large rapidity bins. The p_Z/E cut has an effect on these bins near the lower boundary of y, The change of the cut of the higher y_{JB} boundary is affected in the smallest rapidity bins in the $(d\sigma/d\eta_2)|_{E_T>E_T^{thr},\eta_1}$ since these bins are on the boundary of $y < 0.85$. The behavior of the effect from the change of the y_{JB} scale is different between the whole x_γ range and $x_\gamma > 0.75$ due to the change of the source of the scale shift. In both cases the error is one of the largest among these studies. The effect from the change of the photon or proton structure function is very small. The change of

the energy correction parameter results up to 15% decrease of the cross section for the lowest E_T bins in $d\sigma/dE_T d\eta_1 d\eta_2$. Apart from the lowest E_T bin, the agreement between the two parametrizations is quite well. This indicates that there is no strong dependence on the energy correction parametrization.

8.4 Comparison with models

Figure 8.15 shows the comparison of the measured cross section $d\sigma/dE_T d\eta_1 d\eta_2$ with the models: PYTHIA, PYTHIA(LAC1), HERWIG and HERWIG with MI in the hadron level. The cross section is plotted as the ratio of the cross section to the PYTHIA prediction. In comparison with PYTHIA, that the measured cross section shows a large excess in case both jets go forward ($\eta_1, \eta_2 > 1$). The cross section in the region $x_\gamma > 0.75$ is underestimated.

If one change the photon structure function in PYTHIA from GRV-LO to LAC1 (solid line), the cross section increases where both jets go forward, but this only explains part of the forward excess. With LAC1, the cross section also increases in case one jet is in the forward ($\eta > 1$) and the other is in backward ($\eta < 0$). This is not observed in the measured cross section. Changing the proton structure function (not shown) does not affect the cross section of the PYTHIA model.

The HERWIG model(dashed line) underestimates the cross section both in the entire x_γ and $x_\gamma > 0.75$. In $x_\gamma > 0.75$, the absolute cross section is similar to PYTHIA. Apart from the absolute prediction, HERWIG describes the shape of the cross section fairly well except the forward excess.

The prediction from HERWIG model with MI is also shown in the entire x_γ range. The cross sections in figure 8.15 are shown only E_T below 25 GeV due to the low statistics of the MC(similar to the data). Though the cross section is larger than HERWIG, this is not enough to describe the forward excess in the data.

		entire x_γ range		$x_\gamma > 0.75$	
	η_2 range	$\langle\eta_2\rangle$	$\sigma(\pm\text{stat.}\pm\text{syst.}\pm\text{Escale})$[nb]	$\langle\eta_2\rangle$	$\sigma(\pm\text{stat.}\pm\text{syst.}\pm\text{Escale})$[nb]
$1 < \eta_1 < 2$	[-1.00, -0.75]	-0.87	$8.37 \pm 1.77 \pm 3.08^{+2.14}_{-1.75} \times 10^{-2}$	-0.88	$7.47 \pm 1.69 \pm 2.18^{+0.00}_{-2.04} \times 10^{-2}$
	[-0.75, -0.50]	-0.62	$1.37 \pm 0.20 \pm 0.19^{+0.75}_{-0.30} \times 10^{-1}$	-0.62	$9.67 \pm 1.92 \pm 1.45^{+4.25}_{-1.66} \times 10^{-1}$
	[-0.50, -0.25]	-0.36	$1.82 \pm 0.22 \pm 0.31^{+0.72}_{-0.44} \times 10^{-1}$	-0.35	$9.05 \pm 1.55 \pm 0.98^{+2.11}_{-0.54} \times 10^{-1}$
	[-0.25, 0.00]	-0.11	$2.38 \pm 0.25 \pm 0.22^{+0.75}_{-0.46} \times 10^{-1}$	-0.12	$1.01 \pm 0.17 \pm 0.22^{+0.42}_{-0.18} \times 10^{-1}$
	[0.00, 0.25]	0.13	$3.14 \pm 0.27 \pm 0.32^{+1.00}_{-0.61} \times 10^{-1}$	0.13	$1.39 \pm 0.18 \pm 0.15^{+0.34}_{-0.24} \times 10^{-1}$
	[0.25, 0.50]	0.38	$3.08 \pm 0.25 \pm 0.44^{+1.20}_{-0.34} \times 10^{-1}$	0.38	$1.15 \pm 0.15 \pm 0.26^{+0.29}_{-0.09} \times 10^{-1}$
	[0.50, 0.75]	0.63	$3.00 \pm 0.26 \pm 0.32^{+1.55}_{-0.33} \times 10^{-1}$	0.62	$7.09 \pm 1.11 \pm 1.69^{+2.77}_{-0.71} \times 10^{-1}$
	[0.75, 1.00]	0.87	$3.11 \pm 0.26 \pm 0.25^{+1.25}_{-0.72} \times 10^{-1}$	0.86	$4.87 \pm 0.90 \pm 1.27^{+0.95}_{-1.00} \times 10^{-1}$
	[1.00, 1.25]	1.13	$2.50 \pm 0.24 \pm 0.38^{+1.07}_{-0.50} \times 10^{-1}$	1.09	$1.41 \pm 0.47 \pm 2.60^{+1.04}_{-0.28} \times 10^{-1}$
	[1.25, 1.50]	1.37	$2.30 \pm 0.22 \pm 0.48^{+1.07}_{-0.48} \times 10^{-1}$	–	–
	[1.50, 1.75]	1.62	$2.77 \pm 0.26 \pm 0.44^{+1.16}_{-0.50} \times 10^{-1}$	–	–
	[1.75, 2.00]	1.87	$2.94 \pm 0.30 \pm 0.62^{+1.95}_{-0.61} \times 10^{-1}$	–	–
$0 < \eta_1 < 1$	[-1.00, -0.75]	-0.84	$7.64 \pm 1.54 \pm 1.68^{+3.69}_{-0.59} \times 10^{-2}$	-0.84	$7.80 \pm 1.61 \pm 2.64^{+3.52}_{-0.87} \times 10^{-2}$
	[-0.75, -0.50]	-0.62	$1.34 \pm 0.19 \pm 0.36^{+0.20}_{-0.18} \times 10^{-1}$	-0.62	$1.15 \pm 0.17 \pm 0.25^{+0.31}_{-0.13} \times 10^{-1}$
	[-0.50, -0.25]	-0.38	$1.83 \pm 0.21 \pm 0.16^{+0.49}_{-0.40} \times 10^{-1}$	-0.38	$1.45 \pm 0.20 \pm 0.14^{+0.28}_{-0.26} \times 10^{-1}$
	[-0.25, 0.00]	-0.12	$2.19 \pm 0.21 \pm 0.17^{+0.57}_{-0.44} \times 10^{-1}$	-0.13	$1.46 \pm 0.18 \pm 0.10^{+0.22}_{-0.12} \times 10^{-1}$
	[0.00, 0.25]	0.12	$2.39 \pm 0.22 \pm 0.11^{+0.73}_{-0.46} \times 10^{-1}$	0.12	$1.76 \pm 0.22 \pm 0.20^{+0.43}_{-0.38} \times 10^{-1}$
	[0.25, 0.50]	0.38	$2.36 \pm 0.22 \pm 0.32^{+0.83}_{-0.47} \times 10^{-1}$	0.37	$1.38 \pm 0.17 \pm 0.36^{+0.59}_{-0.25} \times 10^{-1}$
	[0.50, 0.75]	0.63	$2.96 \pm 0.25 \pm 0.50^{+0.65}_{-0.44} \times 10^{-1}$	0.63	$1.49 \pm 0.18 \pm 0.37^{+0.38}_{-0.18} \times 10^{-1}$
	[0.75, 1.00]	0.87	$2.30 \pm 0.21 \pm 0.32^{+0.98}_{-0.23} \times 10^{-1}$	0.87	$1.34 \pm 0.18 \pm 0.24^{+0.61}_{-0.15} \times 10^{-1}$
	[1.00, 1.25]	1.12	$3.22 \pm 0.27 \pm 0.33^{+0.84}_{-0.49} \times 10^{-1}$	1.12	$1.28 \pm 0.17 \pm 0.33^{+0.31}_{-0.24} \times 10^{-1}$
	[1.25, 1.50]	1.37	$3.12 \pm 0.26 \pm 0.15^{+1.39}_{-0.39} \times 10^{-1}$	1.37	$1.06 \pm 0.15 \pm 0.15^{+0.30}_{-0.17} \times 10^{-1}$
	[1.50, 1.75]	1.62	$2.85 \pm 0.24 \pm 0.20^{+1.47}_{-0.43} \times 10^{-1}$	1.62	$8.18 \pm 1.21 \pm 0.92^{+2.82}_{-0.28} \times 10^{-1}$
	[1.75, 2.00]	1.87	$3.10 \pm 0.26 \pm 0.30^{+1.24}_{-0.62} \times 10^{-1}$	1.87	$5.46 \pm 1.00 \pm 1.00^{+1.25}_{-0.48} \times 10^{-1}$
$-1 < \eta_1 < 0$	[-0.75, -0.50]	-0.60	$2.62 \pm 0.83 \pm 1.81^{+0.77}_{-0.47} \times 10^{-2}$	-0.60	$2.69 \pm 0.86 \pm 1.37^{+0.37}_{-0.26} \times 10^{-2}$
	[-0.50, -0.25]	-0.36	$8.34 \pm 1.36 \pm 3.79^{+1.63}_{-0.78} \times 10^{-2}$	-0.36	$8.53 \pm 1.41 \pm 1.62^{+1.77}_{-0.35} \times 10^{-2}$
	[-0.25, 0.00]	-0.12	$1.28 \pm 0.19 \pm 0.33^{+0.19}_{-0.28} \times 10^{-1}$	-0.13	$1.25 \pm 0.19 \pm 0.21^{+0.19}_{-0.23} \times 10^{-1}$
	[0.00, 0.25]	0.13	$1.22 \pm 0.16 \pm 0.26^{+0.18}_{-0.22} \times 10^{-1}$	0.13	$1.15 \pm 0.17 \pm 0.21^{+0.16}_{-0.22} \times 10^{-1}$
	[0.25, 0.50]	0.38	$1.48 \pm 0.20 \pm 0.18^{+0.37}_{-0.30} \times 10^{-1}$	0.39	$1.21 \pm 0.18 \pm 0.23^{+0.34}_{-0.19} \times 10^{-1}$
	[0.50, 0.75]	0.63	$1.76 \pm 0.20 \pm 0.16^{+0.63}_{-0.22} \times 10^{-1}$	0.63	$1.32 \pm 0.18 \pm 0.16^{+0.31}_{-0.07} \times 10^{-1}$
	[0.75, 1.00]	0.88	$1.66 \pm 0.20 \pm 0.26^{+0.44}_{-0.36} \times 10^{-1}$	0.87	$1.17 \pm 0.17 \pm 0.26^{+0.28}_{-0.11} \times 10^{-1}$
	[1.00, 1.25]	1.12	$1.84 \pm 0.24 \pm 0.17^{+0.82}_{-0.31} \times 10^{-1}$	1.12	$9.78 \pm 1.62 \pm 2.45^{+1.85}_{-1.71} \times 10^{-1}$
	[1.25, 1.50]	1.38	$1.81 \pm 0.23 \pm 0.31^{+0.52}_{-0.52} \times 10^{-1}$	1.37	$1.06 \pm 0.18 \pm 0.13^{+0.31}_{-0.18} \times 10^{-1}$
	[1.50, 1.75]	1.61	$1.51 \pm 0.20 \pm 0.23^{+0.65}_{-0.23} \times 10^{-1}$	1.62	$9.34 \pm 1.78 \pm 1.22^{+3.03}_{-1.35} \times 10^{-1}$
	[1.75, 2.00]	1.86	$1.28 \pm 0.18 \pm 0.21^{+0.42}_{-0.32} \times 10^{-1}$	1.87	$6.18 \pm 1.43 \pm 0.80^{+0.38}_{-0.91} \times 10^{-1}$

Table 8.5: The measured cross section $(d\sigma/d\eta_2)|_{E_T > E_T^{\text{lab}}, \eta_1}$ of the event with $E_T > 14$GeV.

		entire x_γ range		$x_\gamma > 0.75$	
	η_2 range	$\langle\eta_2\rangle$	$\sigma(\pm\text{stat.}\pm\text{syst.}\pm\text{Escale})$[nb]	$\langle\eta_2\rangle$	$\sigma(\pm\text{stat.}\pm\text{syst.}\pm\text{Escale})$[nb]
$1 < \eta_1 < 2$	[-0.75, -0.50]	-0.61	$7.91 \pm 1.37 \pm 2.55^{+2.79}_{-2.22} \times 10^{-2}$	-0.60	$5.79 \pm 1.26 \pm 1.42^{+1.42}_{-1.47} \times 10^{-2}$
	[-0.50, -0.25]	-0.37	$1.11 \pm 0.14 \pm 0.18^{+0.41}_{-0.18} \times 10^{-1}$	-0.37	$7.57 \pm 1.21 \pm 1.56^{+2.67}_{-1.36} \times 10^{-1}$
	[-0.25, 0.00]	-0.12	$2.09 \pm 0.19 \pm 0.19^{+0.73}_{-0.37} \times 10^{-1}$	-0.12	$1.24 \pm 0.15 \pm 0.17^{+0.34}_{-0.15} \times 10^{-1}$
	[0.00, 0.25]	0.13	$2.27 \pm 0.19 \pm 0.19^{+0.83}_{-0.38} \times 10^{-1}$	0.12	$1.13 \pm 0.13 \pm 0.13^{+0.34}_{-0.15} \times 10^{-1}$
	[0.25, 0.50]	0.38	$2.77 \pm 0.21 \pm 0.32^{+0.97}_{-0.53} \times 10^{-1}$	0.38	$1.11 \pm 0.13 \pm 0.15^{+0.37}_{-0.17} \times 10^{-1}$
	[0.50, 0.75]	0.63	$3.05 \pm 0.22 \pm 0.30^{+1.01}_{-0.60} \times 10^{-1}$	0.63	$1.43 \pm 0.15 \pm 0.23^{+0.42}_{-0.21} \times 10^{-1}$
	[0.75, 1.00]	0.87	$2.72 \pm 0.20 \pm 0.15^{+1.20}_{-0.46} \times 10^{-1}$	0.87	$1.13 \pm 0.14 \pm 0.16^{+0.46}_{-0.14} \times 10^{-1}$
	[1.00, 1.25]	1.12	$2.68 \pm 0.21 \pm 0.15^{+1.31}_{-0.49} \times 10^{-1}$	1.12	$8.99 \pm 1.22 \pm 1.94^{+4.15}_{-1.18} \times 10^{-1}$
	[1.25, 1.50]	1.37	$2.43 \pm 0.19 \pm 0.19^{+1.31}_{-0.48} \times 10^{-1}$	1.37	$6.58 \pm 0.96 \pm 0.89^{+3.63}_{-0.83} \times 10^{-1}$
	[1.50, 1.75]	1.62	$2.39 \pm 0.19 \pm 0.23^{+1.48}_{-0.45} \times 10^{-1}$	1.62	$3.41 \pm 0.63 \pm 0.52^{+3.08}_{-0.43} \times 10^{-1}$
	[1.75, 2.00]	1.87	$2.55 \pm 0.20 \pm 0.28^{+1.79}_{-0.48} \times 10^{-1}$	1.86	$2.98 \pm 0.61 \pm 0.26^{+3.78}_{-0.37} \times 10^{-1}$
$0 < \eta_1 < 1$	[-0.75, -0.50]	-0.61	$7.34 \pm 1.38 \pm 3.59^{+2.68}_{-0.91} \times 10^{-2}$	-0.61	$6.86 \pm 1.24 \pm 2.42^{+2.40}_{-0.65} \times 10^{-2}$
	[-0.50, -0.25]	-0.36	$9.46 \pm 1.31 \pm 1.73^{+4.44}_{-1.29} \times 10^{-2}$	-0.37	$9.18 \pm 1.34 \pm 1.98^{+3.14}_{-1.39} \times 10^{-2}$
	[-0.25, 0.00]	-0.13	$1.65 \pm 0.18 \pm 0.37^{+0.53}_{-0.25} \times 10^{-1}$	-0.12	$1.39 \pm 0.15 \pm 0.14^{+0.39}_{-0.24} \times 10^{-1}$
	[0.00, 0.25]	0.13	$1.82 \pm 0.16 \pm 0.25^{+0.51}_{-0.27} \times 10^{-1}$	0.13	$1.40 \pm 0.15 \pm 0.30^{+0.36}_{-0.18} \times 10^{-1}$
	[0.25, 0.50]	0.38	$1.85 \pm 0.16 \pm 0.14^{+0.57}_{-0.28} \times 10^{-1}$	0.37	$1.22 \pm 0.13 \pm 0.15^{+0.32}_{-0.17} \times 10^{-1}$
	[0.50, 0.75]	0.63	$2.09 \pm 0.17 \pm 0.16^{+0.62}_{-0.34} \times 10^{-1}$	0.63	$1.47 \pm 0.14 \pm 0.20^{+0.37}_{-0.20} \times 10^{-1}$
	[0.75, 1.00]	0.88	$2.62 \pm 0.20 \pm 0.18^{+0.82}_{-0.41} \times 10^{-1}$	0.87	$1.37 \pm 0.15 \pm 0.17^{+0.33}_{-0.17} \times 10^{-1}$
	[1.00, 1.25]	1.13	$2.51 \pm 0.21 \pm 0.14^{+0.95}_{-0.43} \times 10^{-1}$	1.12	$1.29 \pm 0.15 \pm 0.20^{+0.44}_{-0.15} \times 10^{-1}$
	[1.25, 1.50]	1.37	$2.95 \pm 0.21 \pm 0.18^{+1.07}_{-0.57} \times 10^{-1}$	1.37	$1.52 \pm 0.15 \pm 0.20^{+0.55}_{-0.23} \times 10^{-1}$
	[1.50, 1.75]	1.62	$2.80 \pm 0.21 \pm 0.21^{+0.99}_{-0.48} \times 10^{-1}$	1.62	$1.06 \pm 0.13 \pm 0.16^{+0.29}_{-0.18} \times 10^{-1}$
	[1.75, 2.00]	1.87	$2.52 \pm 0.19 \pm 0.15^{+0.99}_{-0.49} \times 10^{-1}$	1.87	$8.96 \pm 1.17 \pm 0.93^{+3.16}_{-1.47} \times 10^{-1}$
$-1 < \eta_1 < 0$	[-0.25, 0.00]	-0.11	$4.02 \pm 0.80 \pm 1.91^{+3.09}_{-0.29} \times 10^{-2}$	-0.11	$3.82 \pm 0.78 \pm 1.61^{+2.75}_{-0.40} \times 10^{-2}$
	[0.00, 0.25]	0.15	$5.94 \pm 1.23 \pm 2.69^{+2.66}_{-0.88} \times 10^{-2}$	0.13	$6.03 \pm 1.17 \pm 1.95^{+2.02}_{-0.88} \times 10^{-2}$
	[0.25, 0.50]	0.38	$9.33 \pm 1.38 \pm 2.69^{+2.94}_{-1.53} \times 10^{-2}$	0.38	$7.53 \pm 1.13 \pm 1.28^{+2.35}_{-1.09} \times 10^{-2}$
	[0.50, 0.75]	0.63	$9.26 \pm 1.24 \pm 1.90^{+3.52}_{-1.73} \times 10^{-2}$	0.62	$8.31 \pm 1.23 \pm 1.70^{+2.49}_{-1.73} \times 10^{-2}$
	[0.75, 1.00]	0.88	$9.91 \pm 1.35 \pm 2.01^{+3.94}_{-1.38} \times 10^{-2}$	0.88	$9.23 \pm 1.32 \pm 1.80^{+2.99}_{-1.30} \times 10^{-2}$
	[1.00, 1.25]	1.13	$1.04 \pm 0.14 \pm 0.21^{+0.36}_{-0.23} \times 10^{-1}$	1.12	$7.70 \pm 1.29 \pm 1.79^{+1.94}_{-1.45} \times 10^{-1}$
	[1.25, 1.50]	1.37	$1.10 \pm 0.15 \pm 0.15^{+0.38}_{-0.20} \times 10^{-1}$	1.37	$7.92 \pm 1.42 \pm 1.06^{+2.04}_{-1.44} \times 10^{-1}$
	[1.50, 1.75]	1.62	$1.11 \pm 0.13 \pm 0.23^{+0.40}_{-0.21} \times 10^{-1}$	1.62	$6.99 \pm 1.11 \pm 1.30^{+2.51}_{-1.10} \times 10^{-1}$
	[1.75, 2.00]	1.87	$9.71 \pm 1.30 \pm 2.08^{+3.48}_{-1.93} \times 10^{-2}$	1.87	$5.49 \pm 1.03 \pm 4.35^{+2.23}_{-1.15} \times 10^{-2}$

Table 8.6: The measured cross section $(d\sigma/d\eta_2)|_{E_T > E_T^{\text{lab}}, \eta_1}$ of the event with $E_T > 17$GeV.

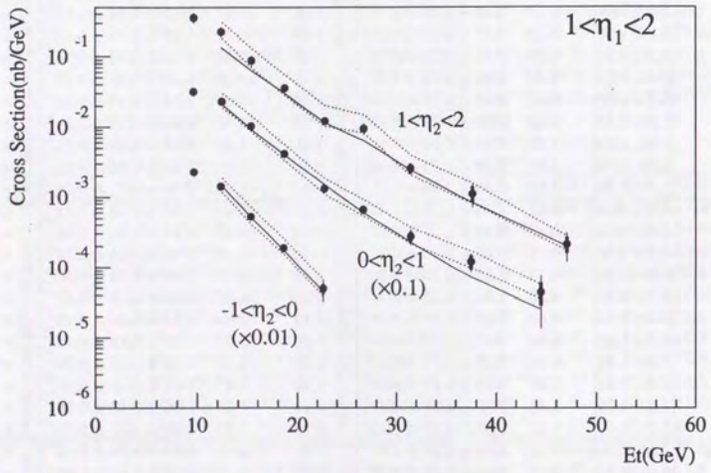

Figure 8.7: $d\sigma/dE_T d\eta_1 d\eta_2$ in the entire range of x_γ of the rapidity region $1 < \eta_1 < 2$(this page), $0 < \eta_1 < 1$ and $-1 < \eta_1 < 0$(next page). The inner thick error bar shows the statistical error and the outer thinner error bar is the addition of the statistical and systematic error in quadrature. The solid line is the prediction of the PYTHIA MC. The band drawn by the two dotted lines indicate the uncertainty due to the energy scale, which is not included in the systematic error.

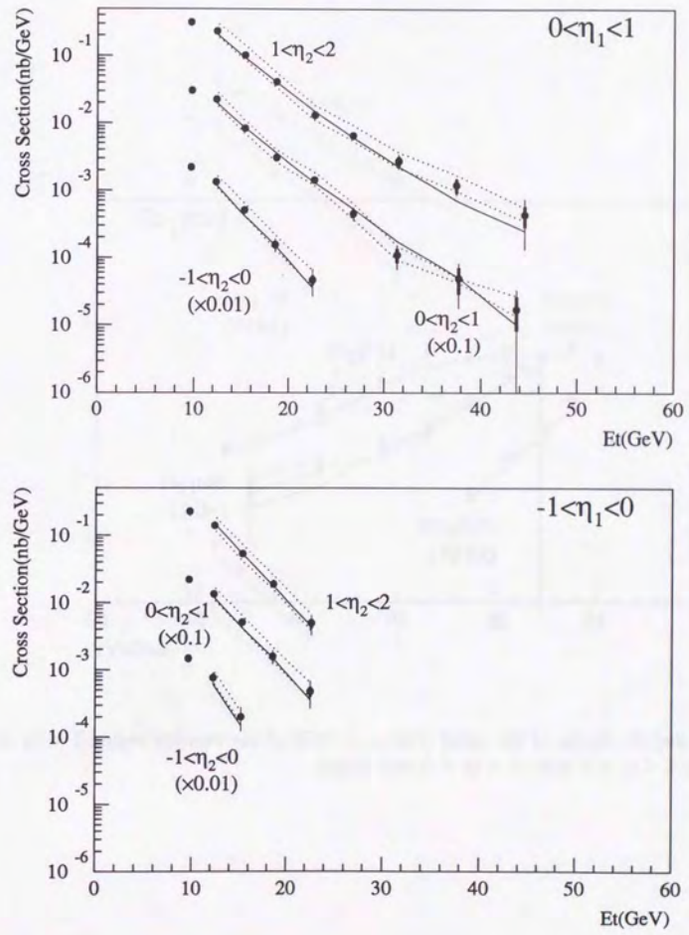

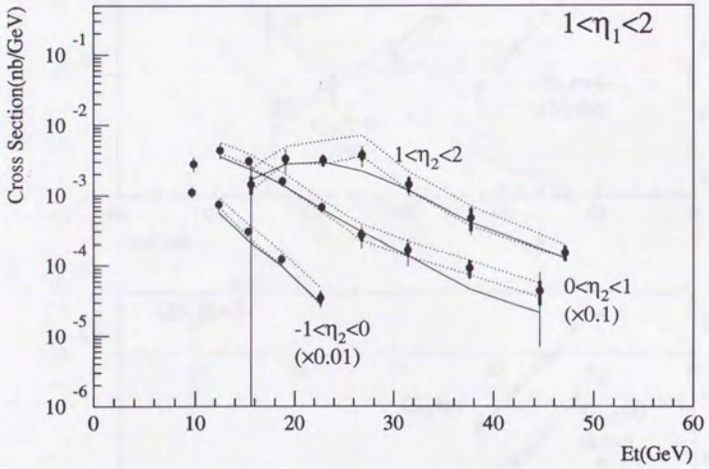

Figure 8.8: $d\sigma/dE_T d\eta_1 d\eta_2$ of the event with $x_\gamma > 0.75$ of the rapidity region $1 < \eta_1 < 2$(this page), $0 < \eta_1 < 1$ and $-1 < \eta_1 < 0$(next page).

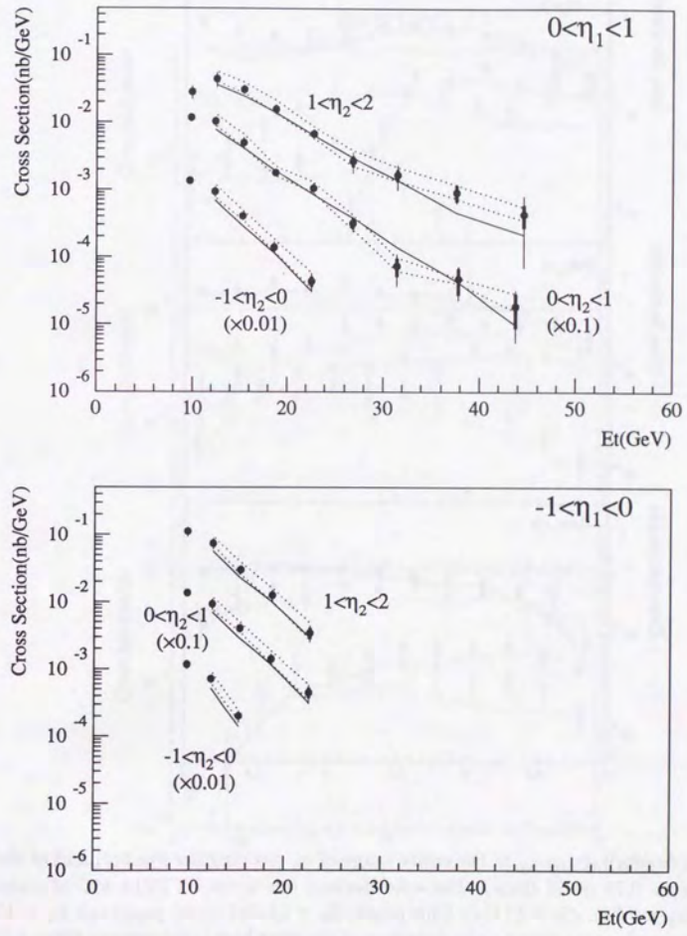

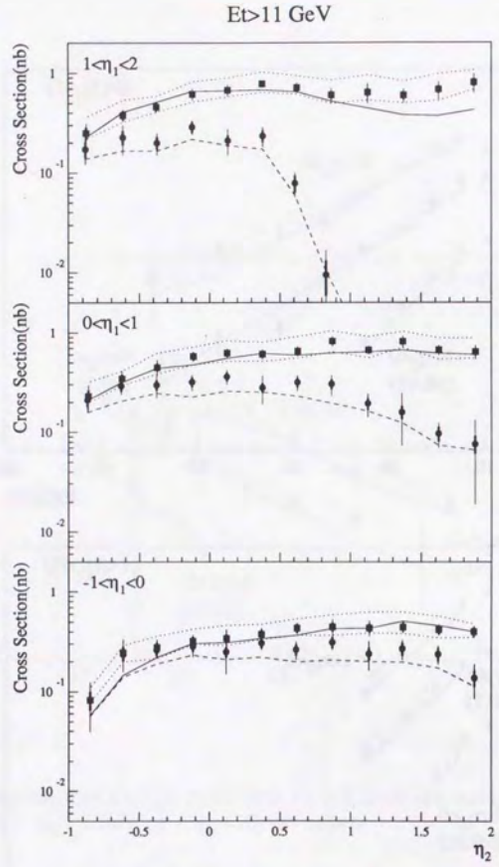

Figure 8.9: $(d\sigma/d\eta_2)|_{E_T>E_T^{thr},\eta_1}$ in the entire range of x_γ (rectangular symbol) and of the event with $x_\gamma > 0.75$ (solid circle). The solid(dashed) line is the PYTHIA MC of entire range of $x_\gamma(x_\gamma > 0.75)$. $E_T > 11$ GeV (this page), $E_T > 14$ GeV (next page) and $E_T > 17$ GeV (two pages after) are shown. The definition of the error bars is the same as figure 8.7.

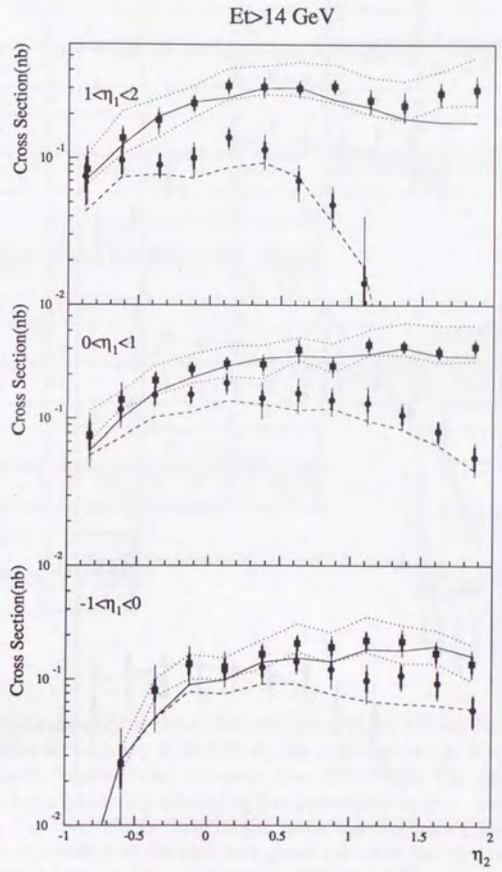

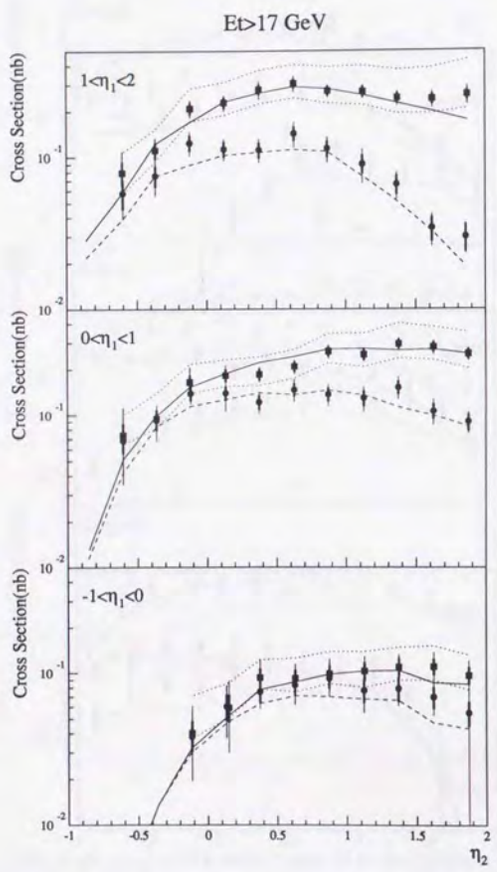

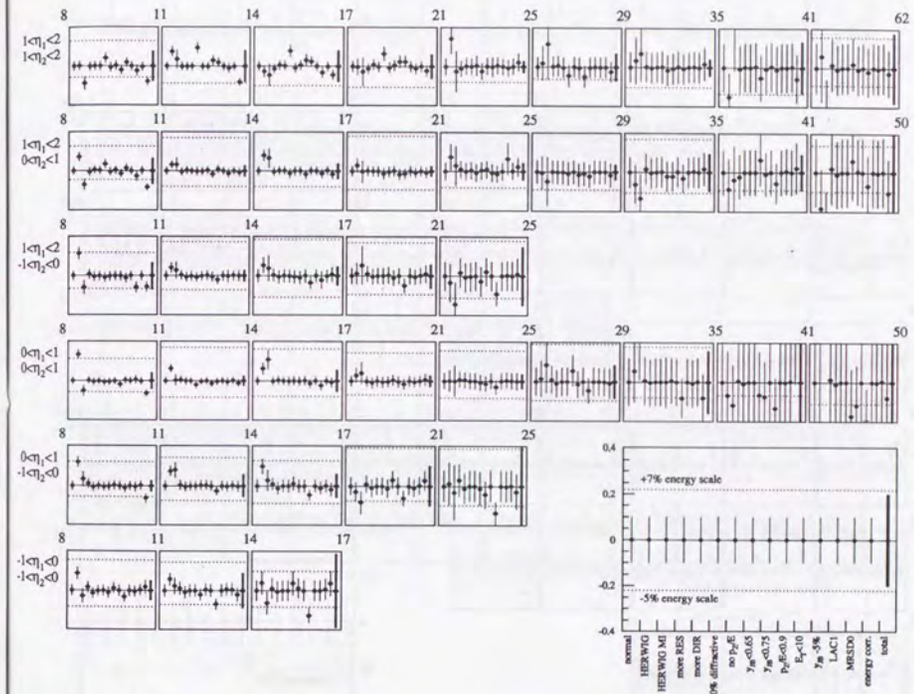

Figure 8.10: The summary of the systematic error of $d\sigma/dE_T d\eta_1 d\eta_2$. The result of the systematic studies for each bin of $d\sigma/dE_T d\eta_1 d\eta_2$ is plotted in one histogram, as a ratio to the nominal result, together with the error from each study. The meaning of each point is listed in the large histogram plotted in the lower right corner. Each row of histogram corresponds to the cross section bins of the given rapidity region listed on the left side. The number on the corner of the each histogram indicates the E_T boundary of each bin. The vertical axis is ranging from -0.4 to 0.4, showing $\pm 40\%$ deviation. The dotted lines indicate the uncertainty range from the energy scale study. The thick line situated in the rightmost of each histogram indicates the total systematic errors.

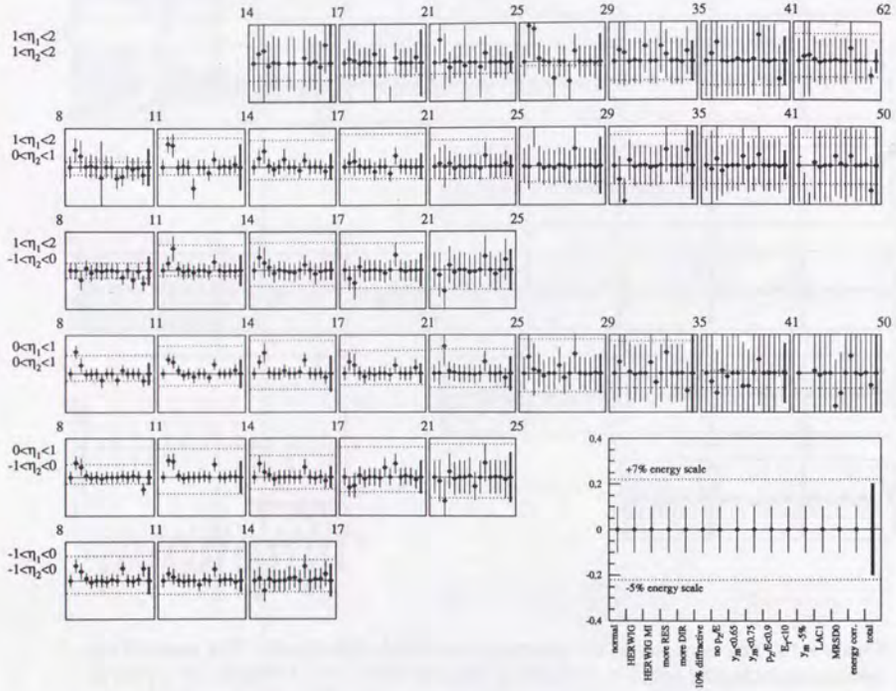

Figure 8.11: The summary of the systematic error of $d\sigma/dE_T d\eta_1 d\eta_2$ for the event with $x_\gamma > 0.75$. The definition of the histograms are the same as figure 8.10.

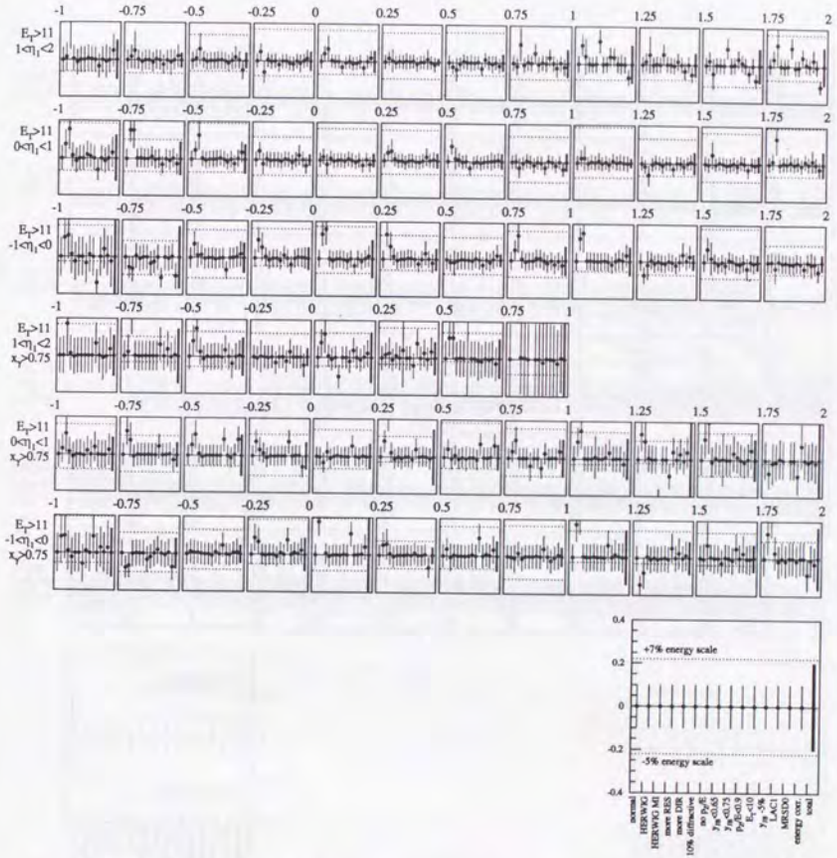

Figure 8.12: The summary of the systematic error of $(d\sigma/d\eta_2)|_{E_T > E_T^{thr}, \eta_1}$ for the event of $E_T > 11$GeV. Each row of histogram corresponds to the cross section bins of the given E_T and the first jet rapidity region listed on the left side. The number on each histogram corner shows the boundary of the rapidity of the second jet of each bin. The definition of the points in the histogram is listed as the same as figure 8.10.

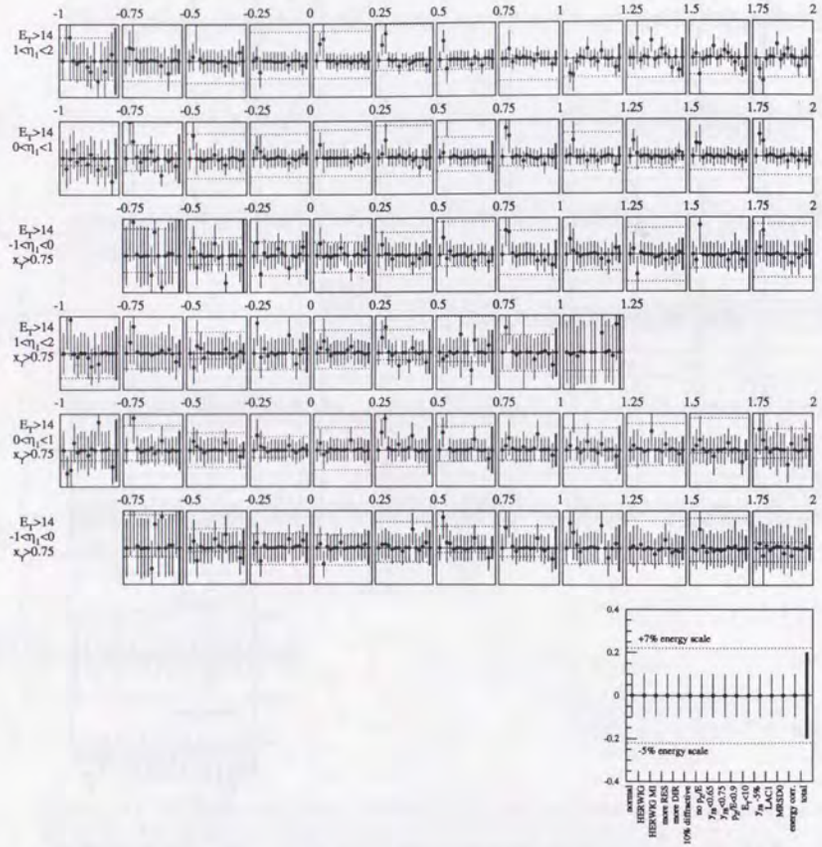

Figure 8.13: The summary of the systematic error of $(d\sigma/d\eta_2)|_{E_T>E_T^{thr},\eta_1}$ for the event of $E_T > 14$GeV. The definition of the histograms is the same as figure 8.12.

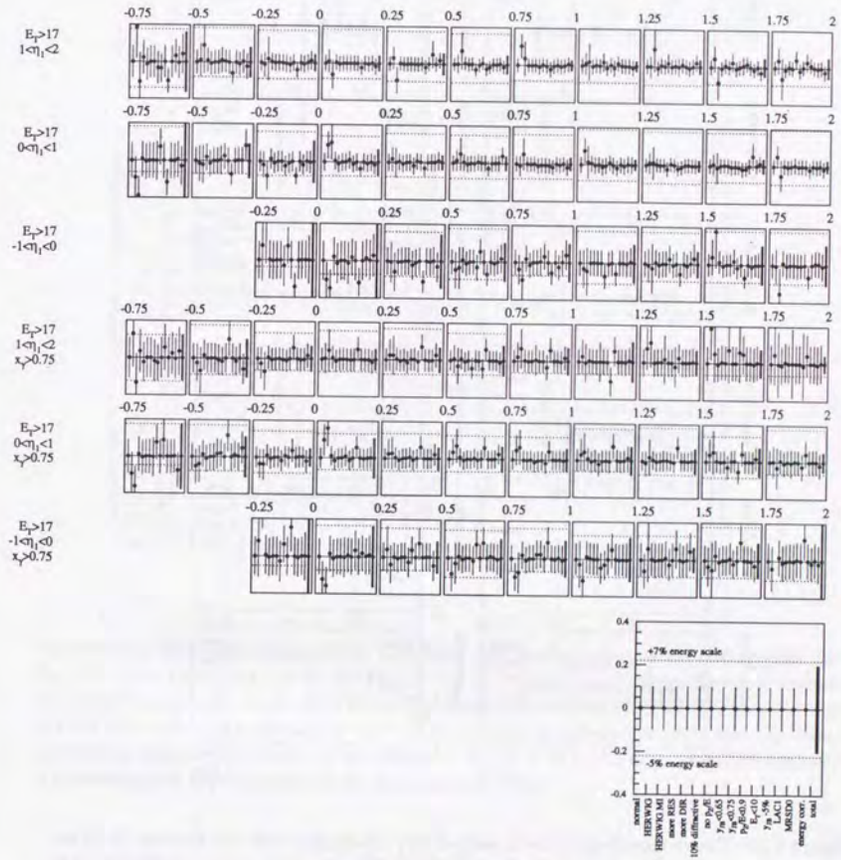

Figure 8.14: The summary of the systematic error of $(d\sigma/d\eta_2)|_{E_T>E_T^{thr},\eta_1}$ for the event of $E_T > 17$GeV. The definition of the histograms is the same as figure 8.12.

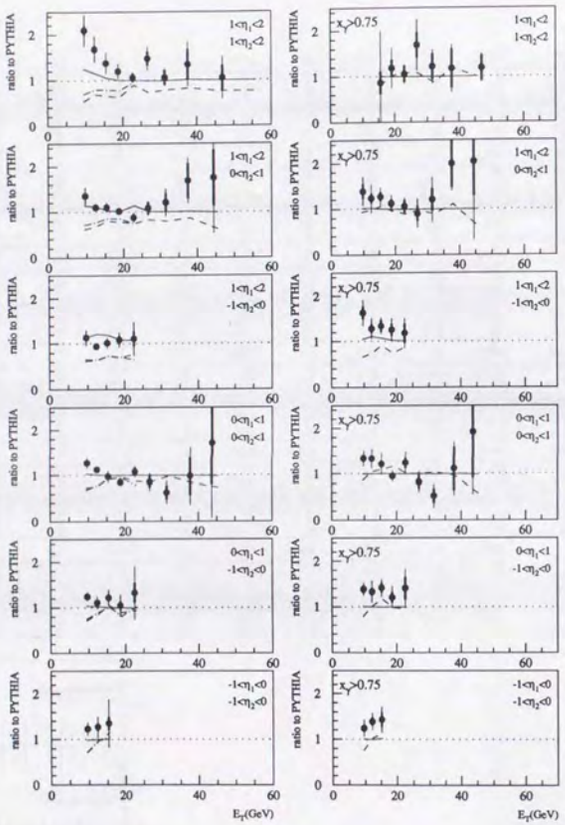

Figure 8.15: The comparison of the measured $d\sigma/dE_T d\eta_1 d\eta_2$ with the models. Here the cross section is plotted as the ratio to the PYTHIA. The dashed line shows HERWIG. The solid line is PYTHIA with LAC1 instead of GRV as the photon structure function, and the dash-dotted line shows HERWIG with MI. Both PYTHIA with LAC1 and HERWIG with MI is shown only in the cross section for the entire x_γ range. HERWIG MI is shown in only $E_T < 25$ GeV due to the low statistics in the high-E_T region.

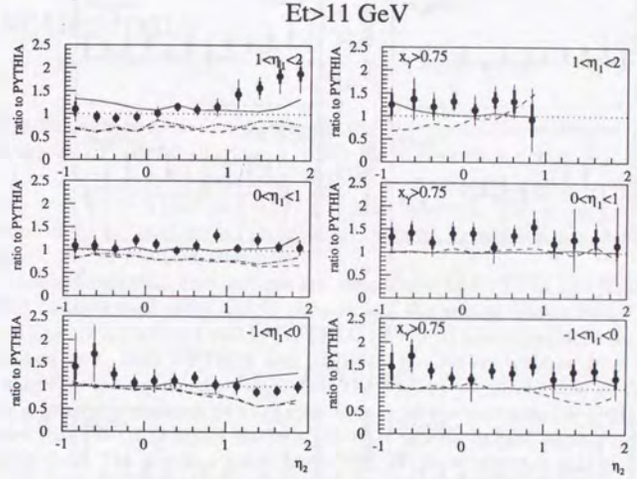

Figure 8.16: The comparison of the measured $(d\sigma/d\eta_2)|_{E_T>E_T^{thr},\eta_1}$ with the models, for $E_T > 11$ GeV (this page), > 14 GeV and > 17 GeV (next page). Here the cross section is plotted as the ratio to the PYTHIA. The dashed line shows HERWIG. The solid line is PYTHIA with LAC1 instead of GRV as the photon structure function, and the dash-dotted line shows HERWIG with MI. Both PYTHIA with LAC1 and HERWIG with MI is shown only in the cross section for the entire x_γ range.

Et>14 GeV

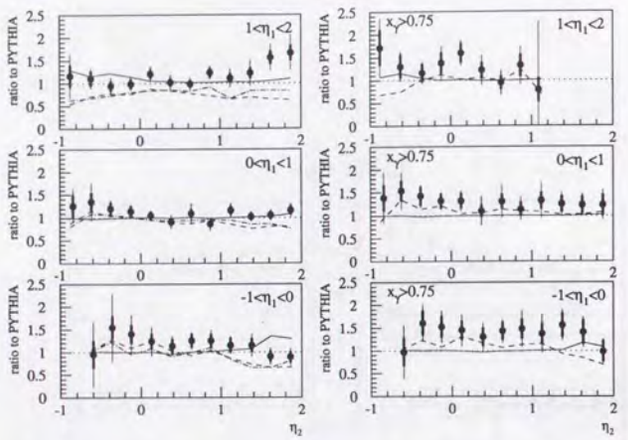

Et>17 GeV

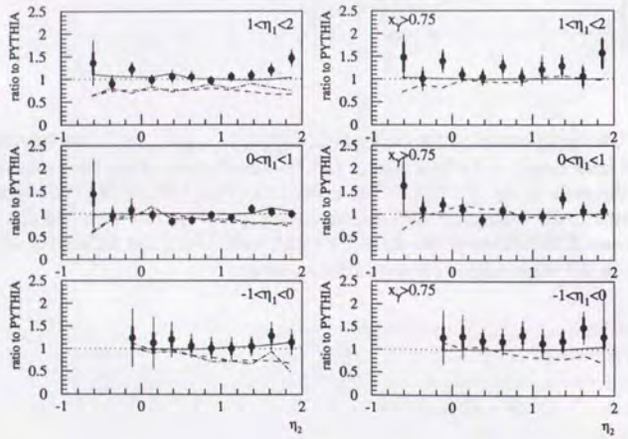

Chapter 9

Discussions

By the previous chapter the first measurement of the triple differential dijet cross sections, $d\sigma/dE_T d\eta_1 d\eta_2$ and $(d\sigma/d\eta_2)|_{E_T>E_T^{thr},\eta_1}$, in a photoproduction regime ($Q^2 < 4\text{GeV}^2$ and $0.2 < y < 0.85$) has been presented. For the measurement, events containing two or more jets with $E_T > 8$ GeV and $-1 < \eta < 2$ are selected. The jet rate and the energy correlation of the first and second jet are also presented. In addition, the transverse energy flow around the jet has been evaluated.

The triple differential cross sections are compared with PYTHIA and HERWIG, which are based on the lowest order matrix element and the parton shower model. The overall cross sections are reproduced well by PYTHIA. HERWIG also reproduced the shape of the cross section well. Both PYTHIA and HERWIG models are inspired from perturbative QCD, therefore the agreement means that the high-p_T jet production in the photoproduction is generally understood in the framework of the perturbative QCD. This thesis confirmed that the QCD model works in the dijet process in hard photoproduction up to $E_{T_{jet}} \simeq 50$ GeV. The previous publications [26, 61] have reported that the inclusive jet cross section can be described by the parton-parton scattering model. This thesis further verified the agreement for the dijet events.

The jet rate and the energy correlation of the first and the second jets also agree with the PYTHIA prediction well. Since these effects are due to the higher order effect, it can be concluded that the higher order effect is well simulated by the parton shower in terms of the jet topology.

There are, however, some disagreements in the measured quantities. First, the measured dijet cross section excesses the PYTHIA or HERWIG model in the positive rapidity direction. This thesis showed that the excess is mainly for the case that both jets are in the forward region ($\eta_1, \eta_2 > 1$, see figure 8.16). It is also seen that the amount of the excess is prominent in the low E_T jet and becomes smaller as the jet E_T becomes higher (see figure 8.15). This excess cannot be accounted for with the change of the proton structure function. The dependence on the photon structure function is tested by LAC1 parametrisation. Since this parametrisation has the softest gluon distribution among the commonly used parametrisations, the cross section is expected to exceed in the small x_γ region, i.e., the forward region. After changing from GRV-LO to LAC1, only the part of the excess

is described. Therefore, the forward excess cannot be fully explained by changing the photon structure function within the range that is allowed in the current framework of the calculation of the parton densities in the photon discussed in section 2.2.3.

Second, the excess of the transverse energy flow around the jet, or the jet E_T pedestal, over the PYTHIA and HERWIG models is observed. The excess is observed in the forward-going jet ($0 < \eta_{jet} < 2$). In this region, the excess becomes larger as the E_T of the jet becomes smaller. For the jet with $1 < \eta_{jet} < 2$, the excess is seen for the jet with E_T up to 21 GeV. The excess also depends on the rapidity of the other jet. When it goes forward, the excess becomes larger.

Lastly, the cross sections are generally underestimated by the models. The PYTHIA model predicts the absolute cross section of the whole x_γ region well, though the cross section in $x_\gamma > 0.75$ is smaller than the data. The prediction of HERWIG is lower than the measured cross section in both the whole x_γ region. The same statement is applied when the x_γ region is limited above 0.75 (see figure 8.15 and 8.16).

The excess of the forward cross section was reported in the previous publications, in both the inclusive jet cross section [26] and the dijet [28] cross section. The detailed topology of the event in the region where excess was observed, however, was unclear since these studies measured the cross section by integrating the kinematical variables. This thesis spotted the kinematical region of the excess by observing the variables of the second jet as described above.

The kinematical region where the excess of the jet cross section is observed is the same as the region where the excess of the large transverse energy flow around the jet is observed. Either the cross section excess or the large pedestal excess is observed where both jets go in the forward direction ($1 < \eta_1, \eta_2 < 2$). Both of the excesses in this jet rapidity region become larger as the E_T of the jet becomes smaller.

One model to explain these excesses simultaneously is the multiple interaction model. In this model, the soft underlying events from the interaction between the photon and the proton remnants can occur in the hard process. This may increase the jet energy pedestal and thus the cross section becomes larger, as discussed in 4.4. In this thesis both the jet cross sections and the jet E_T pedestal are compared with the HERWIG with MI option. The prediction of the HERWIG MI model gives a qualitative agreement with the data; both the jet cross section and the jet energy flow increase over the HERWIG prediction without MI option. The amount of the increase, however, is not sufficient to explain the excess of the data. Since the prediction of the MI model strongly depends on the photon structure function, further tuning of the photon structure function in the region where no direct measurement has been performed may reproduce the excesses of the transverse energy flow and the cross section.

As for the absolute cross section, which the models predict smaller values than the observation, there are some possibilities left to improve. First, there is a possible change in the cross section in the whole x_γ region when the photon structure function is modified. The recent study in the paper by Klasen and Kramer [62] demonstrated that the change of the photon structure function may change the cross section even in $x_\gamma > 0.75$ where

the direct process is dominant, due to the change of the cross section in high-x_γ resolved process.

Second, the cross section in NLO calculation becomes larger than the LO calculation in general. For the photoproduction at HERA energy, the NLO calculation [63] has demonstrated that it exceeds the LO in the inclusive jet cross section. The NLO calculation of the inclusive dijet cross section of the direct process [35] also shows an increase. In these calculations, the increase of the cross section is uniform in any rapidity and E_T of the jet which can be measured by experiments. Therefore the overall increase of the inclusive dijet cross section in NLO can be expected.

Third, the cross section depends on the choice of the scale in hard scattering. In the PYTHIA and HERWIG model, the scale is chosen as $Q \approx p_T$. If one changes it to $p_T/2$, the cross section becomes larger. This ambiguity becomes smaller when all the scales in the photon structure function, the factorization scale and in the hard scattering for both direct and resolved process are treated simultaneously in NLO. Figure 9.1 which is taken from the paper by Bödeker et al. [64] shows the dependence of the scale for LO (upper) and NLO (lower). It is seen that the cross section is less sensitive to the change of the scales in the NLO calculation.

Considering these possibilities, the comparison of the cross section with the full NLO calculation with various photon structure functions is an interesting subject. Therefore the NLO calculation for the resolved process of the inclusive dijet cross section in addition to that of the direct process is desired for the precise evaluation of the cross section.

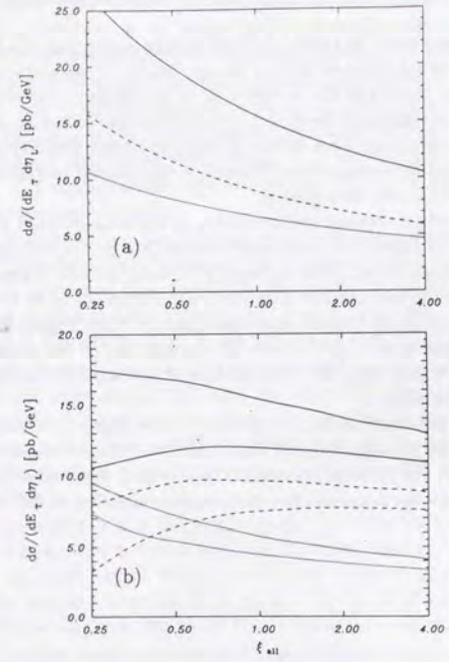

Figure 9.1: The inclusive jet cross section $d\sigma/dE_T d\eta$ at $\eta = 1.5$, in photoproduction at HERA from Böedker et al. The cross section for direct (dotted), resolved (dashed) and complete (solid lines) are plotted as the function of all three scales with $\mu = Q_p = Q_\gamma = \xi_{all} E_T$. (a) Leading order, (b) NLO with cone radius R = 0.3 and 0.7 (the cross section increases as R).

Chapter 10

Conclusion

The inclusive dijet cross section, $d\sigma/dE_T d\eta_1 d\eta_2$ and $(d\sigma/d\eta_2)|_{E_T > E_T^{min}, \eta_1}$ are measured for the first time for events in the photoproduction regime of $Q^2 < 4$ GeV and $0.2 < y < 0.85$, in positron-proton collision at HERA at $\sqrt{s} = 300$ GeV. The data of 2.62 pb^{-1} from the 1994 run was used. Events with two or more jets with $E_T > 8$ GeV and $-1 < \eta < 2$ are required by using the cone algorithm jet finder based on the calorimeter energy. The cross section is defined inclusively to see all of the possible kinematical range. In this way x_γ can be calculated experimentally for each event and the direct process is separated by a cut of $x_\gamma > 0.75$. The jet rate of the event with at least two high-p_T jets, and the energy correlation of the two high-p_T jets are investigated. The energy flow around the jet is also studied.

The cross section is compared with the prediction of PYTHIA and HERWIG that are based on the lowest order matrix element of the hard process together with the parton shower to simulate the higher order effects. The overall cross section is described well by the PYTHIA and HERWIG models up to E_T of 50 GeV, which indicates the success of the perturbative QCD in the hard process of the photon-proton collision. The ratio of two jet events to three jet events and the energy correlation of the two jets show a fair agreement with the PYTHIA MC.

After a more detailed comparison, however, the excess of the cross section is observed in the case where both jets are in the forward region ($\eta_1, \eta_2 > 1$). In this region, a large excess of the jet transverse energy pedestal is observed as well. To explain the excess on the cross section and the energy flow simultaneously, HERWIG with the multiple interaction option is compared with the data. The model improves the description of the energy flow and the cross section qualitatively, though the amount of the excess is not fully reproduced.

The absolute cross section of the models, PYTHIA and HERWIG, is smaller than the data in most of the kinematic region. Possible remedies are the change of the photon structure function, the NLO calculation and the hard scattering scale. For the unambiguous comparison with the theoretical calculation, a complete NLO calculation is desired.

Acknowledgements

First of all I would like to express my cordial thanks to Prof. S. Yamada for his guidance and advices throughout my graduate student course, and for his giving me an opportunity to participating to the ZEUS experiment.

I also give my special thanks to Dr. K.Tokushuku for giving me a chance to work on the softwares of GFLT, and for suggesting me to study the photoproduction at HERA and this theme of this thesis.

My first experience on the physics analysis at HERA was the study of the photon remnant, together with Prof. R. Nania, Dr. B. Behrens and Prof. J. Whitmore and Dr. K. Tokushuku. The experience on the cooperation and the discussion with them was essential and invaluable in my life of the study in high energy physics. I with to thank all of them. Also this thesis is due to the discussion and suggestion with C. Glasman, L. Feld, J. Butterworth, J. Terron and many members of the physics working group for hard photoproduction. I acknowledge them for their kind suggestion till the last minutes.

I would like to express my thanks to Dr. M. Kuze for his support and the discussion with him during my stay at DESY. Also my thanks is given to Dr. T. Ishii for the discussion on my study during at INS and his encouragement. The discussion and the cooperation both at INS and DESY with the Dr. T Hasegawa, Dr. M. Hazumi, Dr. T. Hazumi, Dr. M. Nakao, Dr. I. Fleck, Mr. I. Suzuki, Mr. S. Mine, Mr. K. Umemori, Mr. M. Inuzuka, Mr. K. Homma Mr. K. Yamauchi and Mr. T. Abe were invaluable in the study and highly appreciated.

The continuous encouragements from my old friends were essential during the work on this thesis. Lastly I would like to thank my parents and relatives for not only the financial and life support but also the spiritual support.

Bibliography

[1] E. D. Bloom et al., Phys. Rev. Lett. **23**(1969)930.
M. Breidenbach et al., Phys. Rev. Lett. **23**(1969)935.

[2] R. P. Feynman, Phys. Rev. Lett. **23**(1969)1415.

[3] TASSO Collaboration, R. Brandelik et al., Phys. Lett. **86B**(1979)243.
MARK J Collaboration, D. P. Barber et al., Phys. Rev. Lett. **43**(1979)830.
PLUTO Collaboration, Ch. Berger et al., Phys. Lett. **86B**(1979)418.
JADE Collaboration, W. Bartel et al., Phys. Lett. **91B**(1980)142.

[4] UA2 Collaboration, M. Banner et al., Phys. Lett. **118B**(1982)203.

[5] D. J. Fox et al., Phys. Rev. Lett. **33**(1974)1504.
Y. Watanabe et al., Phys. Rev. Lett. **35**(1975)898.
C. Chang et al., Phys. Rev. Lett. **35**(1975)901.

[6] T. Eichten et al., Phys. Lett. **B46**(1973)274.

[7] V. N. Gribov and L. N. Lipatov, Sov. Journ. Nucl. Phys. **15** (1972) 438 and 675.

[8] G. Altarelli and G. Parisi, Nucl. Phys. **126** (1977) 297.

[9] J. J. Sakurai, Phys. Rev. Lett. **22**(1969)981.

[10] TASSO Collaboration, M. Althoff et al., Z. Phys **C31** (1986) 527.
PLUTO Collaboration, C. Berger et al., Nucl. Phys **B281** (1987) 365.
TPC/2γ Collaboration, H. Aihara et al., Z. Phys **C34** (1987) 1.
OPAL Collaboration, R. Akers et al., Z. Phys **C61** (1994) 199.
TOPAZ Collaboration, K. Muramatsu et al., Phys. Lett. **B332** (1994) 477.
AMY Collaboration, S. K. Sahu et al., Phys. Lett. **B346** (1995) 208.
DELPHI Collaboration, P. Abreu et al., CERN-PPE-95-087.

[11] F. Halzen and A. D. Martin, *Quarks and Leptons: A Introductory Course in Modern Particle Physics*, John Wiley & Sons, 1984.

[12] R. G. Roberts, *The structure of the proton*, Cambridge University Press, 1990.

[13] C. G. Callan and D. J. Gross, Phys. Rev. Lett. **22**(1969)156.

[14] H. Baer, J. Ohnemus and J. F. Owens, Z. Phys **C42** (1989) 657.

[15] G. A. Schuler and T. Sjöstrand, Phys. Lett **B300** (1993) 169.

[16] P. Aurenche, J. P. Guillet and M. Fontannaz, Z. Phys. **C64**(1994)621.

[17] M. Drees and K. Grassie, Z. Phys **C28** (1985) 451.

[18] H. Abramowicz, K. Charchula and A. Levy, Phys. Lett **B269**(1991)458.

[19] M. Glück, E. Reya and A. Vogt, Z. Phys **C53**(1992)127.

[20] L. E. Gordon and J. K. Storrow, Z. Phys **C56** (1992) 307.

[21] ZEUS collaboration, M. Derrick et al., Phys. Lett. **B293**(1992)465.

[22] H1 collaboration, T. Ahmed et al., Phys. Lett. **B299**(1993)374.

[23] H1 Collaboration, T. Ahmed et al., Phys. Lett. **B297**(1992)205.

[24] ZEUS Collaboration, M. Derrick et al., Phys. Lett. **B297**(1992)404.

[25] H1 collaboration, I. Abt et al., Phys. Lett. **B314**(1993)436.

[26] ZEUS Collaboration, M. Derrick et al., Phys. Lett. **B342**(1995)417.

[27] ZEUS Collaboration, M. Derrick et al., Phys. Lett. **B322**(1994)287.

[28] ZEUS Collaboration, M. Derrick et al., Phys. Lett. **B348**(1995)665.

[29] H1 Collaboration, T. Ahmed et al, Nucl. Phys. **B445**(1995)195.

[30] J. F. Owens, Phys. Rev **D21** (1980) 54.

[31] For example, J. Chýla, Phys. Lett. **B320**(1994)186.

[32] F. Jacquet and A. Blondel, Proceedings of the study of an *ep* facility for Europe, DESY 79/48(1979)391, U. Amaldi ed.

[33] W. T. Giele, E. W. N. Glover and D. A. Kosower, Phys. Rev. Lett. **73**(1994)2019.

[34] CDF Collaboration, F. Abe et al., FERILAB-Conf-93/210-E
D0 Collaboration, S. Abachi et al., FERMILAB-Conf-95/217-E.

[35] M. Klasen and G. Kramer, DESY 95-226.

[36] The ZEUS Detector, Status Report 1993, DESY(1993).

[37] ZEUS Calorimeter group, A. Andresen et al., Nucl. Instrum. Meth. **A309**(1991)101.

[38] ZEUS Barrel Calorimeter Group, A. Bernstein et al., Nucl. Instrum. Meth. **A336**(1993)23.

[39] K. Piotrzkowski and Maciej Zachara, ZEUS-Note 95-138.

[40] M. van der Horst, Phys. Lett. **B244(1990)107.**

[41] Y. Yamazaki, *Offline Analysis of the ZEUS First Level Trigger* (in Japanese), Master thesis, Univ. of Tokyo(1993).

[42] Henk Uijterwaal, *The Global Second Level Trigger*, PhD thesis of NIKHEF, 1992.

[43] T. Sjöstrand, Computer Physics Commun. **82** (1994) 74.

[44] G. Marchesini et al., Computer Physics Commun., **67**(1992)465.

[45] J. M. Butterworth and J. R. Forshaw, RAL-94-088 (1994).

[46] T. Sjöstrand, Comput. Phys. Commun. **39**(1986)347.

[47] ZEUS Collaboration, M. Derrick et al., contributed paper to the International Europhysics Conference on High Energy Physics(EPS-HEP)EPS-0380, Brussels, July 1995.

[48] P. Bruni and G. Ingelman, *Proc. of the International Europhysics Conference*, editted by J. Carr and M. Perrotet, Marseille, France, July 1993 (Ed. Frontiers, Giu-sur-Yvette, 1994) p.595.

[49] G. Ingelmann and P. E. Schlein, Phys. Lett. **B152**(1985)256.

[50] ZEUS Collaboration, M. Derrick et al., Phys. Lett. **B315**(1993)481, **B332**(1994)228.
H1 Collaboration, T. Ahmed et al., Nucl. Phys. **B429**(1994)477.

[51] ZEUS Collaboration, M. Derrick et al., Phys. Lett. **B346**(1995)399.
H1 Collaboration, T. Ahmed et al., Nucl. Phys. **B435**(1995)3.

[52] H1 Collaboration, T. Ahmed et al., Phys. Lett. **B348**(1995)681.
ZEUS Collaboration, M. Derrick et al., DESY 95-093.

[53] W. H. Smith et al., Nucl. Instrum. Meth. **A355**(1995)278.

[54] F. Chlebana, ZEUS-Note **94-102**(1994).

[55] JADE collaboration, W. Bartel et al., Zeit. Phys. **C33**(1986)23; S. Bethke et al., Phys. Lett. **B213**(1988)235.

[56] S. Catani, Yu.L. Dokshitser, M. Olsson, G. Turnock and B.R. Webber, Phys. Lett. **B269**(1991)432.

[57] J. Huth et al., in Proceedings of the Summer Study on High Energy Physics, Snowmass, 1990.

[58] In the library for the physics analysis in ZEUS(PHANTOM).

[59] M. H. Seymour, CERN-TH/95-176.

[60] ZEUS collaboration, M. Derrick et al., Phys. Lett. **B354**(1995)163.

[61] H1 Collaboration, T. Ahmed et al, DESY 95-219.

[62] M. Klasen and G. Kramer, DESY 95-159.

[63] M. Klasen, G. Kramer and S. G. Salesh, DESY 94-232.

[64] D. Bödeker, G. Kramer and S. G. Salesch, Z. Phys **C63**(1994)471.

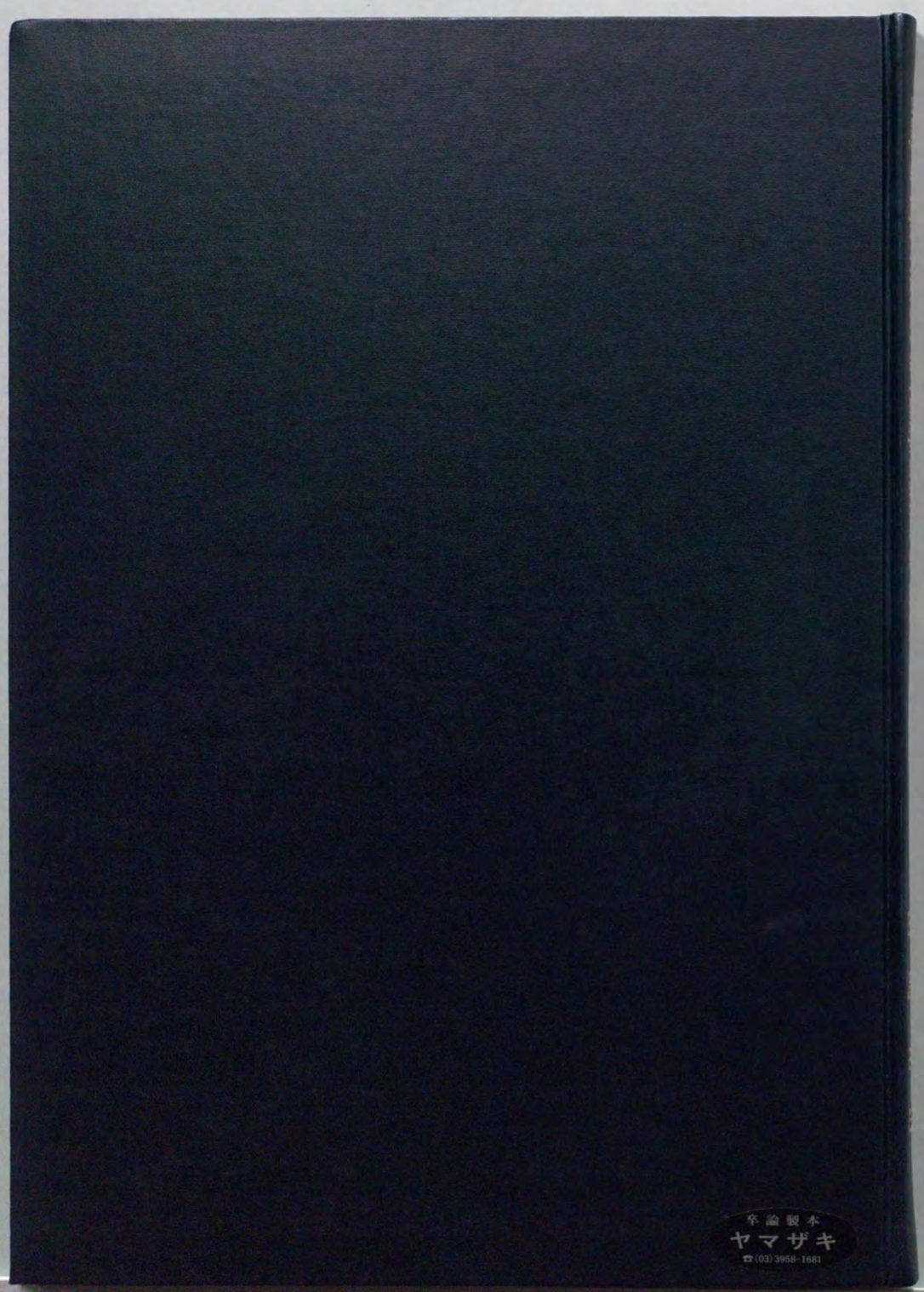
卒論製本
ヤマザキ
☎(03)3958-1681